Helsinki University of Technology Publications in Engineering Physics
Teknillisen korkeakoulun teknillisen fysiikan julkaisuja
Espoo 2007 TKK-F-A850

STUDIES ON LIMITING FACTORS OF POLYMER ELECTROLYTE MEMBRANE FUEL CELL CATHODE PERFORMANCE

Mikko Mikkola

Dissertation for the degree of Doctor of Science in Technology to be presented with due permission of the Department of Engineering Physics and Mathematics for public examination and debate in Auditorium F1 at Helsinki University of Technology (Espoo, Finland) on the 4th of May, 2007, at 12 o'clock noon.

Helsinki University of Technology
Department of Engineering Physics and Mathematics
Laboratory of Advanced Energy Systems

Distribution:
Helsinki University of Technology
Laboratory of Advanced Energy Systems
P.O. Box 4100
02015 HUT
Finland

Tel. +358-9-451 3298
Fax. +358-9-451 3195
E-mail: mikko.mikkola@tkk.fi

ISBN 978-951-22-8589-1
ISBN 978-951-22-8590-7 (PDF)

ISSN 1456-3320
ISSN 1459-7268 (PDF)

Multiprint Oy
Espoo 2007

TEKNILLINEN KORKEAKOULU
PL 1000, 02015 TKK
http://www.tkk.fi

VÄITÖSKIRJAN TIIVISTELMÄ

Tekijä Mikko Samuli Mikkola

Väitöskirjan nimi

TUTKIMUKSIA POLYMEERIPOLTTOKENNON KATODIN SUORITUSKYKYÄ RAJOITTAVISTA TEKIJÖISTÄ

Käsikirjoituksen jättämispäivämäärä 2006-10-17	Väitöstilaisuuden ajankohta 2007-05-04
☐ Monografia	☒ Yhdistelmäväitöskirja (yhteenveto + erillisartikkelit)

Osasto	Teknillinen fysiikka ja matematiikka
Laboratorio	Teknillinen fysiikka ja matematiikka - Energiatieteet
Tutkimusala	Polttokennot
Vastaväittäjä(t)	tohtori Anders Lundblad
Työn valvoja	professori Peter Lund
(Työn ohjaaja)	

Tiivistelmä

Polttokennot ovat sähkökemiallisia laitteita, jotka muuntavat polttoaineen kemiallisen energian suoraan sähköksi ja lämmöksi. Polymeeripolttokenno on polttokennotyyppi, jossa elektrolyyttinä käytetään protonijohtavaa polymeerikalvoa. Polymeeripolttokennojen odotetaan korvaavan perinteiset teholähteet monissa käyttökohteissa, mm. ajoneuvoissa, hajautetussa energiantuotannossa, varavoimanlähteissä ja kannettavissa laitteissa.

Tässä työssä tutkittiin polymeeripolttokennon katodin suorituskykyä rajoittavia tekijöitä keskittyen aineensiirtoon ja vedenhallintaan. Hapen pelkistysreaktion häviöt jätettiin tarkastelun ulkopuolelle. Pääasiallisena tutkimuskohteena oli kaasudiffuusiokerros (KDK), jonka ominaisuudet vaikuttavat reaktanttien ja reaktiotuotteiden sekä sähkö- ja lämpövirtojen kulkuun.

KDK-tutkimuksessa oli kolme pääaluetta, materiaalien karakterisointi, fysikaalisten ominaisuuksien korrelointi suorituskykyyn sekä epätasaisen puristuspainejakauman vaikutusten tarkastelu. Karakterisointia varten kehitettiin parannettu menetelmä, ja tätä käyttäen tarkasteltiin materiaalien toimivuutta eri olosuhteissa. Mittauksessa havaittiin katodipuolen tulvimisen alkavan kaasudiffuusiokerroksessa eikä itse elektrodilta. Selvää yhteyttä fysikaalisten ominaisuuksien ja polttokennon suorituskyvyn välille ei löydetty.

Epätasaisen puristuspainejakauman havaittiin aiheuttavan paikallisia eroja KDK:n aineensiirto-ominaisuuksissa, sähköisessä johtavuudessa sekä kontaktivastuksessa eri rajapinnoilla. KDK:n johtavuuden ja KDK:n ja virtauskanavalevyn välisen kontaktivastuksen määrittämiseen puristuksen funktiona kehitettiin menetelmä.

Titaanisintterin toimivuutta polymeeripolttokennon kaasudiffuusiokerroksena tutkittiin vapaasti hengittävässä polttokennossa. Titaanisintterin havaittiin olevan mekaanisilta ominaisuuksiltaan sopivaa, mutta suuren hydrofiilisuuden takia sintteri oli altis tulvimiselle ja kontaktivastus sintterin ja muiden komponenttien välillä oli suuri.

Natriumkloridin vaikutusta polymeeripolttokennon katodilla tutkittiin kokeellisesti ja sen havaittiin johtavan peruuttamattomaan suorituskyvyn laskuun. Natriumionit korvaavat protoneita elektrolyyttipolymeerissa ja laskevat johtavuutta. Kloridi-ionilla ei havaittu olevan vaikutusta suorituskykyyn.

Asiasanat polymeeripolttokenno, katodi, kaasudiffuusiokerros, vedenhallinta, virrankatkaisu, virrantiheysjakauma

ISBN (painettu) 978-951-22-8589-1	ISSN (painettu) 1456-3320
ISBN (pdf) 978-951-22-8590-7	ISSN (pdf) 1459-7268
ISBN (muut)	Sivumäärä 78 s. + liit. 1 s.

Julkaisija Teknillisen fysiikan ja matematiikan osasto, Teknillinen korkeakoulu

Painetun väitöskirjan jakelu Teknillinen fysiikka - Energiatieteet, PL 4100, 02015 TKK

☒ Luettavissa verkossa osoitteessa http://lib.tkk.fi/Diss/2007/isbn9789512285907/

HELSINKI UNIVERSITY OF TECHNOLOGY
P. O. BOX 1000, FI-02015 TKK
http://www.tkk.fi/

ABSTRACT OF DOCTORAL DISSERTATION

Author	Mikko Samuli Mikkola

Name of the dissertation

STUDIES ON LIMITING FACTORS OF POLYMER ELECTROLYTE MEMBRANE FUEL CELL CATHODE PERFORMANCE

Date of manuscript 2006-10-17	Date of the dissertation 2007-05-04
☐ Monograph	☒ Article dissertation (summary + original articles)

Department	Engineering Physics and Mathematics
Laboratory	Advanced Energy Systems
Field of research	Fuel cells
Opponent(s)	PhD Anders Lundblad
Supervisor	professor Peter Lund
(Instructor)	

Abstract

Fuel cells are electrochemical devices that convert the chemical energy of fuel into electricity and heat. Polymer electrolyte membrane fuel cells (PEMFCs) are a type of fuel cells which use a proton conducting polymer membrane as the electrolyte. PEMFCs are envisioned to replace conventional power sources in many applications, including transportation, stationary distributed and backup power generation, and portable devices. This work concentrated on the limiting factors of the PEMFC cathode performance, focusing on mass transport and water management. Overpotential of oxygen reduction reaction was outside the scope of this thesis. The main study subject was the porous transport layer (PTL). Physical properties of the PTL have a significant effect on reactant and reaction product transport, as well as electrical and thermal fluxes.

PTL research concentrated on three main areas, characterization of PTL media, correlation of PTL physical properties to fuel cell performance, and the effects of inhomogeneous compression distribution. An improved method for PTL characterization was developed and used to investigate the performance of PTL materials under different operating conditions. It was observed that the flooding on the cathode side begins in the PTL, not the electrode itself. A clear relation between PTL properties and fuel cell performance could not be established.

Inhomogeneous compression of PTLs was found to cause local variations in the mass transport properties, electrical conductivity and contact resistance at various interfaces. A method for determining the bulk conductivity of the PTL and the contact resistance at the PTL-flow field plate interface as a function of compression was developed.

The applicability of titanium sinters as porous transport layers for free-breathing PEMFC was investigated. The mechanical properties of titanium sinters were found acceptable, but due to high hydrophilicity, the sinter was prone to flooding. Furthermore, contact resistance between the sinter and other components was high.

The effect of sodium chloride on PEMFC performance was investigated experimentally and found to cause an irreversible performance loss. Sodium ions were found to replace protons in the electrolyte membrane and thus increase resistance. Chloride ions were not observed to interfere with fuel cell operation under the conditions used in the experiments.

Keywords PEMFC, cathode, porous transport layer, gas diffusion layer, water management, impurities

ISBN (printed)	978-951-22-8589-1	ISSN (printed)	1456-3320
ISBN (pdf)	978-951-22-8590-7	ISSN (pdf)	1459-7268
ISBN (others)		Number of pages	78 p. + app. 1 p.

Publisher Department of Engineering Physics and Mathematics, Helsinki University of Technology

Print distribution Laboratory of Advanced Energy Systems, P.O. Box 4100, 02015 TKK, Finland

☒ The dissertation can be read at http://lib.tkk.fi/Diss/2007/isbn9789512285907/

Table of Contents

Preface

The work presented here was carried out between 2002 and 2006 in the laboratory of Advanced Energy Systems at Helsinki University of Technology, under the supervision of Professor Peter Lund. The laboratory provided a pleasant, inspiring, creative and sometimes surreal environment to work in. Present and former colleagues in the fuel cell group, D.Sc. Tuomas Mennola, D.Sc. Matti Noponen, D.Sc. Tero Hottinen, Mr. Olli Himanen, Ms. Suvi Karvonen, Mr. Iwao Nitta and others deserve my gratitude. This thesis, and every day at work in general would not have been this good without your ideas, suggestions, relentless criticism and our countless discussions, on and off topic. Outside our own group, working with PhD Jari Ihonen at KTH, Sweden proved to be both fruitful and pleasant.

Furthermore, I thank PhD Francisco Uribe, PhD Wayne Smith, Mrs. Judith Valerio, Mr. Tommy Rockward, Mrs. Marilyn Ellis, PhD Bryan Pivovar, PhD Richard Silver, all the Johns and everyone else at the Los Alamos National Laboratory MST-11 for their kindness and help during my visit there Aug 2003 - Jul 2004.

Olli, Tuomas K. and Ville - thank you for taking me out of the lab and to the crags or indoor wall even when I really didn't feel like it. Straining the mind is easier if you strain *flexor digitori* and the rest of the body every now and then.

I want to express my gratitude to my lovely wife Tiina, for understanding and enduring my long hours at the lab and lost in homework.

Lopuksi kiitos vanhemmilleni, Maijalle ja Pekalle. Koulun penkillä ei koskaan tuntunut siltä, että olisitte painostaneet valitsemaan jonkin tietyn uran. Tässä on siitä tulos, ja tämä väitöskirja on omistettu teille.

Results? Why, man, I have gotten lots of results! If I find 10,000 ways something won't work, I haven't failed. I am not discouraged, because every wrong attempt discarded is often a step forward. – Thomas A. Edison

List of publications

This thesis is an introduction to the following publications:

- **I** Tuomas Mennola, Mikko Mikkola, Matti Noponen, Tero Hottinen and Peter Lund, "**Measurement of ohmic voltage losses in individual cells of a PEMFC stack**", *J. Power Sources* 112(1) 2002, pp. 261-272
- **II** Matti Noponen, Tuomas Mennola, Mikko Mikkola, Tero Hottinen and Peter Lund, "**Measurement of current distribution in a free-breathing PEMFC**", *J. Power Sources* 106(1-2) 2002, pp. 304-312
- **III** T. Hottinen, M. Mikkola, T. Mennola and P. Lund, "**Titanium sinter as gas diffusion backing in PEMFC**". *J. Power Sources* 118(1-2) 2003, pp. 183-188
- **IV** J. Ihonen, M. Mikkola and G. Lindbergh, "**Flooding of Gas Diffusion Backing in PEFCs: Physical and Electrochemical Characterization**", *J. Electrochem. Soc.* 151(8) 2004, pp. A1152–A1161
- **V** Iwao Nitta, Tero Hottinen, Olli Himanen and Mikko Mikkola, “**Inhomogeneous Compression of PEMFC Gas Diffusion Layer – Part I: Experimental”**, accepted for publication in *J. Power Sources* Dec 2006
- **VI** Mikko S. Mikkola, Tommy Rockward, Bryan S. Pivovar and Francisco A. Uribe, ”**The Effect of NaCl in Cathode Air Stream on PEMFC Performance**”, accepted for publication in *Fuel Cells* May 2006

For publication I, the author developed the methodology used for resistance measurement of individual cells in a fuel cell and contributed to data analysis and writing process.

For publication II, the author participated in the development of segmented current collector cell, especially testing development versions, measurement planning, data analysis, and writing process.

In publication III, the author contributed to design of experiments and characterization of titanium sinters, data analysis and article writing.

For publication IV, the author had principal responsibility for subchapters about pore size distribution and contact angle measurements, including experimental design, measurements, data analysis and writing. Furthermore, the author contributed to design and construction of experimental equipment, conducting measurements, and participated in data analysis and writing process.

For publication V, the author contributed to design of the experimental equipment and measurements and participated in the writing process.

For publication VI, the author had principal responsibility for design, experiments, data analysis and writing.

Publications with contribution by the author but not included in this thesis are listed in Appendix A.

1. Introduction

1.1. Background

World primary energy demand was 10.7 Gtoe[a] in 2003 [1], up 94 % from 5.5 Gtoe in 1971 [2] and expected to rise by 58% to 16.3 Gtoe by 2030 [3]. At the same time, fossil fuel resources, especially oil, are limited and geographically unevenly distributed, and there is pressure to combat anthropogenic climate change by reducing greenhouse gas emissions. This creates a need to increase the share of renewable energy sources (hydro, wave, tidal, geothermal, solar and wind power, and biomass) and improve the efficiency of end use technologies. Fuel cells are an energy conversion technology well suited for the future, since they have high efficiency, low emissions and can use fuels from renewable sources.

Fuel cells are electrochemical devices that transform the chemical energy of the fuel directly into electricity and heat. The operating principle of fuel cells is similar to primary batteries, except that in fuel cells reactants are stored externally.

The main benefit of fuel cells is high efficiency. Fuel cells are not heat engines, but the energy conversion process is fundamentally different, and thus Carnot's efficiency limitation does not apply. Furthermore, fuel cell efficiency is not strongly dependent on the device size and contrary to heat engines, does not suffer from operating on partial load but actually improves. High efficiency even on partial load and separation of conversion and storage functions make fuel cells an attractive power source for numerous applications.

Other often quoted benefits of fuel cells are fuel flexibility, low emissions, low noise and footprint, and scalability. However, fuel flexibility and scalability on the extremes depend to some degree on the fuel cell type, and emissions on the fuel. The optimal fuel for fuel cells is hydrogen, which produces only water as exhaust and can be derived from fossil or renewable sources or produced via electrolysis, but also many others, both from fossil and biological sources can be used.

The strongest advocate of the introduction of fuel cells is the automotive industry seeking to replace internal combustion engines as vehicle power sources with a more efficient and environmentally friendly option. Other viable application areas are mobile electronics, backup power systems, distributed energy generation, combined heat and power production, power systems for remote locations, and military and space applications.

From technology perspective fuel cells are ready for market introduction. However, fuel cell applications will compete with batteries, internal combustion engines and other established power sources in a saturated market, where successful market penetration requires economical viability. Currently, the price of fuel cells is not yet competitive in most applications.

---

[a] toe = ton of oil equivalent, 1 toe ≈ 41.8 GJ = 11.6 MWh

1.2. Motivation and objectives

The main outstanding issues with fuel cell technology that impede widespread market penetration are the high cost compared to conventional technologies and establishing long term durability and reliability. Currently, vehicle power trains based on internal combustion engines cost \$25-\$35/kW, whereas current price of fuel cells is close to \$1000/kW and high volume cost estimate with 2004 technology was \$110/kW [4]. Fuel cell power trains need to cost less than \$50/kW to be competitive against internal combustion engines in vehicle applications [5]. U.S. DOE target cost for vehicle fuel cells is \$45/kW by 2010, with a power train life span of 5000 hours [4]. For stationary applications, competitive price lies in the range of \$400-\$750/kW with \$1000/kW acceptable for initial applications [6]. However, required system life time is over 40 000 hours, which has not yet been demonstrated [5].

Lowering price per watt can be done either by improving performance using current materials or developing cheaper materials and components, or both. In this thesis, the emphasis is on improving performance, and thus material development will not be discussed further than mentioning that cheaper ion conductors, catalysts and manufacturing methods are needed.

In many cases, improving fuel cell performance is a process of trial and error. Some areas of fuel cell systems are very complex and theoretical understanding is not complete. Investigating these areas may yield knowledge that enables development of more efficient, stable and durable fuel cell devices.

This thesis is concentrated on one of the less studied but crucial components of polymer electrolyte membrane fuel cells, the porous transport layer. The goal of the studies summarized here was to increase knowledge on the operation of porous transport layers and their performance determining properties.

1.3. Outline of this thesis

This thesis begins with an introduction to fuel cells in chapter 2. The history of fuel cells and a brief overview of different fuel cell types are given. The fuel cell type relevant for this thesis, polymer electrolyte membrane fuel cell is presented in detail in chapter 3, covering main functional components, theory of operation, cell performance, loss mechanisms and efficiency. The role of water and heat management and mass transport in cell performance is emphasized.

Chapters 5 to 10 summarize and review the publications listed above. Each chapter provides an introduction into the topic and an overview of methods and experimental setup. The most important results are reviewed and discussed. To support chapters 5 to 10, the fuel cell test station used for most of the experimental work described in the publications is described in chapter 4. Conclusions on the results presented in previous chapters are presented in chapter 11, in which the significance of the results is discussed in a broader perspective and some suggestions for further studies are given.

2. Fuel cells

2.1. Description in a nutshell

In the simplest form, a fuel cell consists of two electrodes separated by an electrolyte, which prevents reactants from directly mixing. The fuel is oxidized on the anode while oxidant species are reduced on the cathode. An ion, product of either anode or cathode reaction depending on the fuel cell type, passes through the electrolyte to the other side of the cell, while electrons travel through the external circuit, producing electric current. Transported ions and electrons react with the other reactant species, forming reaction product and heat.

2.2. History of fuel cells and current trends

The journey of the fuel cell from the discovery of the theoretical basics to the threshold of commercialization has been a long one. A Swiss chemist Christian Friedrich Schönbein (1799-1868) described the operational principle of fuel cells in the *Philosophical Magazine* in January 1839 [7], and a Welsh lawyer and scientist Sir William R. Grove fabricated the first prototype cells, or gas batteries, as he referred to them. Grove's papers on the subject appeared in the *Philosophical Magazine* in February 1839 and December 1842 and in the *Philosophical Transactions* in 1843.

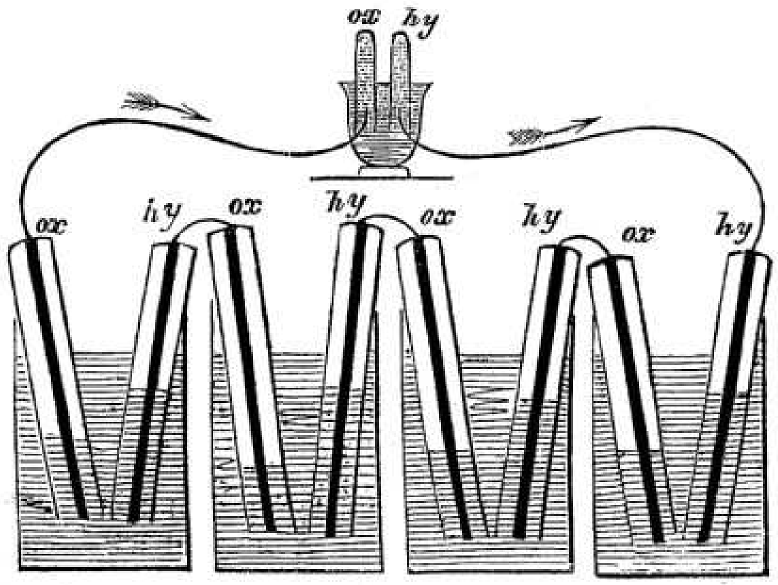

Figure 1: William Grove's prototype fuel cell

Grove's gas battery consisted of platinum strip electrodes surrounded by tubes containing hydrogen and oxygen in a dilute solution of sulfuric acid and water. This design, illustrated in Figure 1, was published in the *Philosophical Magazine* in January 1839 [7]. He experimented also with other electrolytes, but was plagued by inconsistent cell performance. Grove also experimented with other fuels, e.g. camphor, essential oils, ether and alcohol [8].

The first major breakthrough in fuel cell[b] technology was achieved in the 1890s by a German-born British scientist Ludwig Mond and his assistant Charles Langer, who introduced improved porous electrodes [9]. Porous electrodes were already patented by M. Vergnes [10], but they suffered a performance loss when the platinum catalyst became wet.

Mond and Langer attempted to build the first practical fuel cell device, which would operate on air and industrial coal gas. Their cell operated at 2.8-3.5 mA cm^{-2} at 0.73 V with cells of 700 cm^2, covered with 0.35 g of platinum foil and 1 g of platinum black[c]. Furthermore, they recognized the large losses at the oxygen electrode, and the roles of internal resistance and concentration polarization as loss mechanisms [11].

Sulfuric acid was the dominant electrolyte in the 19th century. In the latter half of the century, much attention was given to direct coal fuel cells which worked at higher temperatures with molten salts, such as sodium nitrate and potassium and sodium hydroxide, as electrolyte [11]. In the 1890s, William White Jacques used phosphoric acid as the electrolyte for the first time.

Although fuel cell research in Germany during the 1920s laid foundations for carbonate cycle and solid oxide fuel cells, the next significant contribution to fuel cell technology was made by a British engineer, Dr. Francis T. Bacon. He began experimenting with alkali electrolytes and cheap porous nickel electrodes in the early 1930s. Potassium hydroxide performed as well as acid electrolytes and was less corrosive to the electrodes. Over the next twenty years, Bacon made sufficient progress to demonstrate a practical 5 kW hydrogen-oxygen fuel cell stack in August 1959 [12]. The system provided 700 mA cm^{-2} at 38 bar pressure and temperature of 200 °C and could be used to power a forklift or a welding machine. Later that same year, Allis-Chalmers Manufacturing Co. demonstrated a tractor powered by a 15 kW fuel cell stack. The design was based on Bacon's patents, which had been obtained by Pratt & Whitney Aircraft[d], but operated at lower temperature and pressure.

The space race in the 1950s and 1960s promoted the development of fuel cells. In search of an improved energy source for on-board electricity, NASA chose fuel cells to power space missions and funded over 200 research projects awarded to industry and universities [13]. General Electric developed the first polymer electrolyte membrane fuel cells (PEMFCs[e]) for Gemini space missions. The first mission utilizing fuel cells was Gemini V in 1965 [14]. Gemini V doubled the space flight record of Gemini IV mission, thanks to the fuel cell system, which outperformed the battery systems used on previous missions.

Initially, sulfonated polystyrene membranes were used for electrolytes, but they were replaced in 1966 by Nafion® ionomer[f], which proved to be superior in performance and durability to sulfonated polystyrene. However, the Apollo space missions and subsequent Apollo-Soyuz, Skylab and Space Shuttle missions utilized fuel cells based on Bacon's design and alkaline potassium hydroxide electrolyte, developed by Pratt & Whitney Aircraft.

---

[b] Depending on the source, the term 'fuel cell' is attributed both to Mond and Langer (1899), and Jacques.

[c] A fine black powder of platinum; used as a catalyst in chemical reactions

[d] Later UTC Fuel Cells, a part of United Technologies Corporation.

[e] PEMFC is also known as proton exchange membrane fuel cell, polymer electrolyte fuel cell (PEFC), and solid polymer fuel cell (SPFC).

[f] Nafion® was developed for the chlor-alkali industry in 1962 by Walter Grot of E.I. du Pont de Nemours and Company. Source: http://en.wikipedia.org/wiki/Nafion, quoted 2006-08-02

Despite their success in space programs, fuel cell systems were limited to space missions and other special applications, where high cost could be tolerated. It was not until the late 1980s and early 1990s when fuel cells became a realistic option for wider application base. Several pivotal innovations drove the cost of fuel cells down, making development of PEM fuel cell systems viable. The most notable improvement was the invention of thin-film electrodes, which lead to reduction of platinum loading.

In the last two decades, driving forces for fuel cell research and development have been the automotive industry and distributed energy generation sector, and more recently portable electronics manufacturers. Due to limited reserves of fossil fuels, environmental concerns and imposed limitations on pollutant and greenhouse gas emissions, vehicle manufacturers are looking for a clean and efficient replacement for the internal combustion engine. The interest in using fuel cells to power portable electronics, e.g. laptop computers, has increased with the increasing requirements for higher energy density, specific energy and longer operational time.

In most applications, fuel cells are entering a saturated market and thus need to outperform the competition. Although the technology is mature enough for commercial introduction, the price is still too high for market penetration. Therefore, current research aims at lowering the cost to competitive level by replacing expensive materials and improving performance.

2.3. Fuel cells types

Fuel cells are a family of technologies that share the principle of electrochemical oxidation of the fuel and spatial separation of oxidation of fuel and reduction of oxidant. Fuel cell types are usually characterized by their electrolyte, temperature of operation, transported ion and fuel. A summary of fuel cell types with respective electrolyte materials, transported ions and operating temperatures are presented in Table 1. Characteristic features of different fuel cell types are discussed below, with the exception of polymer electrolyte membrane fuel cell, which is discussed in detail in chapter 3.

From the fuel cell types listen in Table 1, molten carbonate fuel cells and solid oxide fuel cells are classified as high temperature fuel cells, the rest are low temperature fuel cells, even if the operating temperature of phosphoric acid and alkaline fuel cells exceeds 200 °C.

Alkaline fuel cells are very efficient and cheapest to manufacture, but the electrolyte is sensitive to carbon dioxide and therefore oxidant air has to be scrubbed before use, or pure oxygen used, which makes operating AFCs expensive. The primary fuel is hydrogen, but also the use of low alcohols and sodium borohydride has been studied [e.g. 15 16]. AFCs are used in applications that require high performance regardless of price, e.g. space and military applications.

Phosphoric acid fuel cell was the first commercial fuel cell type. Owing to operating temperature closer to 200 °C, in PAFCs platinum catalyst is less sensitive to carbon monoxide in the fuel, but still requires noble metal catalysts to enhance oxygen reduction reaction on the cathode, and corrosion tolerant materials because of highly corrosive electrolyte. PAFCs have been used mostly for stationary electricity and heat production, but the interest has waned, since the potential for cost reduction is considered low.

Table 1: Summary of electrolyte materials, transported ions and operating temperatures of common fuel cell types.

Fuel cell type	Electrolyte material	Transported ion	Operating temperature
Polymer electrolyte membrane fuel cell (PEMFC)	Cation conducting polymer membrane	H^+	20-80 °C
Direct methanol/ethanol fuel cell (DMFC/DEFC)	Cation conducting polymer membrane	H^+	20-80 °C
Direct formic acid fuel cell (DFACF)	Cation conducting polymer membrane	H^+	20-80 °C
Direct borohydride fuel cell (DBFC)	Aqueous alkaline solution (e.g. KOH), Anion or cation conducting polymer membrane	OH^- or Na^+	20-80 °C
Phosphoric acid fuel cell (PAFC)	Molten phosphoric acid (H_3PO_4)	H^+	150-200 °C
Alkaline fuel cell (AFC)	Aqueous alkaline solution (e.g. KOH)	OH^-	<250 °C
Molten carbonate fuel cell (MCFC)	Molten alkaline carbonate (e.g. $NaHCO_3$)	CO_3^{2-}	600-700 °C
Solid oxide fuel cell (SOFC)	O^{2-} conducting ceramic oxide (e.g. Y_2O_3-stabilized ZrO_2)	O^{2-}	600-1000 °C

Direct methanol, ethanol and formic acid fuel cells are closely related to polymer electrolyte membrane fuel cells. The main difference is the fuel which these cell types utilize instead of neat hydrogen or hydrogen rich gas. The cathode side is often identical to that in PEMFCs, but the anode is modified to accept liquid fuels and tolerate more carbon monoxide, which is sometimes created as a byproduct in fuel oxidation. The prime attraction of these fuel cell types is the high energy density and easy handling of the fuel compared to hydrogen. These cell types are still in development phase, often afflicted by fuel permeation to the cathode side, although there are some DMFC applications already available on the market.

There are three variants of the direct borohydride fuel cell, which employ different electrolytes. The PEMFC subtype uses a cation conducting polymer membrane, and the mobile ion is Na^+, whereas AFC subtypes utilize either anion conductive polymer membranes or immobilized KOH and the charge carrier in the electrolyte is OH^-. DBFCs with KOH electrolyte have an advantage over ordinary AFCs, since the waste product, $NaBO_2$, prevents the CO_2 poisoning of the electrolyte, and thus removing the need for CO_2 scrubbing. Like direct ethanol and formic acid fuel cells, direct borohydride fuel cells are still in the development phase.

The focus of molten carbonate fuel cell development has been on larger stationary or marine power plants, where slow start-up time and large footprint are not an issue. Thanks to relatively high operating temperature, electrode reactions do not require noble metal catalysts. In addition to many common fossil and renewable fuels that can be reformed internally, MCFCs can use also carbon monoxide as a fuel. However, high operating temperature and corrosive electrolyte require expensive materials for cell components for mechanical stability and sufficient life time. Furthermore, carbonate forming reaction at the cathode needs a source of carbon dioxide, which is usually provided by recycling from anode exhaust gas.

Solid oxide fuel cells utilize a ceramic oxygen ion conductive electrolyte and operate at high temperature. Therefore, there is no need for noble metal catalysts and carbon monoxide can be used as a fuel. High operating temperature also allows using various hydrocarbons as fuels and using waste heat for cogeneration or in steam turbines. High operating temperature also has drawbacks. Thermal expansion has to be controlled carefully and corrosion of metal components is a challenge. SOFCs are best suited for stationary and distributed power generation, either in heat and power cogeneration or hybrid systems with gas turbines.

The field of fuel cells is very active and it is difficult to provide a comprehensive list of cell types and possible fuels that are under development. Many fuel cell types, e.g. biological fuel cells and zinc-air fuel cells were omitted, and many potential fuels, for example dimethyl ether, acetaldehyde and 2-propanol were left unmentioned.

2.4. Theory of operation

2.4.1. Theoretical cell voltage

In a hydrogen-oxygen fuel cell, PEMFC for example, hydrogen is oxidized at the anode and oxygen reduced at the cathode. Anode, cathode and total cell reactions are presented in equations 1, 2 and 3, respectively.

$$H_2 \rightarrow 2H^+ + 2e^- \tag{1}$$

$$2H^+ + 2e^- + ½O_2 \rightarrow H_2O \tag{2}$$

$$H_2 + ½O_2 \rightarrow H_2O \tag{3}$$

The phase of water produced in the cell reaction depends on the conditions under which the reaction occurs.

Standard potential E^0 for the cell reaction, i.e. the potential at standard temperature and pressure (STP) when no current is drawn, is obtained by dividing the Gibbs' energy change of the reaction at STP, ΔG^0 by the Faraday constant F (96 485.3 C mol^{-1}) and the number of electrons transferred in one reaction z,

$$E^0 = -\frac{\Delta G^0}{zF} \tag{4}$$

Assuming that water is produced as liquid in equation 3, ΔG^0 equals -237.1 kJ mol^{-1} and z equals 2, and thus the standard potential is 1.229 V. If product water is in gaseous form, the corresponding potential is 1.18 V.

For a reaction outside STP conditions, the potential is given by the Nernst equation

$$E = E^0 - \frac{RT}{zF}\ln\left[\prod_{\mathrm{i}} a_{\mathrm{i}}^{\nu_{\mathrm{i}}}\right] \tag{5}$$

Where R is the universal gas constant, T is the temperature, a_{i} and ν_{i} are the activity and stoichiometric coefficient of species i respectively. For dry air (21% oxygen, 79% inert gases) on the cathode instead of neat oxygen at a temperature of 298.15 K, equation 5 yields for liquid product

$$E = E^0 - \frac{RT}{zF}\ln\left[\frac{a_{H2O}}{a_{H2}a_{O2}^{0.5}}\right] = E^0 - \frac{RT}{zF}\ln\left[\frac{1}{0.21^{0.5}}\right] = 1.219\text{V}$$

Real PEM fuel cells do not achieve the theoretical open circuit potential given by equation (5) due to mixed potentials caused by hydrogen diffusion through the membrane and platinum oxidation on the cathode.

2.4.2. Polarization behavior

Polarization of a fuel cell is defined as the drop from open circuit voltage as a result of drawing electric current. Voltage drop is caused by various current and mass transport-induced losses, often called overpotentials. The total sum of overpotentials[g], η, is defined as the difference of the real voltage E and the theoretical one, E_t.

$$\eta = E - E_t \qquad (6)$$

Typical fuel cell polarization curve, voltage as a function of current density, is outlined in Figure 2. Additionally, the figure includes also a power density curve.

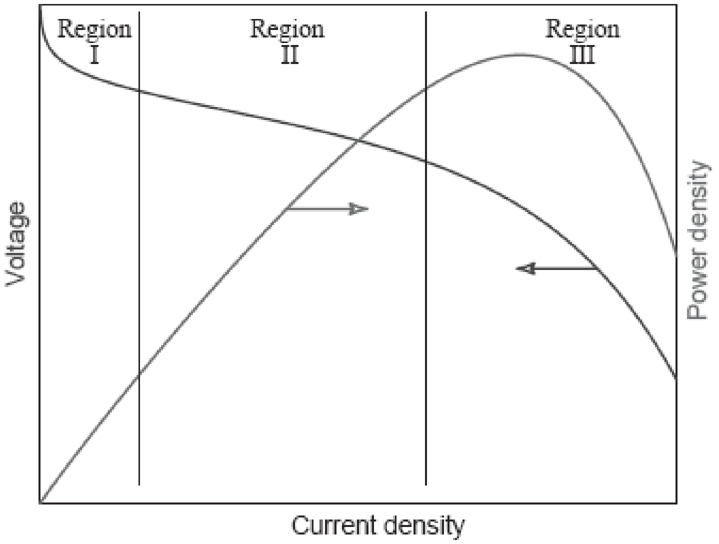

Figure 2: Characteristic polarization and power density curves of a fuel cell. (Picture: Matti Noponen)

At low current density, region I in Figure 2, the shape of the polarization curve is governed by the activation overpotential, which arises from the kinetics of charge transfer reactions across interfaces and represents the magnitude of activation energies when reactions propagate at the rate required by the current. It depends on the type of reactions and catalyst materials, electrode microstructure, reactant activities, electrolyte material (acidic/alkaline), temperature and current density.

Activation overpotential of hydrogen oxidation is negligible compared to the overpotential associated with ORR at the cathode, which is larger by several orders of magnitude [17]. Thus, anode activation overpotential is often neglected in calculations.

---

[g] To be more exact, the total sum of overpotentials averaged over the electrode area, since overpotentials may vary over the electrode area.

After the rapid drop due to activation overpotential, see region II in Figure 2, fuel cell polarization exhibits pseudolinear behavior as the current density increases. In this region, the shape of the curve is governed by the ohmic overpotential or *IR*-loss, which arises from the resistance of fuel cell components. Bulk materials and interfaces between components display an intrinsic resistance to electron flow, and electrolyte materials offer resistance to transport of ions, which carry the current in the electrolyte phase.

The magnitude of ohmic overpotential, η_{IR}, is proportional to current and cell resistance, and can be expressed as

$$\eta_{IR} = IR = jr \tag{7}$$

where I and R are the total current and cell resistance, respectively. Alternatively, ohmic loss can be expressed in terms of area or volume specific current density and resistance, j and r, respectively. This approach is useful when calculating contributions to *IR*-loss from individual components.

Resistance of rigid bulk material depends mainly on material properties, but bulk conductivity of pliable materials and contact resistance are also affected by surface properties and contact pressure between the components. Electrolyte conductivity depends primarily on temperature and for some electrolyte types, water content. The largest single contributor to cell resistance is usually the electrolyte resistance to ionic current.

Measuring fuel cell resistance is not entirely straightforward, since ohmic loss has to be separated from other overpotentials. Furthermore, electrical current is carried by ions in the electrolyte, and therefore ordinary resistance measurement methods which rely on imposing a potential difference over a sample and observing electronic current are not usable. However, there are methods to measure fuel cell resistance, which are discussed further in chapter 5.

At large current density, region III in Figure 2, the shape of the curve is determined by the mass transfer overpotential. When current density reaches a certain level, sluggishness of mass transfer processes starts to limit the supply of reactants to the electrodes, and cell voltage begins to decrease rapidly with increasing current demand. Mass transfer overpotential can be viewed as an activation energy required to drive mass transfer at the rate needed to support the current.

Polarization behavior of electrochemical RedOx systems due to activation and mass transfer overpotentials can be represented by the current-overpotential equation[h], in which current density j is expressed as a function of overpotential η.

$$j = j_0 \left\{ \frac{c_{red}}{c_{red}^b} \exp\left[\frac{(1-\alpha)zF}{RT}\eta \right] - \frac{c_{ox}}{c_{ox}^b} \exp\left[-\frac{\alpha zF}{RT}\eta \right] \right\} \tag{8}$$

j_0 is the exchange current density[i], α the charge transfer coefficient for the cathode reaction, and c_{red} and c_{ox}, and c_{red}^b and c_{ox}^b represent the electrode concentrations of

---

[h] This equation is often, and misleadingly, called the Butler-Volmer equation. The historical Butler-Volmer equation ignores mass transport, i.e. electrode and bulk concentrations are assumed equal, and thus describe polarization behavior only due to activation overpotential. This is a good approximation when current is less than 10% of the maximum current set by mass transport limitations.

[i] For a RedOx system, j_0 is the absolute value of anodic and cathodic currents in equilibrium, when total current is zero, $j = j_a + j_c = 0 \leftrightarrow |j_a| = |j_c| = j_0$.

the RedOx pair species on the electrode surface and in the bulk, respectively. The first term in equation 8 is the anodic and the latter cathodic current density. In a case where the overpotential is large, $|\eta| >> RT/zF$, one of the terms becomes insignificant, depending on the sign of the overpotential.

$$j = j_0 \frac{c_{red}}{c_{red}^b} \exp\left[\frac{(1-\alpha)zF}{RT}\eta\right] \quad , \eta > 0 \tag{9a}$$

$$j = -j_0 \frac{c_{ox}}{c_{ox}^b} \exp\left[-\frac{\alpha zF}{RT}\eta\right] \quad , \eta < 0 \tag{9b}$$

Although equation 8 appears relatively simple, situation is complicated by the fact that both concentrations and different overpotentials are not constant everywhere on the electrode surface. Local variations in temperature, reactant flow velocity and concentration in the flow channel, transport layer properties (material porosity, pore size distribution, permeability, thickness, presence of inert species etc.), humidity conditions, and so on have an effect on reactant concentration on the electrode surface and magnitude of overpotentials. Therefore, an accurate description of fuel cell polarization using equation 8 must take into account both local variations in operating conditions and species transport by convection and multicomponent diffusion. If liquid water is present, mass transport in both phases should be considered. Causes and effects of local variations in operating conditions are discussed further in chapter 3.4.

In addition to overpotential listed above, actual fuel cell voltage is often decreased by reactant diffusion through the electrolyte and presence of impurities. These react on the electrodes, creating so called mixed potentials and decreasing cell performance.

2.5. Fuel cell efficiency

High electrical efficiency is one of the attractive properties of fuel cells. Since the energy conversion process is electrochemical in nature, fuel cells are not bound by the Carnot law of efficiency heat engines are subject to. Therefore, the same equation for efficiency cannot be used, but there are several defined efficiencies for fuel cells that make up the total efficiency.

The reversible efficiency, η_{rev}, is defined as the ratio of the maximum electrical energy from the cell reaction to the reaction enthalpy. This represents the theoretical upper limit for electrical fuel cell efficiency.

$$\eta_{rev} = \frac{-\Delta G}{-\Delta H} \tag{10}$$

PEMFC reaction with liquid product has a reversible efficiency of 83% and 95% with gaseous product. There are also reactions with reversible efficiency over 100%. For example, for the formation of carbon monoxide from carbon and oxygen η_{rev} is 123%. These reactions convert the thermal energy taken from the surroundings into electrical energy. However, technical difficulties prevent the use of many theoretically promising fuel-oxidant pairs.

When electrical energy is drawn from a fuel cell, cell voltage drops due to various losses. Voltage efficiency η_{V} takes into account these losses and is defined as ratio of the actual cell voltage to the theoretical voltage.

$$\eta_V = \frac{E}{E_{rev}} = \frac{zFE}{-\Delta G} \tag{11}$$

Often, mass transport problems force to supply fuel cells with more fuel than consumed in the cell reaction. Fuel or current efficiency η_I is defined as the ratio of actual current to theoretical current, which can be calculated from Faraday's equation using the actual molar flow of fuel.

$$\eta_I = \frac{I}{I_{theor}} = \frac{I}{zF\dot{n}_{H2}} \tag{12}$$

where I is the current drawn from the cell and $\dot{n}_{H2}$ the molar flow rate of hydrogen. Furthermore, a small fraction of the fuel diffuses through the electrolyte, further decreasing fuel efficiency and generating mixed potentials, which decrease cell voltage. Fuel efficiency is closely related to the stoichiometric factor λ, which is used to describe the amount of excess fuel fed into the cell. Stoichiometric factor is defined as

$$\lambda = \frac{zF\dot{n}_{H2}}{I} \tag{13}$$

Total efficiency of a fuel cell, η_{total}, is calculated as the product of reversible, voltage and current efficiencies, equations 10 to 12.

$$\eta_{total} = \eta_{rev}\eta_V\eta_I = \frac{EI}{-\Delta H\dot{n}_{H2}} \tag{14}$$

In the nominator of equation 14 is the electrical power of the fuel cell and in the denominator the rate at which chemical energy is fed into the cell.

For complete fuel cell systems, also the power consumed by auxiliary devices must be taken into account. System efficiency η_{system} takes into account the parasitic losses by auxiliary devices, P_{aux}, which decrease efficiency.

$$\eta_{system} = \frac{EI - P_{aux}}{-\Delta H\dot{n}_{H2}} \tag{15}$$

Efficiency of fuel cell systems can be increased by combining them with gas turbines. Estimated electrical efficiencies of such fuel cell power plants can reach up to ca. 70% and total efficiency even higher if waste heat is used for e.g. space or service water heating.

3. Polymer electrolyte membrane fuel cells

3.1. Overview

Polymer electrolyte membrane fuel cells utilize a proton conducting polymer (ionomer) membrane as the electrolyte, and hydrogen and oxygen as fuel and oxidant, respectively. Hydrogen molecules are oxidized on the anode and protons are carried through the electrolyte membrane to the cathode. Electrons stripped from hydrogen molecules travel to the cathode via the external circuit creating electrical current. On the cathode, oxygen, protons and electrons react forming water and heat. The operating principle is illustrated in Figure 3.

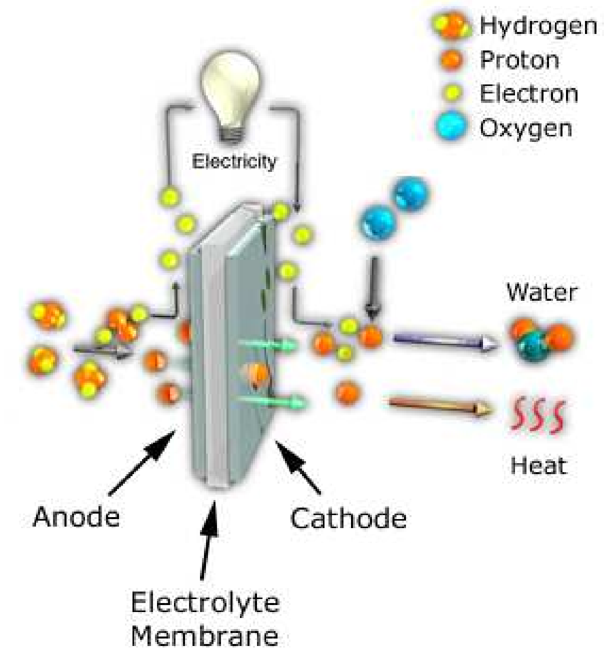

Figure 3: The operating principle of the polymer electrolyte membrane fuel cell. (Picture: XCellsis)

The schematic structure of a PEM fuel cell is presented in Figure 4. The main functional component, the membrane electrode assembly (MEA), with porous transport layers[j] (PTLs) on each side, is sandwiched between bipolar plates[k]. Bipolar plates feature flow channels for reactant delivery and PTLs enable transport of reactants into the areas under the flow channel ridges. Functions and material requirements of each component are discussed in detail in the following subchapters.

Theoretical output voltage of a unit cell is ca. 1.2 V, but due to the overpotentials, it drops to ca. 0.7 V when current is drawn. For applications, unit cells are connected in series to increase output voltage. Electrical interconnection between the cells is made by bipolar plates, hence the name. An integrated assembly of series-connected unit cells is often called a fuel cell stack. A cross section of a stack is shown at the bottom of Figure 4. There exists a multitude of different unit cell and stack structures and designs for different applications and purposes.

---

[j] Porous transport layers are also known as gas diffusion backings (GDBs) and gas diffusion layers (GDLs). However, some authors call a part of the electrode the ‘gas diffusion layer’.

[k] In unit cells, bipolar plates are often referred to as flow field plates or current collectors.

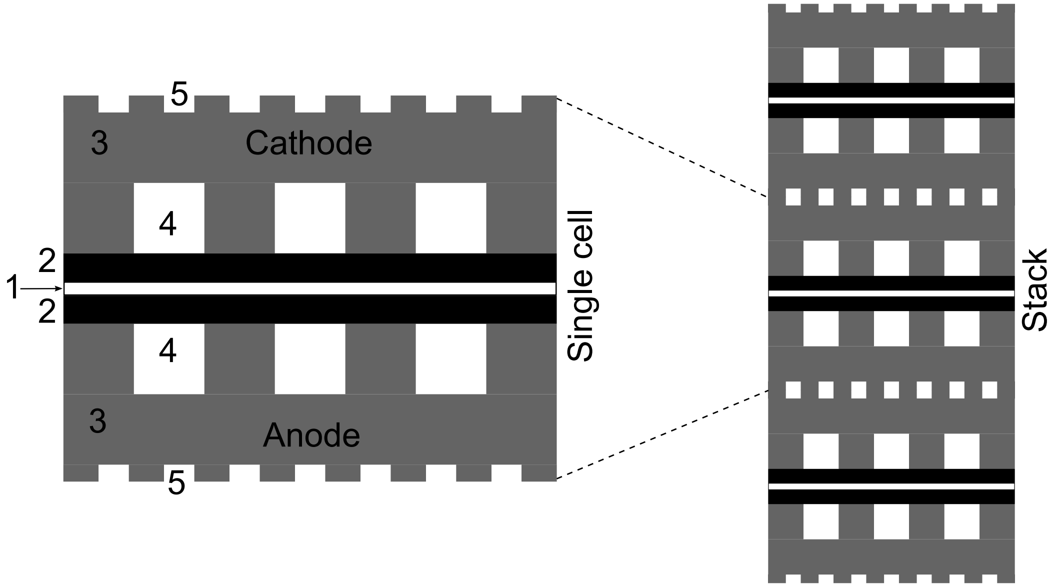

Figure 4: Cross section schematic of a PEM unit cell and a PEMFC stack. 1. MEA 2. porous transport layers 3. bipolar plates 4. reactant flow channels 5. coolant channels

The operating temperature of PEMFCs is restricted to between freezing and boiling points of water, since common electrolyte membranes need to be humidified to maintain proton conductivity, and full humidification is achieved only by contact with liquid water. Fuel cells can operate in temperatures below freezing, due to internal heat production, but freezing water may damage the membrane or other components when the fuel cell does not operate. Operating temperature range can be expanded beyond the normal range by pressurizing the system or by utilizing so-called high temperature membranes that maintain conductivity at higher temperatures.

Characteristic benefits of polymer electrolyte membrane fuel cells include fast startup, quick load following, and ease of electrolyte handling, low corrosion and system robustness due to solid electrolyte. Furthermore, it is possible to utilize waste heat from larger PEMFC systems, for example for service water heating in residential systems.

Low operating temperature involves also drawbacks. Presence of liquid water, required by the ionomer, complicates mass transfer – Water may flood parts of the system, rendering them inaccessible to oxygen, while scarcity of water lowers the proton conductivity of the ionomer. Furthermore, catalysts commonly utilized in PEMFCs are sensitive to even very low concentrations of carbon monoxide in the normal operating temperature range. Additionally, low operating temperature makes expulsion of waste heat problematic, if the ambient temperature is high. Increasing operating temperature beyond the boiling point of water would alleviate all these problems, since in addition to simplifying mass transfer and heat removal, platinum catalyst is more tolerant to carbon monoxide and reaction kinetics are more facile in higher temperature, and waste heat is more valuable.

PEMFC technology as such is almost ready for applications, but there are still issues to be solved before PEM fuel cells can successfully rival conventional technologies. Probably the most important outstanding question is cell durability and lifetime, which have not yet been demonstrated. Furthermore, the current price of both catalysts and ionomer materials is too high for competitiveness outside niche markets. Manufacturing and assembly cost per unit can be expected to decrease with mass production and advanced manufacturing methods, while catalyst and ionomer cost is more dependent on material development.

Polymer electrolyte membrane fuel cells are envisioned to replace internal combustion engines (ICEs) as vehicle power sources and to compete with conventional technologies in backup power systems, residential combined heat and power (CHP) devices and consumer electronics. Motivation for vehicle applications lies in the high efficiency even on partial load and low emissions at the time of use. Backup power systems have traditionally been based on either diesel engines, which are noisy and polluting, or batteries, which are bulky. Fuel cell devices generally produce less noise than ICEs and surpass batteries in energy storage density after a given capacity.

3.2. PEMFC components

3.2.1. Ionomer membrane

A solid proton conducting ionomer membrane is used as the electrolyte in PEM fuel cells. The electrolyte conducts protons from anode to cathode electrode and prevents mixing and direct combustion of reactants. Most of the fuel cells utilize perfluorosulfonic acid (PFSA) polymer membranes, which consist of perfluorovinyl ether groups terminated with sulfonate groups incorporated onto polytetrafluoroethylene (PTFE) backbone. The most common membrane material is Nafion®. Other similar materials are for example Flemion® and Aciplex® (Asahi Glass Co. Ltd.), and GORE-SELECT® (W.L. Gore & Associates, Inc.). Main differences between these membranes are the lengths of monomer chains in the backbone and side chains [18]. Thickness of common membranes varies approximately between 15 and 200 μm, depending on the material and intended operating conditions.

Ionomer membranes for PEM fuel cells have to have high chemical and physical durability, high proton conductivity, and preferably low price. Current PFSA membranes are chemically and physically stable, but their conductivity depends strongly on the degree of humidification. Furthermore, best humidification is achieved by contact with liquid water, and therefore operating temperature is limited to the range where water exists in liquid form. Under very dry conditions or at temperatures above boiling point membranes lose absorbed water and conductivity drops drastically. Fully humidified, conductivity of common membranes can reach values from 1 to 10 S m^{-1} [18].

Current PEMFC membrane research concentrates on two main themes, high temperature membranes and alternatives to expensive PFSA materials, which are partially overlapping. High temperature membranes are the subject of intensive research and development efforts. A review of high temperature PEM fuel cells, including new ionomer materials, was published by J. Zhang *et al.* [19].

3.2.2. Electrodes

Electrochemical reactions in PEM fuel cells take place on the electrodes, which are manufactured directly onto the membrane, hence the term membrane electrode assembly or onto the porous transport layers[1]. PEMFC electrodes are very thin, only

---

[1] Due to the lack of established terminology, catalyzed porous transport layers are sometimes called gas diffusion electrodes.

ca. 10 µm, thinner than in other fuel cell types, and thus power density in PEMFC electrodes is higher compared to other fuel cells.

Kinetics of oxygen reduction reaction (ORR) in acidic environment at the cathode are relatively slow under normal operating temperatures, and therefore PEMFC electrodes have high effective area and contain noble metal catalysts. High effective area is attained by creating a highly porous three-dimensional structure, where the ionomer and catalyst are in contact with each other and accessible to the gas phase and electron conductor (a.k.a. three phase boundary), and the actual electrochemical reaction takes place on the catalyst surface.

Porosity is an essential property of a high performance electrode. Pores allow transport of reactants onto three phase boundary sites and removal of reaction product water. Porous structure is achieved by the preparation method or by adding a pore forming agent, which is later removed, into the mixture in the manufacturing phase.

Typically, a PEMFC electrode consists of a mixture of ionomer and platinum black suspended on carbon black particles (Pt/C catalyst). Average catalyst loading on an electrode is usually between 0.1 and 0.4 mg cm^{-2} for both anode and cathode.

Highest performance is achieved with platinum catalyst when using neat hydrogen, but unfortunately platinum is sensitive to carbon monoxide, which is often present in reformed fuel feeds. Even very small amounts of CO in the fuel stream, 5 to 10 ppm, cause a notable performance loss by blocking reaction sites on platinum surface [20]. CO tolerance can be improved by using alloyed and nonalloyed bi- and trimetallic catalysts, anode side air bleed, reconfigured anodes, and increasing operating temperature. Platinum alloy catalysts, of which PtRu alloy is the most common, enhance CO tolerance by facilitating CO oxidation. Under normal operating conditions, PtRu alloy catalysts can tolerate up to 100 ppm and nonalloyed PtRu catalyst up to 150 ppm of CO in the fuel stream, respectively [21 22].

Air bleed, i.e. injecting a small amount (1 to 6%-vol) of air into the fuel stream for oxidation of CO on the catalyst surface can improve CO tolerance [23], but selectivity for CO oxidation is low. Reconfigured anodes contain a secondary catalyst layer on the porous transport layer, which is specific for CO oxidation [24]. When used with air bleed, carbon monoxide is chemically oxidized into carbon dioxide before it reaches the electrochemical catalyst layer. With air bleed, reconfigured anodes with platinum catalysts electrodes can tolerate up to 100 ppm CO, and PtRu electrodes up to 300 ppm [25].

Carbon monoxide adsorption onto platinum surface decreases dramatically as temperature is increased [26]. An analysis of free energy for CO and H_2 adsorption suggests that CO tolerance increases by a factor of 20 when operating temperature is elevated to higher than 100 °C [27]. At 125 and 200 °C normal Pt/C catalyst tolerates 0.1 and 3% CO in the fuel stream, respectively, with no significant performance loss [27].

In addition to improving tolerance to impurities, current research efforts aim at decreasing noble metal loading in the electrodes. This is pursued by both increasing catalyst utilization ratio for existing catalyst materials, and developing new, noble metal free catalysts.

3.2.3. Porous transport layers

Porous transport layers have numerous functions in a PEM fuel cell. As the name suggests, they act as a conduit for reactant species, reaction products, electric current and heat. Furthermore, they provide mechanical support for the MEA, ensuring a sufficient electrical and thermal contact between the MEA and the PTL under the flow channels.

The porous nature of the PTL materials provides the reactants access to the parts of the electrodes that are under the flow channel ridges, and a passage for reaction product water from the electrode to the flow channel. Reactant transport is usually driven by diffusion and in some cases by convection and water removal by capillary action. Electric current passes trough the PTLs when electrons travel from the cathode to the anode electrode via an external circuit, and heat produced in the cathode reaction leaves the MEA mainly by conduction though the PTLs.

These functions set various requirements on PTL materials. Transport of reactants and reaction products calls for high permeability and suitable water management properties; the ratio of hydrophilic and hydrophobic pores has to be balanced to allow passage of species in both gaseous and liquid phases. Contact with the electrodes and mechanical compression require both chemical and mechanical durability, and high electrical and thermal bulk conductivity and low contact resistances are necessary to minimize ohmic losses and temperature differences inside the cell. Additionally, the material should be inexpensive in order to improve economic competitiveness of fuel cell systems. Many of these properties are interconnected and thus best performance is often achieved by carefully balancing different properties instead of optimizing one.

Traditionally, PEMFC porous transport layers have been made of carbon cloth, paper or felt treated with PTFE or similar fluorocarbon to increase hydrophobicity, i.e. to ensure that water does not fill all the pores. [28 29]. Many PTLs feature a microporous layer of carbon black and PTFE on one or both sides to improve water management properties [30 31]. If the electrodes are manufactured onto the PTL, Pt/C catalyst is bound onto the microporous layer or directly onto the PTL substrate by ionomer or ionomer/PTFE solution [32]. Instead of carbon cloths or papers, the use of metal webs, sinters, foams and micromachined thin films for PTLs has been suggested. Details of PTL materials, characterization and cost estimates are given in the literature [33 34 35] and in publication V.

Porous transport layers are a critical component in cell water management, and experiments and modeling have shown that majority of mass transfer losses occur due to limited oxygen diffusion through the cathode side PTL, especially when liquid water is present [36 38]. Diffusion of reactants and removal of excess water are affected by PTL porosity, pore size distribution and ratio of hydrophobic and hydrophilic pores, gas permeability and material thickness. It has been suggested that liquid is transported in micropores by capillary action, while gases diffuse through the hydrophobic macropores [38 39], which makes careful balancing of various properties crucial for high performance.

Reactant transport processes and water management are very complex and interconnected phenomena, which depend on operating conditions and cell geometry and assembly as well as PTL properties. An adequate link between PTL properties and fuel cell performance has not been established. Water management is discussed further in chapter 3.3.

3.2.4. Flow field plates

Flow field plates feature flow channels for reactant distribution over the active cell are and water removal, and provide an electrical interconnection between the porous transport layers and outer components. Furthermore, flow field plates conduct heat and provide mechanical support for more flexible cell components, such as PTLs and the MEA.

Flow field plates in a fuel cell stack are often referred to as bipolar plates, because they act as an anode side plate for one unit cell and cathode side plate for another, separating reactants and connecting adjacent cells electrically. Similarly, flow field plates of a single cell are sometimes called monopolar plates. A simple flow field plate is shown in Figure 5.

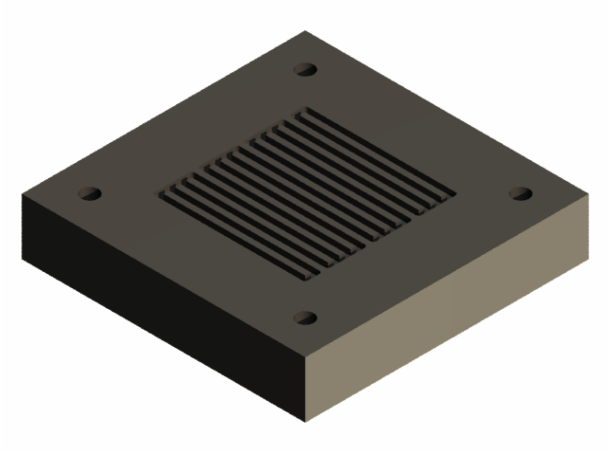

Figure 5: A simple flow field plate with a serpentine flow channel. Gas inlet and outlet are located on the opposite face of the plate.

Electrical and thermal properties have an effect on cell operation and performance. For minimizing ohmic losses in the flow field plate, electrical conductivity of the bulk material should be as high as possible and contact resistance between the flow field plate and adjacent components should be low. Electrical resistance of a flow field plate should be lower than 1 $\mu\Omega$ m^2 [34]. Thermal conductivity of bipolar plates determines the maximum area of unit cells, when passive cooling is used. For more efficient heat removal, coolant channels can be integrated into bipolar plates [40].

Chemical durability and low gas permeability are basic requirements for all flow plate materials. Flow field plates are exposed to a harsh chemical environment, and preventing hydrogen leaking and permeation to air channels is essential for fuel efficiency, cell performance and safety.

Besides performance, also economic aspects will play a role in the success of a flow field plate material. Bulk material should be readily available, inexpensive and lend itself to mass production techniques, e.g. injection molding. Additionally, low density will lead into lower stack weight, which is desirable from application manufacturers' point of view.

Common flow field plate materials include graphite, graphite composites, and stainless steel and other metals [41]. Resin-impregnated graphite has low gas permeability, and good electrical and thermal conductivity, but is expensive and unsuitable for mass production, e.g. injection molding or other melt processing methods. Flow channels have to be machined, which increases manufacturing costs.

Metallic materials are usually cheap, mechanically durable and flow channels can be stamped onto the plate, but often suffer from corrosion and high contact resistance due to oxides forming on the surface [42]. Therefore, coatings or surface treatments are necessary [43 44 45]. Composite flow field plate materials, which are being actively researched [e.g. 46 47 48 49], are a promising candidate due to suitability for melt processing, low gas permeability and sufficient conductivity.

A vital factor for flow field plate performance is flow channel geometry. Channel and ridge width, channel depth, surface properties and overall geometry all have an effect on reactant distribution and water removal. A myriad of different channel configurations exist, e.g. parallel, serpentine, spiral and interdigitated geometries with their single and multiple channel variations. There are also channelless designs that utilize a metal net or foam for reactant distribution [50 51]. There, the functions of flow fields and porous transport layers are combined into one component. Furthermore, reactant supply by natural convection and forced convection both need different flow field geometries. Several experimental and modeling performance studies have been published, for example by Birgersson and Vynnycky [52] or Yan *et al.* [53].

3.2.5. Other components

In addition to the core components introduced above, a number of other components are needed to make a functional unit cell or fuel cell stack. An exploded view of a simple unit cell is provided in Figure 6.

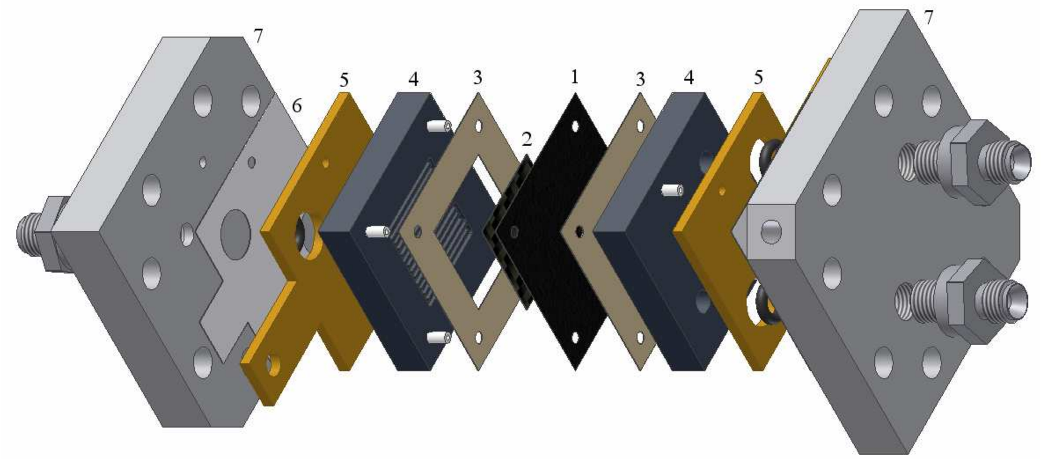

Figure 6: An exploded view of a unit cell. 1) MEA 2) PTL 3) Gasket 4) Flow field plates 5) Current collectors 6) Insulator 7) End plate. Clamping bolts are omitted from the figure.

Gaskets, either separate or integrated into other components, prevent leaks and accidental mixing of reactants. Common gasket materials include PTFE, VDF, EPDM and other thermoplastic polymers that can endure the harsh conditions in a fuel cell.

If connecting current leads directly into flow field plates is unfeasible, separate current collector plates are used. They are placed at both ends of the cell or stack and have terminals for current leads. Corrosion resistant, high conductivity materials are suitable for current collector plates.

Single cells and fuel cell stacks are held together by the end plates and clamping bolts or similar structures. They provide mechanical support and exert the required compression for sealing and electrical and thermal contact between the components. High rigidity is required from the end plates, since buckling under stress will lead into uneven compression, which in turn causes problems with gas tightness and electrical and thermal contact between components. In order to reduce the number of components, the functions of the end plates and current collectors are sometimes combined. The end plates are made of a rigid, conducting material, and current leads are connected into them. This requires insulating the clamping bolts from the end plates at least at one end to prevent short circuiting the cell.

To facilitate thermal management, cooling plates are often integrated into fuel cell stacks. They are sandwiched between bipolar plates that have been divided in two parts and feature channels for coolant circulation, see Figure 4. Alternatively, cooling plates can be made of high conductivity materials and feature cooling fins for heat removal outside the flow field area. With this arrangement, efficiency of heat removal is highly dependent on the thermal conductivity of the plate material.

On system level, more components are needed. The number and type depend on the system in question, but common components are reactant lines and storage units, reactant humidification systems, compressors or blowers, valves, pressure and flow controllers and control electronics, heating and cooling systems, and power conditioning units. If the fuel contains impurities or needs to be reformed, a separate fuel handling unit will be needed for extracting the hydrogen from the carrier.

Compressors supply the cell or stack with reactants, hydrogen and air or oxygen, and the control system takes care of flow and pressure control, purging, fuel recycling and so on. Before introduction the reactants into the stack, they are routed through a humidification subsystem it the reaction product water is not enough to keep the membranes well humidified. Reaction product water can be recycled for this purpose.

Heating and cooling systems maintain the stack temperature within the design specifications. At startup, the system can be heated externally until internal heat production can maintain the temperature, and during normal operation excess heat is removed through the cooling system. Excess heat can be expelled or used for reactant heating and humidification, or in external systems, e.g. space or service water heating.

The exact number and type of required auxiliary devices depends on the systems and application. For portable systems, the size and number of external systems is minimized by utilizing passive control where possible, but for large systems active controls are often more practicable.

3.3. Water management

Water management is one of the key issues for PEM fuel cells for achieving high performance, since it has an effect on both ionomer conductivity and reactant transport. Furthermore, these two effects compete with each other: Ionomer conductivity is maintained only under ample humidification, but presence of liquid water in the electrode and porous transport layers obstructs reactant transfer from the flow channels to the electrodes. Mass transfer problems caused by flooding are usually more severe in the cathode side, due to water production in cathode reaction, slower diffusion of oxygen and oxygen dilution by other inert species. Optimum performance is achieved by carefully balancing the amount of water inside the cell.

Water is produced in the cathode reaction and introduced into the cell with reactants if they are externally humidified. Water is transported in the flow channels and removed from the cell with the gas streams, either as vapor or liquid, depending on the concentration of water in the gas stream. Water can also permeate through the membrane by electro-osmotic drag, diffusion and hydraulic permeation. Electro-osmotic drag stands for the water flux from anode to cathode which arises from protons carrying water molecules along through the membrane. Diffusion and hydraulic permeation fluxes are driven by concentration and pressure gradients, respectively. The direction of these fluxes is usually from cathode to anode, but can vary in magnitude and direction over the active electrode area. Thinner membranes lead into larger diffusion and hydraulic permeation fluxes. Water fluxes inside a PEM fuel cell are illustrated in Figure 7.

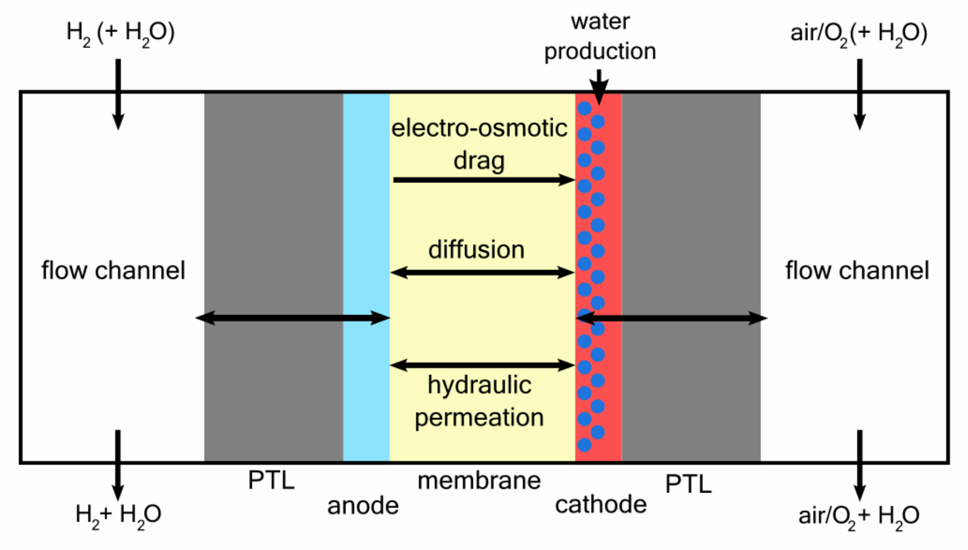

Figure 7: Water transport through the membrane in PEMFCs.

The direction and magnitude of local water flux depends on the local conditions, i.e. current density, temperature, reactant flow conditions, water concentration, component properties and cell geometry. These factors also have an effect on current density distribution in a cell, and these two are closely connected. Current density distribution is discussed further in chapter 3.4.

The objective of water management is to ensure sufficient ionomer humidification throughout the active area, while removing excess water that might obstruct reactant diffusion. Water removal from the cell can be actively controlled by regulating cell temperature, reactant flow rates and humidification. Passive control methods are based on cell design, i.e. flow channel geometry, flow directions, PTL material selection, MEA thickness etc. Active control methods require additional equipment and require power, thus reducing system efficiency. However, active controls can respond to changing external conditions better than passive control methods.

3.4. Current density distribution

Current density distribution, i.e. current production profile over the electrode area in PEM fuel cells is not homogeneous but distributed. Main causes for current density distribution are local variations in ohmic resistance and reactant transport, which in turn are caused by local variations in material properties and operating conditions [54 55].

Variation of ohmic resistance is caused by variations in ionomer hydration conditions and contact pressure between components. Local hydration conditions depend on the amount of liquid water in contact with the ionomer, which in turn depends on electrode and PTL properties, local temperature, and flow conditions in the flow channels. Changes in contact pressure have an effect on the electrical and thermal contact between the components and bulk conductivities of PTLs, which changes the ohmic resistance and temperature profiles in the cell. Transport of the reactant to the electrodes is controlled by the flow conditions in the flow channels and the properties and water content of the porous transport layers and the electrodes. Local variations in mass transport arise from changes in local conditions, for example temperature, and material properties, such as PTL permeability and thickness, which are different under the flow channel and under the flow field plate ridge.

Current density distribution occurs on three different scales. On the microscopic level, current production is uneven due to distribution of three phase boundary sites in the electrode and differences in reactant diffusion into the catalyst particle agglomerates. On millimeter scale, current production is uneven due to differences in mass transfer conditions and ohmic resistance. For example, diffusion path from the flow channel to the electrode is longer under the flow field plate ridge than under the channel, and permeability in the PTL under the ridge is lower due to compression. Similarly, contact resistance between the electrode and the PTL is higher under the channel than under the ridge. On cell level, reactant concentration drops and water concentration changes along the flow channel, reducing reactant supply to the electrode and changing humidification conditions, creating a cell level current density distribution. All these effects are interconnected and the severity increases with average current density.

Uneven current production profile can decrease cell life time or cause component failure due to local hot spots [56], or create dead zones where current production is significantly below the average. This leads into less efficient use of catalyst material and cell area, and thereby into suboptimal performance. The methods which can be used to optimize current density distribution and thereby cell performance are substantially the same that are used for water management, since the distribution of liquid water in the cell has a significant effect on the resulting current production profile. Current density distribution measurements, which are discussed further in chapter 5, are a valuable tool in improving fuel cell performance.

4. Fuel Cell Test Station

For the experiments described in Publications I, II and III, the same base components of the fuel cell test station were used. The test station was a commercial one, GlobeTech GT-100 Fuel Cell Test Station, consisting of a gas control unit (GlobeTech, Inc., incorporated into ElectroChem Inc.[m]) and an electronic load unit (Scribner Associates, Inc.[n]). A PC acts as a system controller and data logging unit. A block diagram of the test station is presented in Figure 8. The test station was augmented with auxiliary components and devices as required by different experiments.

The gas control unit feeds hydrogen, and air or oxygen, into the fuel cell. Reactant flows are controlled by MKS Type 1179A Mass-Flow® Controllers (MKS Instruments, Inc.). The gas control unit has bubble type humidifiers for each reactant gas, which can be bypassed if dry reactants are desired. Furthermore, the gas control unit is equipped with back pressure regulators for controlling reactant pressure in the fuel cell. Reactant gases are supplied from pressurized cylinders. Additionally, nitrogen from a pressurized cylinder is used for purging gas lines.

The load unit is a Scribner Series 890 Fuel Cell Load Unit (Scribner Associates, Inc.), rated for 100 watts. The unit acts as the electronic load either in galvanostatic, potentiostatic or constant power mode. A temperature control system, which consists of a thermocouple, PID controller and two electric heating cartridges, is integrated into the unit. The unit also features a built-in current interruption circuit, which enables measuring the ohmic resistance of the fuel cell, which is discussed further in chapter 5.

The test station is controlled by a PC running FuelCell® software (Scribner Associates, Inc.) for system control and data logging. The PC communicates with the load unit via a GPIB interface and the load unit transmits the control signals to the gas control unit.

Base measurement procedures and practices are based on the operational experiences and accumulated knowledge of the Advanced Energy Systems fuel cell group at the Helsinki University of Technology, and are detailed elsewhere [57 58 58 60]. Detailed descriptions of operating conditions, e.g. cell and humidification temperatures, reactant pressures and auxiliary systems and devices for each experiment are presented in their respective chapters.

---

[m] Electrochem, Inc., 400 W. Cummings Park, Woburn MA 01801, USA

[n] Scribner Associates, Inc., 150 E. Connecticut Avenue, Southern Pines, North Carolina 28387, USA

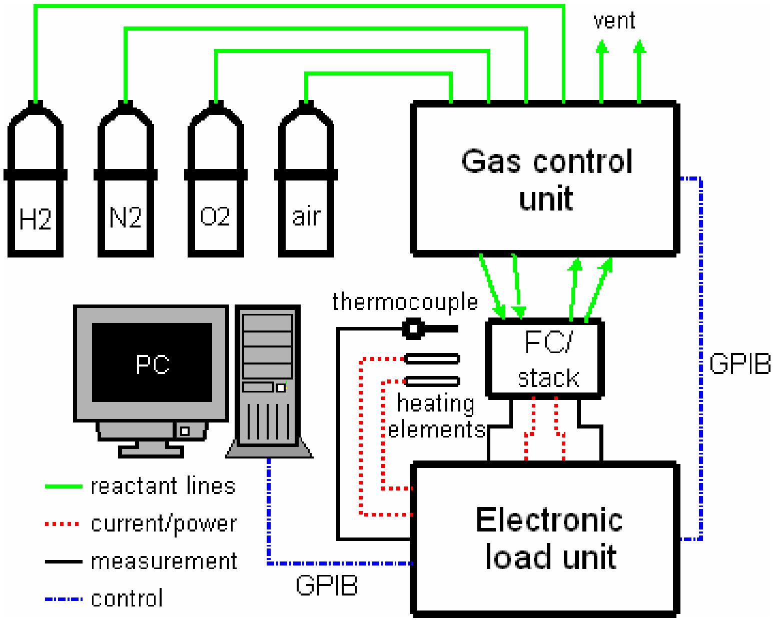

Figure 8: Block diagram of the test station

5. Current Interruption Measurements

5.1. Background

Resistance measurement is an important performance analysis and diagnostic tool which can be applied on an operating fuel cell. High resistance after cell assembly may be an indication of improper alignment of components, leading into high electrical contact resistances. Increasing or decreasing resistance during cell operation is usually an indication of changes in water management, since the conductivity of the ionomer membrane is dependent on its hydration state. Complementing the voltage measurements of unit cells in a fuel cell stack with resistance measurements yields more information on the operation of the stack and its individual cells and possible problems than voltage measurements alone. However, measuring fuel cell resistance is not trivial, since fuel cells contain both protonic and electronic conductors. Furthermore, different overpotentials overlap, making it difficult to distinguish ohmic losses from other overpotentials difficult.

The current interruption method, which has been discussed in several publications [61 62 63 64], for measuring fuel cell resistance is based on the fact that different overpotentials dissipate at different rates after current interruption. In a PEMFC, ohmic overpotentials dissipate in less than 0.5 ns, whereas the dissipation of electrochemical overpotentials takes significantly longer, at least 10 ns [63]. By rapidly interrupting the current and observing the resulting voltage transient, the magnitude of ohmic losses can be estimated from the difference of potentials immediately before and after the current interruption. The principle is illustrated in Figure 9.

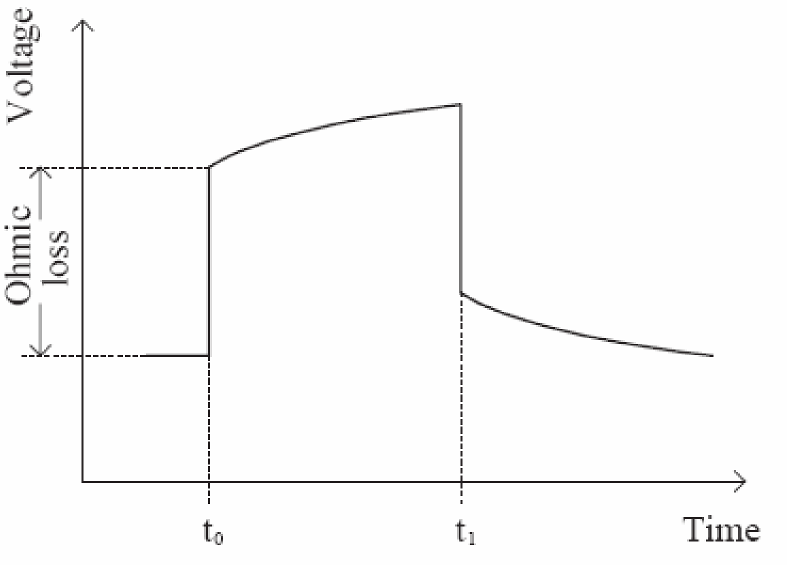

Figure 9: The principle of resistance measurement by current interruption method. The current is interrupted at t_0. Ohmic losses dissipate almost instantaneously and voltage increases rapidly ($\Delta V_{ohmic} = RI$). After that, electrochemical losses start to dissipate. At t_1, the current is switched back on. Ohmic losses set in very rapidly and electrochemical losses at a slower rate.

Implementing the current interruption method requires the use of a fast switch to interrupt the current for a brief moment. Alternatively, an auxiliary current pulse can be fed into the system under scrutiny. The resulting voltage transient is similar to that in Figure 9 but inverse, i.e. voltage drops rapidly when the pulse is applied. This approach has been found to give more accurate results at higher currents [63 64], where rapid interruption of current is difficult to implement.

In practice, measuring the rapid transient accurately is complicated. Due to the inductances of the measured system and the measurement equipment, and the nonideal electronic components, the voltage signal is obscured by noise, and an overshoot and oscillations immediately after the current interruption. These disturbances are present also in high-quality devices and circuits built for current interruption measurements [63]. An example of a recorded voltage transient is presented in Figure 10. The equipment used was not optimized for current interruption measurements and thus the voltage transient is notably slower than that mentioned in reference [63].

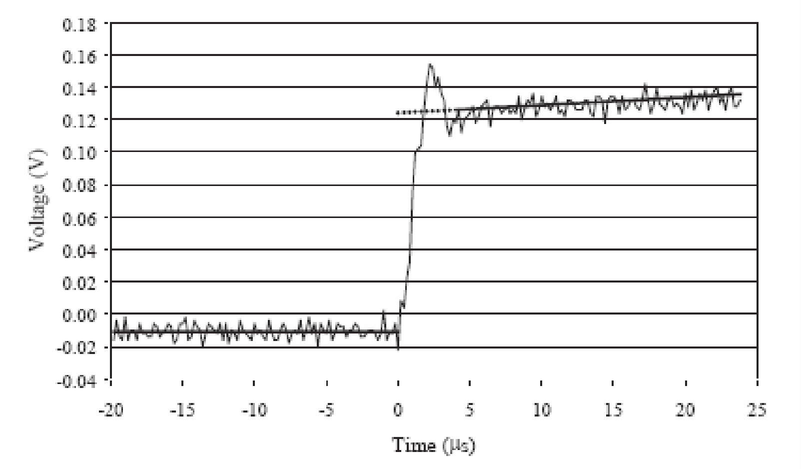

Figure 10: Real voltage transient from a current interruption measurement. DC components have been subtracted from the voltage signal.

Post-interruption overshoot and oscillations last notably longer than the dissipation of ohmic losses, see Figure 10. Therefore using a voltage value recorded after the voltage has stabilized would probably lead into overestimation of resistance, since some of the electrochemical losses have dissipated by that time. In this work, an estimate for the voltage value after the current interruption was obtained by the following procedure: A linear fit was made into the voltage data after the oscillations had decayed and the line was extrapolated back to the moment of current interruption. The ohmic loss was calculated as the difference between this value and the averaged voltage before the current interruption. While not accurate, linear extrapolation will yield better results than using a voltage value recorded either during the overshoot and oscillations or at a later time, when also some electrochemical losses have dissipated. While the transient is exponential in nature after the initial rapid change, linear extrapolation was used because the overshoot and oscillations obscured the area of the transient which is critical for accurate exponential fit. With specialized equipment, the disturbances can be controlled better and exponential fits can be used in stead of linear ones for improved accuracy [63].

An alternative method for measuring cell resistance is electrochemical impedance spectroscopy (EIS), which is based on concurrent observation of cell voltage and current when steady state is perturbed by a small AC signal applied to the system, and subsequent study of phase difference. For interpretation, an equivalent circuit is fitted to EIS data or a set of differential equations describing the system is used, which makes EIS less straightforward than the current interruption method. On the other hand, EIS yields also other information in addition to cell resistance. Current interruption data can also be analyzed using the same methods as for EIS data, if the data is Fourier-transformed into the frequency domain [65].

In Publication I, the current interruption method was applied to a fuel cell stack, a successful measurement series demonstrated and error sources are discussed. The method was first mentioned by D. Webb and S. Møller-Holst [66], but no results were presented. The method used here is an improvement on the previous work of the author [60], and is faster, simpler and provides more accurate results.

5.2. Experimental setup

The experiments were carried out using the test station described in chapter 4 and a commercial four-cell fuel cell stack[o], each cell having an active area of 25 cm^2. The cathode side flow channels were open to surrounding air, enabling air supply both by free convection and the use of an external fan. Figure 11 is a picture of the stack.

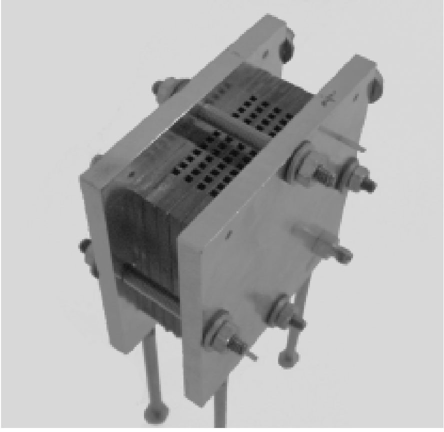

Figure 11: The stack used in current interruption measurements.

The current interruption function was provided by the load unit and the voltage transients were recorded using a TDS-320 digital oscilloscope. The anode end of the stack was connected to ground through the load unit, and therefore the oscilloscope had to be disconnected from ground. Otherwise connecting the counter probe, which is grounded through the oscilloscope, in the middle of the stack would have created a parallel path to ground, severely distorting the results. Therefore, the oscilloscope was powered through an isolating transformer.

The stack was operated without external heating and fed with dry hydrogen at constant stoichiometry of 1.5. Ambient temperature and relative humidity were ca. 22 °C and ca. 20%, respectively. When operating on free convection, measurement series were carried out at 100, 150 and 200 mA cm^{-2}. For forced convection, a fan was placed under the stack and air flow directed into the flow channels using a cardboard housing. The fan operated at a constant power of 1.2 W. Compared to the case of free convection, the forced air flow provided some additional cooling. With forced convection, measurements were carried out at 50 mA cm^{-2} steps from 100 to 400 mA cm^{-2}. During the experiments, stack temperature was observed with a thermocouple sensor located in the flow field plate at the cathode end of the stack. Individual cell voltages were monitored with an Agilent 34970A data logger.

---

[o] BCS # 25-4-29X, BCS Fuel Cells, Inc., 2812 Finfeather Road, Bryan, TX 77801 USA

At each current density for both free and forced convection cases, the stack temperature and voltage were allowed to stabilize, after which a sequence of measurements were performed. First, a full stack voltage transient was recorded, followed by voltage transient measurement from each unit cell. Last, a second full stack transient was recorded in order to check for possible changes in the state of the stack conditions. Stack and unit cell voltages, and stack temperature were also recorded during the transient measurements. If any of the recorded quantities changed in a notable way, the data was discarded and the measurement sequence was repeated.

5.3. Results and discussion

Measured ohmic losses and unit cell voltages under forced convection are presented in Figure 12. As current density was increased from 100 to 400 mA cm^{-2}, the ohmic loss in the middle cells of the stack increased compared to end cells. At maximum current density, resistance of the 3rd cell from the anode end of the stack was 21% higher than that of the 1st cell. However, measurement of unit cell voltages reveals that the performance of cell 3 was equal to that of cell 2 and second to only cell 1.

The most likely reason for uneven ohmic loss profile was uneven temperature distribution in the stack. Temperature of the middle cells was probably higher than at the ends of the stack, which led into increased evaporation, convection and reaction rate. Improved water removal could not be compensated by water production on the cathodes, which caused incipient drying out, but on the other hand facilitated oxygen diffusion to the electrode compensating for the increase in ohmic loss. Reliance on voltage data only would not have revealed that cells in the middle of the stack were actually on the verge of drying out.

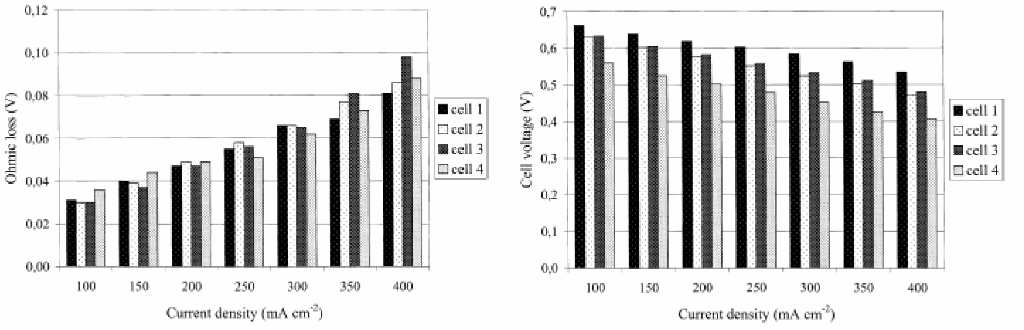

Fig. 12. Measured ohmic losses in individual cells. Air supply: forced convection.

Fig. 13. Individual cell voltages during the measurement of ohmic losses. Air supply: forced convection.

Figure 12: Ohmic losses (left) and unit cell voltages (right) measured from the stack under forced convection.

Figure 13 presents the comparison of full stack resistance measurements before and after the unit cell measurement sequence against the sum of unit cell resistances under forced convection. Measurements indicate a good agreement between the individual readings and full stack measurements, which further supports the applicability of the current interruption method for unit cell resistance measurements.

Some features of Figure 13 warrant further discussion. The curve of the sum of unit cell resistances seems to be smoother than that of full stack measurements, which contains more scatter. This scatter is probably explained by the extrapolation process. When the measured voltage transient is larger, as it is with the full stack compared to a unit cell, also the overshoot and oscillations are more pronounced. This will add uncertainty to the extrapolation and thus cause scatter in the resistance calculation results. This uncertainty in full stack measurements will probably increase with stack size.

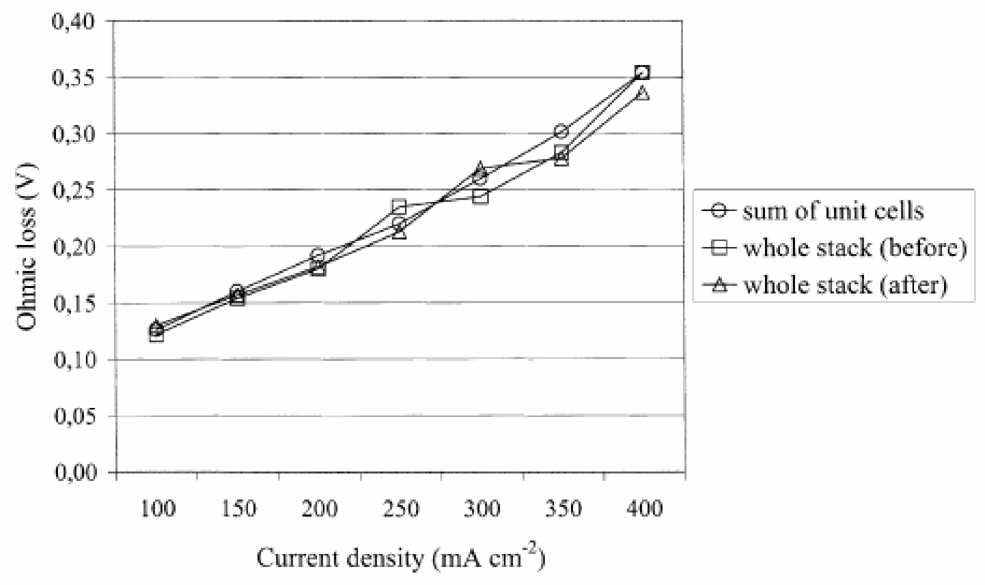

Figure 13: Comparison between full stack resistance measurements and sum of unit cell measurements.

Examining the raw voltage transients recorded with the oscilloscope revealed that the post-interruption transient and subsequent oscillations last 3 to 4 μs, which is considerably more than the time scale for the dissipation of fastest electrochemical losses. Therefore, extrapolation of voltage back to the moment of current interruption is necessary, and was implemented when analyzing data from the experiments. Specialized low inductance circuits are needed to cut the duration of perturbations after the current interruption.

Pre-interruption voltage average as well as post-interruption linear fitting was performed over a period of 20 μs. Conservative estimates for sampling rate and standard deviation, 2 MHz and 5 mV, respectively, give a standard error of the mean of less than 2 mV for ohmic loss. As a relative error, that is less than 10% even in the worst case.

Another error source is the linear extrapolation. As discussed by Büchi *et al.* [63], the extrapolation should be done by fitting a logarithmic curve to the transient, but due to the amount of noise and oscillations, a linear fit was used instead. Based on the results presented by Büchi *et al.* [63] and Büchi and Scherer [64], transients display logarithmic behavior during the first microsecond after the current interruption, whereas the fit used here starts 2 to 3 μs later. Judging from their data, a linear fit exaggerates ohmic loss by some millivolts. Furthermore, the error is systematic and thus comparing ohmic losses of different unit cells should be feasible.

6. Measurement of current density distribution in a free-breathing PEMFC

6.1. Background

Current density distribution in fuel cells is seldom uniformly distributed throughout the active area, and furthermore, there are often differences in the current density distribution from cell to cell in a fuel cell stack. Uneven current production stems from the varying reactant availability and contact pressure distribution, humidity and temperature profiles across the electrode surface. The causes of uneven current density distribution and common solutions are discussed in detail in chapter 3.4.

Uneven current density distribution leads to uneven power production distribution, which leads into suboptimal use of active area and larger cell size. Furthermore, uneven power production distribution may create hot spots or other phenomena harmful to power density or lifetime. Larger PEMFC systems often use auxiliary devices, e.g. humidifiers and blowers, to keep the system performance optimal. However, with small devices, system mass and footprint are paramount, making the use of auxiliary devices undesirable. Minimizing the number of system components requires the introduction of passive control methods for reactant delivery and temperature and humidity control. This can be accomplished with careful cell design and selection of materials.

Oxygen transport in free-breathing fuel cells occurs by diffusion and convection. Diffusive transport is driven by concentration gradients, while the driving forces of convective transport are the buoyancy effects caused by heating and concentration changes, i.e. density changes of air in the cathode flow channels. Of these two, convective transport is clearly dominating over diffusion under common operating conditions [67]. Convective mass transport is strongly dependent on the temperature difference between the cell and ambient air. Higher temperature difference improves oxygen transport by increasing air flow rate, but also enhances water removal due to increased evaporation and convection, which may lead into drying out.

Several methods for measuring the current density distribution in an operating fuel cell can be found in the literature. They are based on either a segmented current collector on one side of the cell or on sensing the magnetic field produced by electric current using e.g. Hall sensors. Segmentation of the current collector can be achieved in a variety of methods, e.g. by embedding conducting elements or Hall sensors in a non-conducting frame [68 69 70 71 72 73 74 75 76], or by a printed circuit board approach [77]. Each approach has their benefits and disadvantages.

In publication II, an apparatus for measuring the current density distribution in a free-breathing fuel cell is presented. The device is based on the segmented current collector approach and will be discussed in detail in the next subchapter. To the knowledge of the authors, publication II was the first paper presenting current density distributions measured from a free-breathing fuel cell.

6.2. Experimental setup

For current density distribution measurements described in publication II, the fuel cell test station described in chapter 3.1 was augmented with a special cell with a segmented cathode current collector. The anode side components of the cell, an end plate, current collector and single channel serpentine graphite flow field plate, were taken from a commercial 25 cm^2 cell by GlobeTech. Cathode side components were in-house production. GORE PRIMEA® Series 5510 MEAs and ®SIGRACET GDL 10 H PTLs by SGL Carbon AG were used in the experiments.

The flow field plate was made of PVC plastic, with 13 parallel channels open to ambient air machined into it. The cross section size of each channel was 3 mm by 3 mm. 48 gold plated stainless steel current collector segments were embedded into the flow field plate to form ridges between the channels. The size of each segment was 1 mm by 10.5 mm and they were arranged in 4 (vertical) by 12 (horizontal) pattern. Small gaps existed between the current collector segments and the PVC ridges. They allowed air flow between adjacent channels, but since the main gradients driving mass transport are in the vertical direction, mass transport between channels was assumed negligible. Each current collector segment was connected to a 0.1 Ω resistor for current measurement. Unlike the current collector, the PTLs and the MEA were not segmented. The cathode side current collector is shown in Figure 14 and details about the structure in Figure 15.

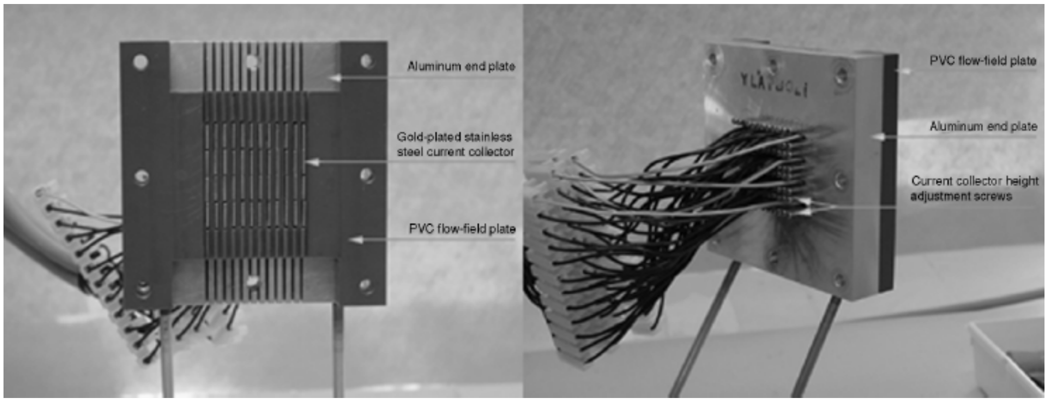

Figure 14: The segmented cathode current collector plate with end plate and current wires.

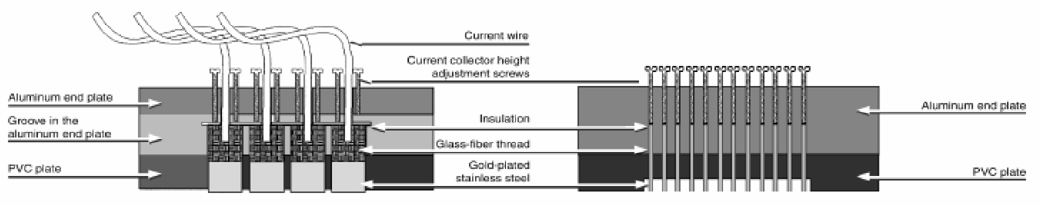

Figure 15: Detailed schematic sections of the segmented cathode current collector plate.

Individual height control of each current collecting segment allowed device calibration for every measurement series. Before starting the experiment, the cell was operated at a low average current density, less than 50 mA cm^{-2}, and the current density of each segment was measured. If notable deviations from the average were detected, they were corrected by adjusting the position of the segments in question. At low average current density, mass transport was expected not to cause local differences in current production and thus complicate the calibration procedure.

For demonstrating the measurement system, current density distributions were mapped at four temperatures (ambient, 45, 60 and 75°C) and two average current densities (100 and 200 mA cm^{-2}). Ambient temperature, in this case, means that the cell was not heated externally. However, heat produced by the cell reaction maintained the cell slightly above the ambient air temperature. At each measurement point, the cell was heated to the desired temperature and allowed to stabilize at 100 mA cm^{-2} for 15 minutes. Current density distribution was recorded for 15 minutes, followed by a polarization curve measurement.

The cell was not actively humidified. The hydrogen fed into the cell was dry, and the only water sources were the ambient air and reaction product water. Due to these conditions, humidity on the cathode side increased towards the top of the cell, due to water production on the cathode electrode. On the anode side, which was humidified only by water diffused from the cathode, hydrogen humidity increased towards the outlet, which was near the segment (12,1).

6.3. Results and discussion

Figure 16 to Figure 18 present current density distributions measured at ambient temperature, 60°C and 75°C at an average current density of 100 mA cm^{-2}. This measurement series illustrates many aspects of mass transfer in free-breathing fuel cells.

In Figure 16 to Figure 18, numbers on the x- and y-axes represent the location of current collector segments, x-axis being horizontal and y-axis vertical. The arrow in the figures indicates the direction of air flow, thus pointing towards the top of the cell. Hydrogen inlet was located near the (1,4) segment. During the measurements, ambient temperature and humidity varied between 25.2 to 28.5°C and 48.2 to 50.3%, respectively.

At ambient temperature, see Figure 16, the average current density in the bottom part of the cell is three times higher than in the top part, and 50% above the average. At 60°C, Figure 17, the current density distribution shows a more uniform quality, with an observable drop near the hydrogen inlet. At the highest temperature, 75°C, see Figure 18, the distribution is very different (Note the different viewing angle). The majority of the current is produced in the upper corner of the cell, away from the hydrogen inlet, and the lower part is nearly dead.

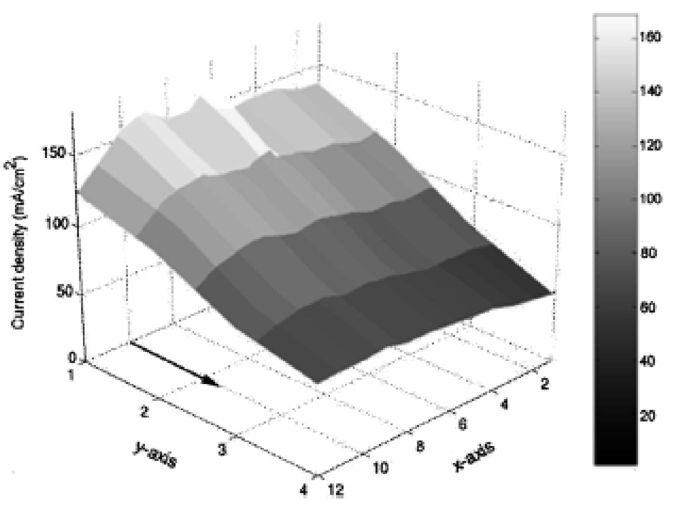

Figure 16: Current density distribution at ambient temperature (ca. 27 °C), at an average current density of 100 mA cm^{-2}.

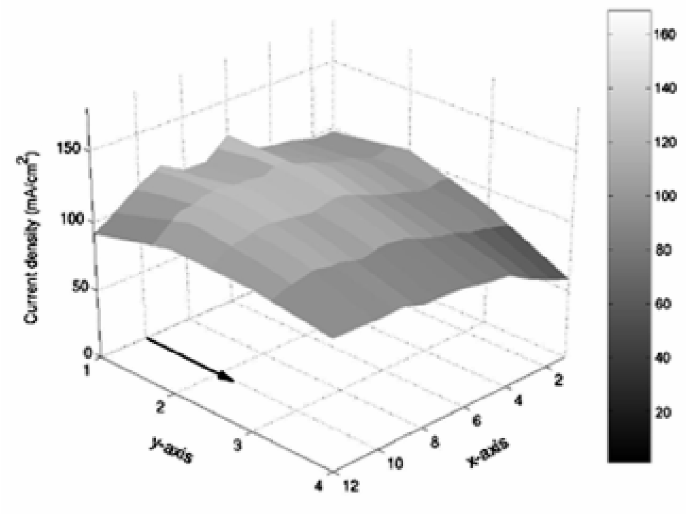

Figure 17: Current density distribution at 60 °C, at an average current density of 100 mA cm^{-2}.

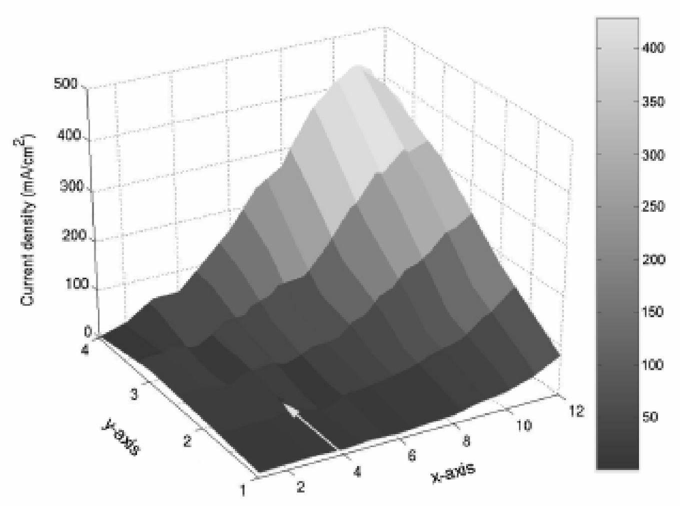

Figure 18: Current density distribution at 75 °C, at an average current density of 100 mA cm^{-2}.

Together with polarization and resistance curves, shown in Figure 19 and Figure 20, respectively, current density distribution graphs provide enlightenment on the conditions at different parts of the cell. At ambient temperature the cell is heated only by the cell reaction. The small temperature difference between the cell and ambient air, combined with concentration gradients in the flow channels, is not enough to provide sufficient amounts of oxygen to the upper parts of the cell. Oxygen transport was further impeded by liquid water accumulation in the flow channels, which is evident from the polarization curve and was confirmed by visual inspection. Thus, the current density is highest at bottom of the cell. Resistance measurements indicate that the cell does not suffer from drying out under these conditions. At 60°C, buoyancy effect of air in the flow channels is strong enough to keep the oxygen concentration relatively uniform along the flow channel, thus the current density distribution is smooth. However, the corner of the (1,4) segment is producing less current than other parts of the cell, which is an indication of beginning drying out of the cell. Dry hydrogen was fed into the cell near the segment (1,4) which lead into local drying out the water vapor accumulation in the flow channel cannot compensate for.

At 75°C, the current density distribution is very different. Most of the current is produced in the top part of the cell, away from the hydrogen inlet. Increased cell resistance, see Figure 20, is an indication of severe drying out. High operating temperature leads into enhanced mass transport, i.e. increased air flow in the channels and evaporation, resulting in membrane drying out. Water vapor content of air is at maximum at the upper part of the flow channel due to accumulation of reaction product water, thus the top part of the cell was better humidified, and produced more current than the bottom part. The effect of feeding dry hydrogen into the cell is clearly visible: The area close to the hydrogen inlet is nearly dead, even if it is located at the top part of the cell, despite water diffusion from the cathode to the anode.

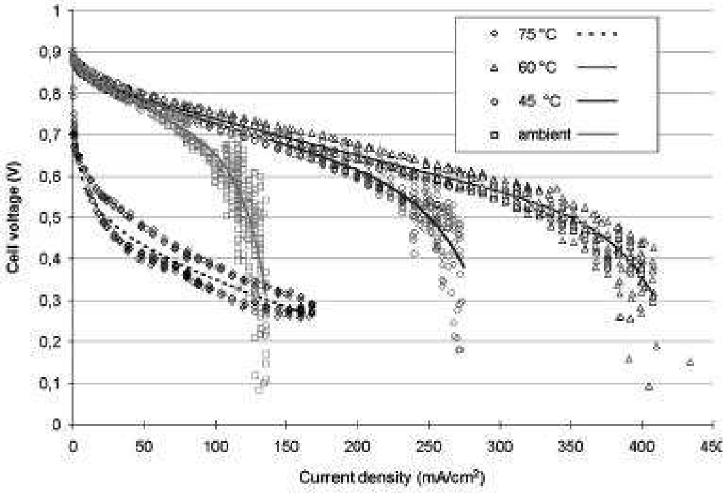

Figure 19: Polarization curves at ambient temperature, 45, 60 and 75 °C.

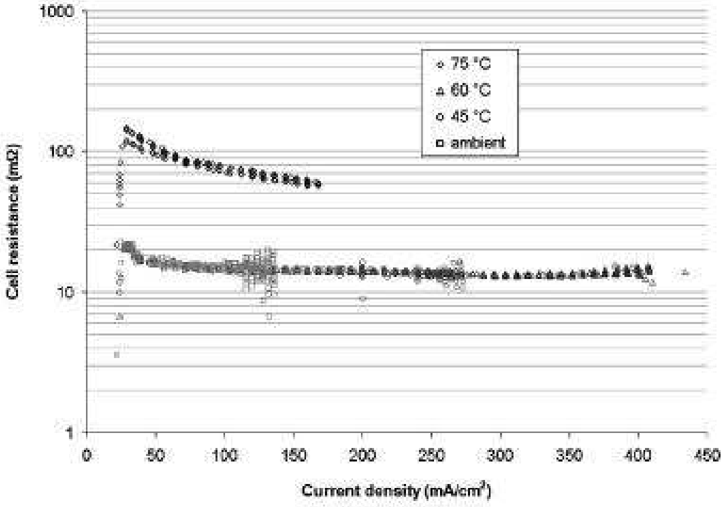

Figure 20: Cell resistance as a function of average current density at ambient temperature, 45, 60 and 75 °C.

The results presented here and in publication II are naturally quantitatively valid only for the hardware used, but they demonstrate on qualitative level the problematics of oxygen transport and water management in free-breathing fuel cells. At low temperatures the performance limiting factor is oxygen transport. The upper part of the cell suffers from oxygen starvation, thus the lower part performs better. At 60°C, the temperature difference between the cell and the surrounding air is large enough to drive a sufficient amount of air through the cathode channels to provide oxygen for the cathode reaction. At the same time, water removal is balanced with water production, keeping the membrane adequately humidified everywhere in the cell. Under these conditions, the current density distribution is the most uniform. At the highest temperature water removal is excessive, rendering most of the cell area useless and creating very high local current densities in certain locations. Current density distribution is mainly caused by the local variations in membrane conductivity, not the concentration of reactants as in the first case. It was thus concluded that 60°C was the optimal operating temperature among those tested.

The effect of varying contact force between the current collector segment and the porous transport layer can be seen in Figure 16 and Figure 17. Segments (6,1) and (8,1) had better contact to the PTL than surrounding segments. Since current seeks the path of least resistance, higher current was measured from those segments, with lower results for adjacent segments. In the graphs this can be seen as peaks in corresponding locations with depressions around them.

The current density distribution mapping device has been used in the laboratory of Advanced Energy Systems to further study the effect of operating conditions [78] and cell orientation as well as the driving forces of free convection [67]. Furthermore, measurement methods utilizing this device for measuring overpotential distributions have been developed [79].

The results described above are based on the assumption that the effect of non-segmented MEA and PTLs was minor. However, later studies [80] have shown that the use of common electrodes with segmented current collectors will significantly affect the current density distribution under potentiostatic operation due to variations in contact resistance between the current collectors and the PTL. While the results and conclusions above are most probably qualitatively correct, care must be taken when interpreting data from current density distribution measurements where common electrodes and PTLs have been used.

7. Titanium sinter as porous transport layer

7.1. Background

Implementing passive control systems can be used to reduce fuel cell system weight and size by reducing the number of auxiliary systems needed. For example, air fans or blowers and humidification systems can be dispensed with if oxygen is supplied to the cathode side by free convection. In this approach, cathode channels are open to surrounding air, or the whole cathode structure is channelless. These so called free-breathing cathode structures are simpler and thus cheaper to manufacture than traditional forced convection flow field plates with machined flow channels.

Implementing channelless cathode structures with traditional PTL materials is challenging. Flexible carbon cloths and papers need supporting ridges for maintaining sufficient electrical and thermal contact with the electrode. More rigid PTL materials would make large cathodes open to surrounding air possible. In the literature, the use of metal foams, sinters and nets as porous transport layers, flow fields or both has been suggested [50 51 81 82 83]. Benefits of these materials include unchanged porosity under compression due to high rigidity, and high thermal and electrical conductivity.

Metal foams, sinters and nets can also be used for replacing PTL and flow channel structures in forced convection cells, either in channelless structures which are simpler to manufacture than current channel structures, or channels can be manufactured directly on the PTL. Rigidity also enables the use of higher compression in cell assembly to ensure electrical and thermal contact between the components.

In publication III, the applicability of titanium sinter as porous transport layer for PEMFCs was evaluated. Testing was carried out in a forced convection cell, and special emphasis was given to contact resistance issues.

7.2. Experimental Setup

The test station used for the experiments was described in chapter 4. 0.5 mm thick titanium sinter PTLs were fitted into a 25 cm^2 commercial single cell, either on the anode or cathode side. Commercial carbon paper was used as a reference material for performance comparison. In addition to untreated titanium sinter, titanium sinters with two coating materials, platinum and carbon, were tested. Coating thicknesses were 5 and 10 nm for platinum and 10 nm for carbon. Coatings were prepared by evaporation method. The porosity of the titanium sinter was 32% according to a mercury intrusion porosimetry measurement.

The effect of PTL materials was investigated by recording polarization curves in galvanostatic mode, accompanied with resistance measurements by built-in current interruption feature of the test station. Curves were measured following a 20 minute stabilization period at 100 mA cm^{-2}. Cell temperature was 50 °C. The flow rates of hydrogen and oxygen consisted of constant base flows of 26 and 62 cm^3 min^{-1}, respectively, and variable flows of 10 and 25 cm^3 min^{-1} per ampere, respectively. If air had been used instead of oxygen, the flow rate would have corresponded to a stoichiometric factor of ca. 1.5. However, pure oxygen was used instead of air, giving a stoichiometric factor of 7.2. Excessive oxygen flow rate was used in order to achieve water removal conditions corresponding to operation on air.

Each PTL material was tested on both anode and cathode side of the cell, with commercial carbon paper PTL of the other side. For reference, a polarization curve was recorded when carbon paper PTL was used on both sides of the cell.

7.3. Results and discussion

Polarization curves recorded when uncoated titanium sinter was used as PTL on one side of the cell are presented in Figure 21. For reference, a polarization curve measured with a conventional carbon paper PTL assembled in the cell is also shown. It is clearly evident that using a titanium sinter as PTL on either side of the cell gave rise to a notable performance loss compared to conventional PTLs. Performance loss was more severe when titanium sinter was on the cathode side.

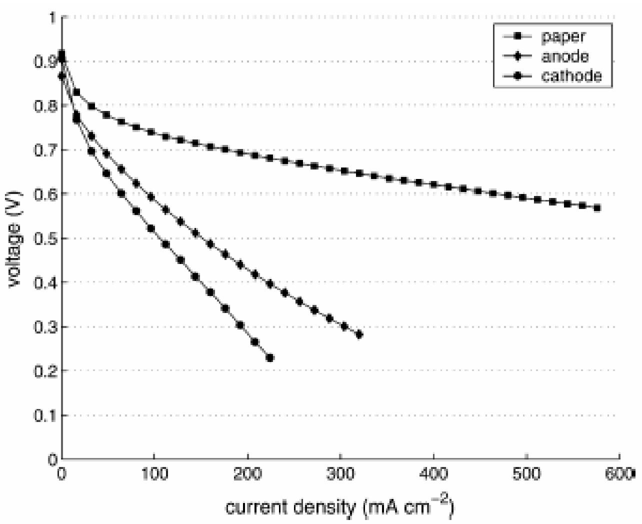

Figure 21: Polarization curves recorded when using an uncoated titanium sinter as PTL on one side of the cell. "Anode" and "cathode" indicate the side the sinter was on, and "paper" refers to the reference measurement with carbon paper on both sides of the cell.

Explanation to performance loss was provided by resistance measurements, see Figure 22. Resistance curves show that the total cell resistance was ca. five times higher when titanium sinter was used as a PTL. Since the bulk conductivity of titanium sinter is high, the most likely cause for high resistance lies in contact resistance between the sinter and the electrode, and the sinter and the graphite flow field plate.

If high resistance was the only reason for performance drop when using a titanium sinter PTL, *IR*-compensated[p] polarization curves would overlap. However, this is not the case in Figure 22: While the *IR*-compensated "anode" curve closely follows the reference curve, the "cathode" curve still exhibits a performance loss, although cell resistances are equal in both cases.

This is probably due to mass transport problems caused by accumulation of liquid reaction product water in the pores of titanium PTL. This assumption is supported by the fact that performance loss that can not be explained by resistance increase occurred only when titanium sinter PTL was on the cathode side. Cathode reaction produces water, while water is supplied to the anode side only by diffusion through the membrane. Furthermore, dynamic viscosity of hydrogen is lower and diffusivity higher due to smaller molecule size. Thus, hydrogen transport in the sinter on the anode side is less impeded by loss of porosity than that of oxygen on the cathode.

---

[p] The voltage of *IR*-compensated polarization curves is compensated by the measured ohmic loss.

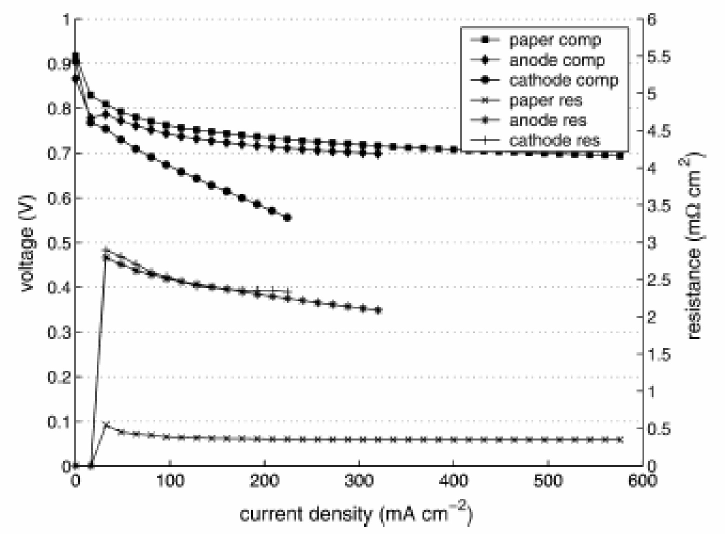

Figure 22: *IR*-compensated polarization curves recorded when using an uncoated titanium sinter as PTL on one side of the cell. "Anode" and "cathode" indicate the side the sinter was on, and "paper" refers to the reference measurement with carbon paper on both sides of the cell. "Comp" and "res" refer to *IR*-compensated polarization curves and resistance curves, respectively.

In the titanium sinter, both oxygen transport towards the electrode and removal of both liquid and gaseous water to the flow channels takes place in the pores. Water accumulation in the pores thus obstructs oxygen transport, rendering parts of the electrode inaccessible to oxygen. For carbon papers and cloths, a different mechanism has been suggested by Amphlett *et al.* [84]. Gaseous species, both reactants and reaction products, diffuse along the macropores in the material, while liquid water is transported by capillary forces in the micropores in the carbon fibers. Therefore, titanium sinters are more prone to flooding than conventional PTL materials, which are treated with non-functionalized fluorocarbons to increase hydrophobicity.

In order to reduce contact resistance, platinum and carbon coatings on the titanium sinter PTLs were tested. *IR*-compensated polarization curves recorded when coated titanium sinter PTLs were on the cathode side of the cell are shown in Figure 23. "Pt5", "Pt10" and "carbon" refer to 5 nm platinum coating, 10 nm platinum coating and 10 nm carbon coating, respectively. Platinum coating on the titanium sinter lowers the cell resistance ca. 60%, but carbon coating does not have a notable effect. Platinum seemed to bond well with the titanium surface, while the electrical connection between the carbon coating and the sinter was poor. Either the conductivity of carbon layer was low, or the contact resistance between the carbon coating and the electrode was high. Still, the total resistance of the cell in the case of platinum coating remains twice as high as in the reference case. Furthermore, since titanium sinters were coated only on the side towards the electrode, resistance drop would indicate that the contact resistance between the sinter and the electrode is significantly higher than that between the sinter and the graphite flow field plate.

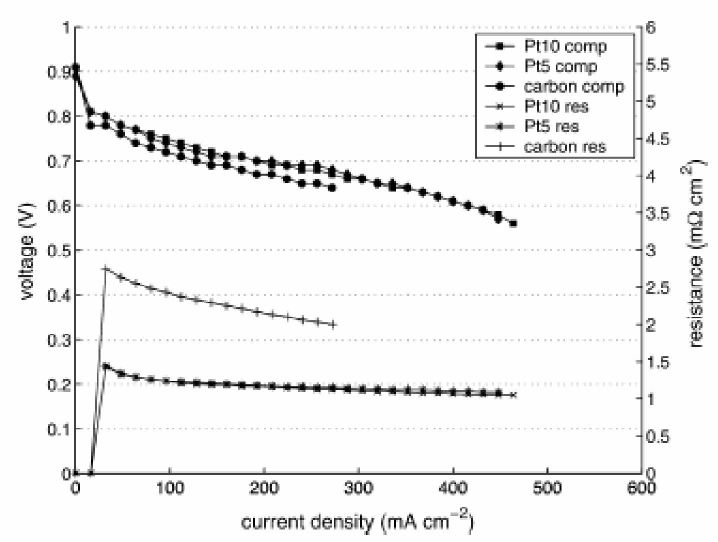

Figure 23: ***IR*-compensated polarization curves recorded when using coated titanium sinters as PTL on the cathode of the cell. "Pt10", "Pt5" and "carbon" indicate the coating material and thickness, 10 nm platinum, 5 nm platinum and 10 nm carbon, respectively. "Comp" and "res" refer to *IR*-compensated polarization curves and resistance curves, respectively.**

A certain difference in polarization behavior between experiments using uncoated and coated titanium sinters on the cathode side warrants further discussion. Evidence of flooding discernible in Figure 22 is not present in Figure 23. This would indicate that coatings on the titanium sinter improved water removal from the cathode, probably by altering the surface properties of the sinter towards lesser hydrophilicity. Hydrophobicity helps keep the electrode surface free of liquid water. To this end, conventional PTL materials are often treated with PTFE or similar fluorocarbons.

Performance of titanium sinter PTLs tested here was inferior to conventional carbon paper PTLs in a forced convection PEMFC due to high contact resistance and mass transport problems. However, in special applications, such as free-breathing fuel cells with large cathode area, where current density is low and high rigidity of the PTL is desirable titanium sinters may be feasible.

Coating PTLs with platinum conflicts with the current trend of lowering the noble metal content of fuel cell electrodes, but the amount of platinum required for 10 nm loading (0.2 mg m^{-2}) is still several orders of magnitude lower than that of low platinum load electrodes (~1 g m^{-2}). Material cost for 10 nm platinum[q] coating is ca. \$8.5 m^{-2}, while the price of conventional porous transport layers and titanium sinters is ca. \$1000 m^{-2} [85]. However, the vacuum deposition method used for platinum coatings is very expensive. With a cost effective coating process, additional cost of platinum coating may be tolerable at least for certain applications.

---

[q] World spot price for platinum: $39.26 per gram (2006-04-25)

8. Porous transport layer characterization

8.1. Background

Despite their multiple functions in a PEM fuel cell and the fact that their properties are crucial for high performance, porous transport layer properties remained a poorly characterized and understood subject until recent years. Especially in the case of uncatalyzed PTLs, the number of studies in open literature was limited at the time of writing publication IV [31 86 87 88 89 90 91 92 93 94 95 96 97 98 99]. Many of these papers discuss the effect of certain properties of PTLs, e.g. PTFE content, on fuel cell performance under various operating conditions. However, they do not provide a solid link between the physical properties of a PTL material and performance in a fuel cell. There are also a number of studies on catalyzed PTLs [51 100 101 102 103 104 105 106 107 108], but in that case establishing a connection between PTL properties and performance is even more challenging, since the effect of the PTL substrate is difficult to differentiate from the effect of the electrode structure. In the last two years, the general interest in PTL properties and performance and consequently the number of papers published on the subject has increased.

Traditionally PTL performance testing has been carried out by recording polarization curves and electrochemical impedance spectra. While applicable, this approach is very time consuming, since especially electrochemical impedance spectroscopy (EIS) requires equilibrium conditions in order to produce reliable results. Furthermore, testing performance at several compression pressures by polarization curve scans multiplies the testing time by the number of pressure points. In publication V, a faster method for PTL performance characterization is described and the dependence of performance on various physical properties of PTL materials is studied.

8.2. Experimental setup and methods

In situ PTL testing was carried out using cell hardware built at the KTH in Stockholm, Sweden. In the cell, clamping pressure on the current collectors is independent of sealing pressure and is exerted by a pneumatic piston. Active area of the cell is 7.1 cm^2 and current collectors are cylindrical, with spiral flow channels. The cell and a schematic cross section of the device are presented in Figure 24. The cell is described in detail in [109] and [110].

Cell temperature during *in situ* testing was 60°C. Reactants were fed into the cell at excessive rates in order to keep the oxygen concentration uniform throughout the active area. Stoichiometric factor λ was 5.5 for hydrogen and 4.3 for air. For oxygen, same flow rate was used as for air in order to maintain similar water removal conditions. Reactant gases were humidified, hydrogen at 60°C, and air and oxygen at 48 or 60°C in order to investigate PTL performance under both one and two phase conditions. All testing was carried out at atmospheric pressure.

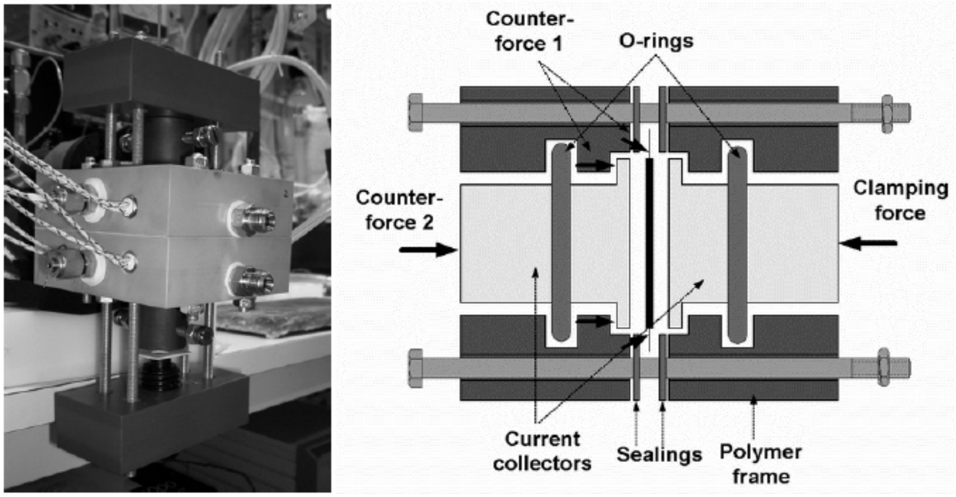

Figure 24: On the left, a photograph of the cell used for PTL testing. On the right, a schematic cross section of the cell. (Figure: Jari Ihonen)

Two carbon cloth and four carbon paper PTL materials were subjected to an array of *in situ* and *ex situ* tests. The goal of *in situ* testing was to investigate the effect of clamping pressure on cell performance and find the optimal clamping pressure for both one and two phase conditions. The experiments consisted of variable clamping pressure and cathode dew point experiments in galvanostatic mode and polarization curve measurements. Polarization curve measurements were carried out at low and high humidity regions at various clamping pressures using both oxygen and air as the cathode reactant. Variable cathode dew point tests were run in galvanostatic mode, unlike Mathias *et al.* [33], to maintain constant water removal conditions, which depend on heat production and flow rate and stoichiometry. Additionally, electrochemical impedance spectroscopy was used to investigate cell operation.

Physical properties of PTL materials, e.g. electrical and thermal conductivity, porosity and pore size distribution, gas permeability, and surface wetting properties were investigated by *ex situ*. The main goal was to investigate the dependence of PTL performance on the physical properties, and secondly, provide values of physical properties for modeling purposes. The procedures used for *ex situ* measurements are detailed in publication V.

8.3. Results and discussion

8.3.1. In situ testing

The traditional approach, recording polarization curves, was applied to one of the PTL materials, GORE™ CARBEL™ CL. Polarization curves recorded at various clamping pressures and two different cathode humidifier set points are illustrated in Figure 25. The curves are *IR*-compensated to better highlight the effect of clamping pressure on mass transport, caused by the loss of porosity. The effect of clamping pressure on cell resistance is discussed later.

For the set of operating conditions and hardware used, the highest *IR*-compensated voltage at high current densities under both low and high humidity conditions was obtained when clamping pressure was 9.7 bar. Therefore, the optimal clamping pressure lies between 4.3 and 18.1 bar. The increase in mass transfer overpotential is clearly distinguished when the difference in cell voltage between polarization curves measured with oxygen and air ($\Delta U_{\mathrm{O2\text{-}air}}$) are plotted. At low current densities, $j < 400$

mA cm^{-2}, $\Delta U_{\text{O2-air}}$ behaves uniformly at all clamping pressures, but displays variations at higher current densities. This is an indication that the mass transfer overpotential is significant at current densities higher than 400 mA cm^{-2}. Furthermore, the fact that the behavior of $\Delta U_{\text{O2-air}}$ is similar for both low and high cathode humidity indicates that the mass transport overpotential stems from the loss of porosity under the ridges of the current collectors rather than flooding of the electrode.

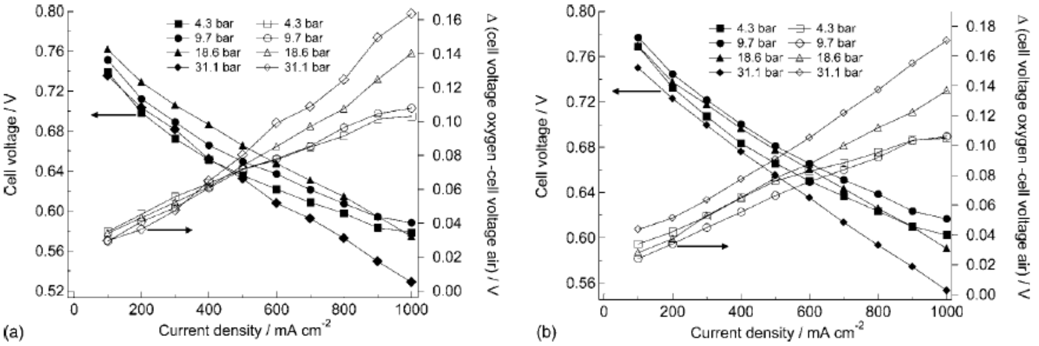

Figure 25: *IR*-compensated polarization curves and cell voltage difference between measurements using oxygen and air. PTL material: CARBEL™ CL. a) one phase conditions, cathode humidifier dew point 48 °C b) two phase conditions, cathode humidifier dew point 60 °C

The results derived from polarization curve measurements were corroborated by variable clamping pressure tests at constant current. The *IR*-corrected voltage reached the maximum at ca. 10 bar for both low and high cathode humidity. However, the optimal cell voltage was obtained at ca. 20-25 bar for high humidity conditions, and significant mass transport problems were detected only close to 30 bar. For low humidity, optimum clamping pressure was clearly higher, over 28 bar.

A possible explanation for this behavior is the improved thermal conduction with increasing clamping pressure. This allows more efficient heat removal from the MEA, which lowers the temperature difference between the MEA and current collectors. Since the absolute humidity is constant, decreased MEA temperature leads into increased relative humidity near the MEA, resulting in improved humidification and lower membrane resistance. On the other hand, also mass transport overpotential increases with clamping pressure, due to loss of porosity under the flow field ridges. This counteracts the beneficial effect of improved electrical and thermal contact, and at the optimal clamping pressure, these opposing effects are balanced. The exact point of balance depends on the materials and operating conditions, but in general the optimal clamping pressure is higher for low humidity conditions, because the decreased temperature on MEA surface is less likely to lead into flooding.

As a further example of information obtained by variable clamping pressure testing, cell voltage and resistance measured using ®SIGRACET GDL 10 BC and 30 BB carbon paper PTLs at constant current density are presented in Figure 26a and Nyqvist plots for 30-BB at various clamping pressure levels from the same measurement in Figure 26b. 30-BB is recommended for low to intermediate humidity operation, while more rigid 10-BC is targeted for intermediate to high humidity region. As expected, 10-BC outperformed 30-BB under two phase conditions. Best performance with 30-BB was reached already at a clamping pressure of 12 bar, above which performance degraded due to loss of porosity and flooding. Decrease in cell resistance and increase in mass transport overpotential are clearly visible also in the Nyqvist plots, see Figure

26b. For 10-BC, performance improved monotonously with increasing clamping pressure, and optimum point, which is above 25 bar, was not reached in the test.

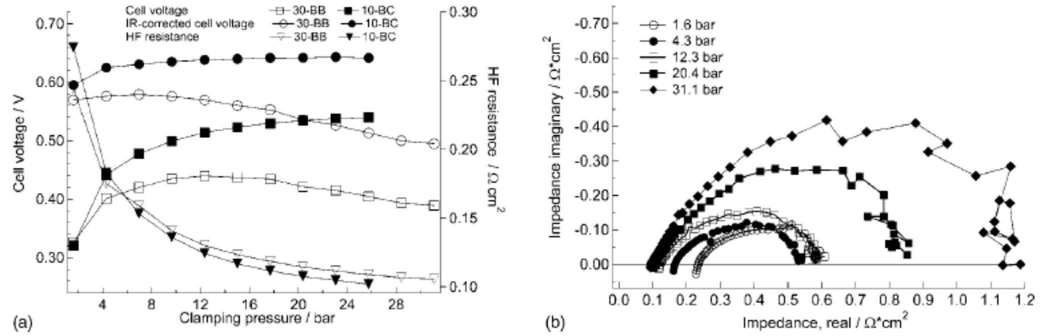

Figure 26: a) Cell voltage and resistance as a function of clamping pressure at 1 A cm^{-2} under two phase conditions for ®SIGRACET GDL 10 BC and 30 BB materials. b) Nyqvist plots for ®SIGRACET GDL 30 BB at various pressures.

Variable dew point method was found to be the fastest way to study PTL performance under one and two phase conditions. As an example, Figure 27a illustrates cell voltage and resistance at constant current of 1 A cm^{-2} at various cathode dew point temperatures when using ®SIGRACET GDL 30 BB PTL, and Figure 27b shows the cell voltages when operating on air and oxygen as a function of cathode dew point with ®SIGRACET GDL 10 BC.

Under one-phase conditions 30 BB performs well, but cell voltage begins to drop steeply when approaching two phase conditions, i.e. ca. 55°C, because liquid water accumulates in the PTL and obstructs oxygen diffusion. Improved humidification is seen to decrease ohmic losses but that is not enough to counteract the detrimental effect of flooding.

For 10-BC, the dew point sweep was performed also when operating on oxygen. Comparing the voltages recorded at various cathode dew points when operating on air and oxygen reveals the effect of improved membrane humidification and the fact that flooding occurs mainly in the PTL, not in the electrode. Cell voltage on air increases due to improved humidification when cathode dew point temperature approaches 50°C and drops slowly after that because of flooding. On neat oxygen, voltage rises, again due to improved membrane humidification, until cathode dew point reaches ca. 60°C and stays on that level at higher dew points. If the electrode was covered by liquid water, oxygen diffusion to the electrode would be obstructed which would appear as voltage drop also in the *IR*-compensated voltage curve measured on neat oxygen. Therefore, it can be concluded that flooding occurs in the PTL.

Measuring the exhaust gas temperature confirmed the temperature difference between the PTL and the current collector. Temperature difference between the exhaust gas and current collector for both anode and cathode side, and cell resistance are presented as a function of clamping pressure in Figure 28. The existence of the temperature difference is an indication that the PTL surface is at higher temperature than the current collector, and the fact that temperature difference decreases with increasing clamping pressure is a further confirmation on the explanation provided when discussing the results in Figure 26.

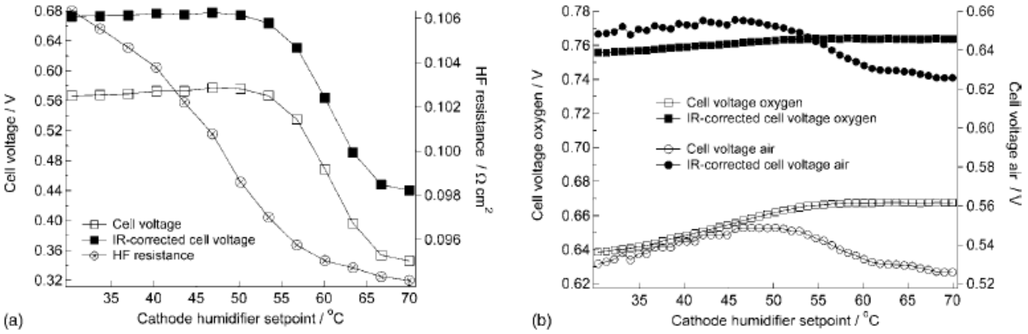

Figure 27: a) Cell voltage and resistance as a function of cathode humidifier dew point measured using ®SIGRACET GDL 30 BB and air. Clamping pressure 31.3 bar. b) Cell voltage as a function of cathode humidifier dew point, measured using ®SIGRACET GDL 10 BC and oxygen and air. Clamping pressure 28.4 bar.

Gases are flowing in channels in which one wall, the PTL, is at higher temperature than the other three. Therefore, depending on heat transfer properties, the temperature difference between the PTL and the current collector should be two to three times higher than that between the exhaust gas and current collector. Thus, the temperature of the PTL under the flow channel can be expected to be at least 3 to 6°C higher than the temperature of the current collector. If heat flux from the PTL to the current collector is assumed to be 0.7 W cm^{-2}, the heat transfer coefficient of the PTL-current collector junction is in the order of 1.7 to 3.3 kW m^{-2} K^{-1}. However, the PTL temperature is based on a best-guess estimate, and thus heat transfer coefficient is only suggestive.

Exhaust gas temperature measurements can also be used to detect the onset of PTL flooding. Reaction product water accumulates in the cathode air stream, and therefore flooding starts near the outlet location. Flooding decreases local current density and heat production, thus decreasing PTL temperature, which can be observed as a decreasing temperature difference between the exhaust gas and current collector. An example is presented in Figure 29. Between 45 and 57°C, the temperature difference between the exhaust gas and current collector drops drastically as the end of the flow channel begins to flood. Above 57°C the temperature difference is seen to increase again as the current density distribution evens out, due to flooding reaching the whole area of the cell.

While polarization curve scans are applicable to PTL performance characterization, they are very time consuming, especially if electrochemical impedance spectroscopy is applied. EIS requires steady equilibrium conditions, which are reached only after 10 to 20 minutes. Furthermore, current density sweeps change the water and heat production and thus the water management conditions, and may change the kinetics of electrode reactions. Many of these drawbacks can be avoided by variable clamping pressure and humidifier dew point testing, which provide a faster method to characterize PTL performance in fuel cells.

Measurement of exhaust gas temperatures is a challenging task due to low heat capacity of gases. Temperature probes must be installed in the gas outlet channels without any contact to channel walls or other solid material, otherwise thermal conduction will distort the measurement results.

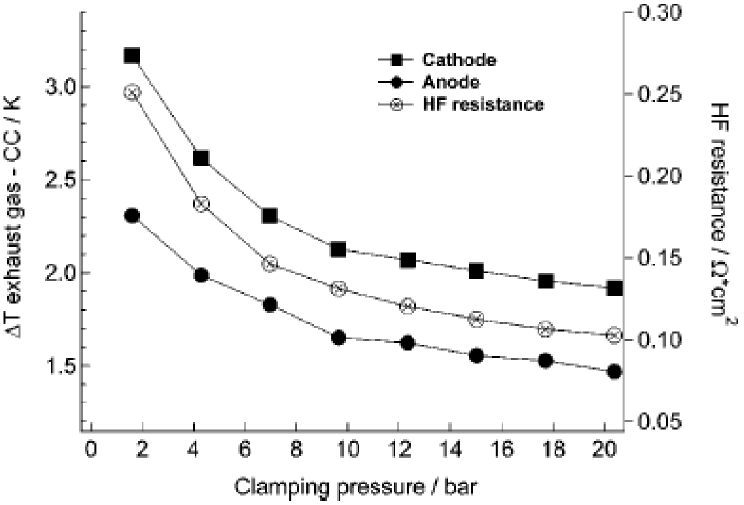

Figure 28: Temperature difference between the exhaust gas and current collector and cell resistance as a function of clamping pressure at 1 A cm^{-2} and 60 °C cathode humidifier dew point. PTL material: GORE™ CARBEL™ CL

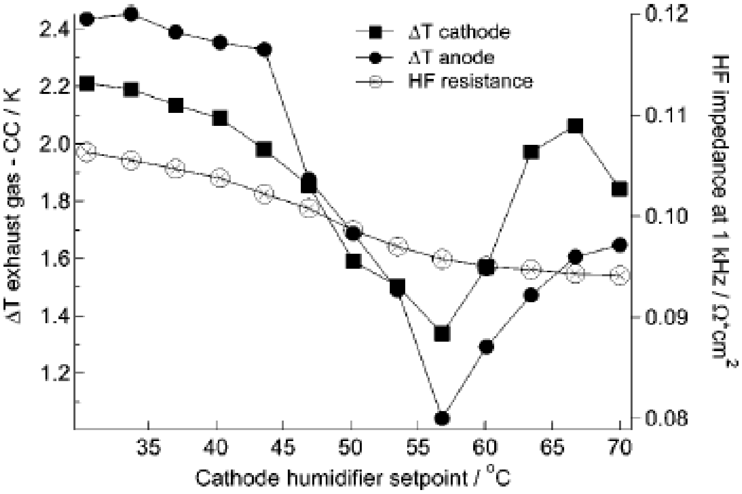

Figure 29: Temperature difference between the exhaust gas and current collector and cell resistance as a function of clamping pressure at 1 A cm^{-2} and 60 °C cathode humidifier dew point. PTL material: ®SIGRACET GDL 30 BB

8.3.2. *Ex situ* testing

Pore size distributions measured from uncompressed PTL samples by mercury intrusion porosimetry are presented in Figure 30. While there are notable differences in pore size distributions, they could not be linked with PTL performance in a fuel cell under two phase conditions. Most PTL materials had a microporous layer (MPL), which has very different structure than PTL substrate material, on one or both sides. However, samples without the MPL could not be obtained for most materials, and therefore achieved porosity values are a combination of PTL substrate and MPL porosities. For further research, pore size distributions should be measured from both plain and MPL containing samples in order to differentiate the effect of the MPL.

Interestingly, all measured porosities were lower than those given by PTL manufacturers. However, this may be a reflection of different measurement procedures.

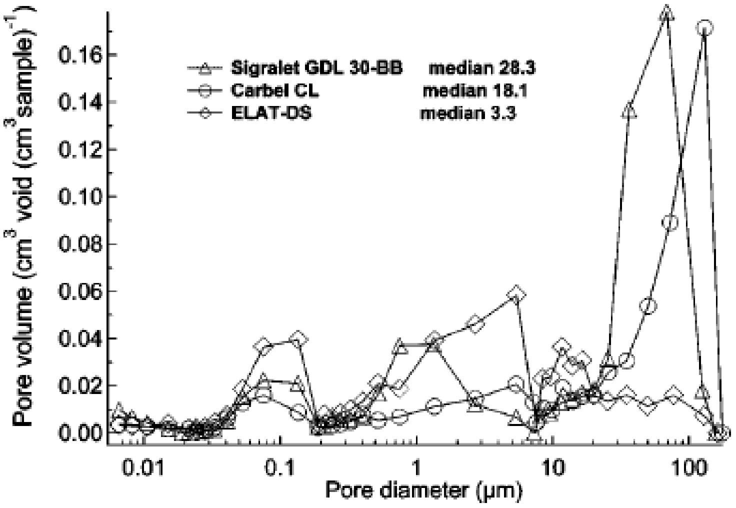

Figure 30: Pore size distributions in uncompressed PTL samples measured by mercury intrusion porosimetry.

Measured in-plane permeability at 1 bar compression and through-plane permeability varied in the range from $3.3 \cdot 10^{-11}$ to $5.2 \cdot 10^{-13}$ m^2 and $1.8 \cdot 10^{-11}$ to $9.6 \cdot 10^{-14}$ m^2, respectively. While an exclusive and unambiguous dependence of performance on PTL permeability was not found, due to the number and interdependent nature of the phenomena, it can be concluded from the results that an in-plane permeability in the range of 10^{-12} m^2 is sufficient for fuel cell operation.

Wetting properties of PTL materials were investigated by measuring the contact angle with deionized water. Results ranged from 145 to 154°, and the two materials that performed best under two phase conditions scored the lowest and highest contact angles. Therefore it can be concluded that the wetting properties of PTL surfaces are not deciding factors for performance in a fuel cell.

Porosity, pore size distribution and wetting properties all affect the water management properties of PTLs. The phenomena controlling these properties are interdependent and it is difficult to deduce PTL performance in a fuel cell based on *ex situ* measurement results. Furthermore, water management properties depend also on qualities that are very difficult to measure, e.g. the distribution of PTFE and the wetting properties of micro and macropores inside the PTL substrate.

Measured thermal resistance and electrical contact resistance for ®SIGRACET GDL 10 BC and CARBEL™ CL as a function of clamping pressure are presented in Figure 31. Bulk conductivities usually fall in the range of 50-200 S cm^{-1} [33], which would correspond to less than 1 mΩ cm^2 in resistance per unit area and is small compared to electrical contact resistance. Similar values were obtained for electrical bulk resistance in other tests. Obtained values of electrical contact resistance for one PTL/current collector interface, 5-15 mΩ cm^2, agree well with results published by Mishra and coworkers [99]. However, the work here and by Mishra *et al.* ignore the effect of compression on bulk conductivity, increasing uncertainty of the results.

Measured heat transfer coefficient from the PTL to the current collector range from 0.7 to 1.4 kW m^2 K^{-1}, corresponding to thermal resistance of 7 to 15 K cm^2 W^{-1}, in the clamping pressure range of 3 to 10 bar. These values contain contributions from both bulk and two interfaces between the PTL and current collectors. If interface resistances are ignored, this corresponds to thermal conductivity of 0.2-0-4 W m^{-1} K^{-1}, close to the value reported by Vie [111]. However, thermal conductivity that low is unrealistic for a material that consists of graphitized carbon fibers. Thermal and electrical conductivities of porous materials are interrelated and the fact that the electrical bulk conductivity of PTLs is about 5-10% of the conductivity of solid graphite, it can be assumed that the same applies also for thermal conductivity. That gives a thermal conductivity of ca. 5-10 W m^{-1} K^{-1}, which corresponds to less than 1 K cm^2 W^{-1} for normal PTLs. Similar to electrical resistance, interfaces are the dominating source of thermal resistance, with thermal resistance of ca. 3-7 K cm^2 W^{-1}. This value agrees well with the thermal resistance value calculated from exhaust gas temperature data, but there is large uncertainty due to the method used here. Measurement of contact resistance is discussed further in chapter 9.

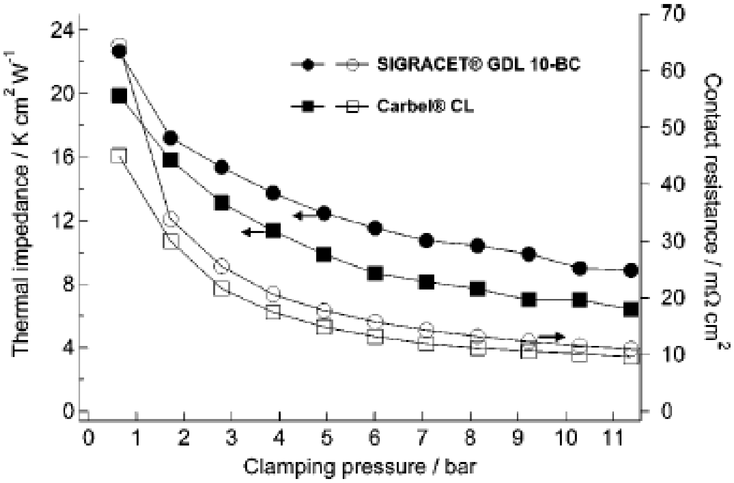

Figure 31: Thermal resistance and electrical contact resistance as a function of clamping pressure for ®SIGRACET GDL 10 BC and CARBEL™ CL. Resistance values include the bulk resistance and two contact resistances (PTL-current collector).

At a realistic heat production rate of 0.7 W cm^{-2} and a channel/ridge ratio of 1:1 this would correspond to a 2-5 K drop across the electrode-PTL interface, if all heat is assumed to leave the electrode by conduction evenly through both sides of the cell. This is significant for water removal and MEA humidification – A temperature change from 60 to 65°C increases the pressure of saturated water vapor by 25%.

9. Inhomogeneous compression of PEMFC porous transport layers

9.1. Background

When a fuel cell with traditional flow channels on bipolar plates is assembled, flow channel ridges exert a pressure onto the porous transport layers, but areas under the flow channels remain uncompressed. While PTL under the ridge is compressed to gasket thickness, PTL under the channel retains most of its original thickness and intrudes into the flow channels, as illustrated in Figure 32.

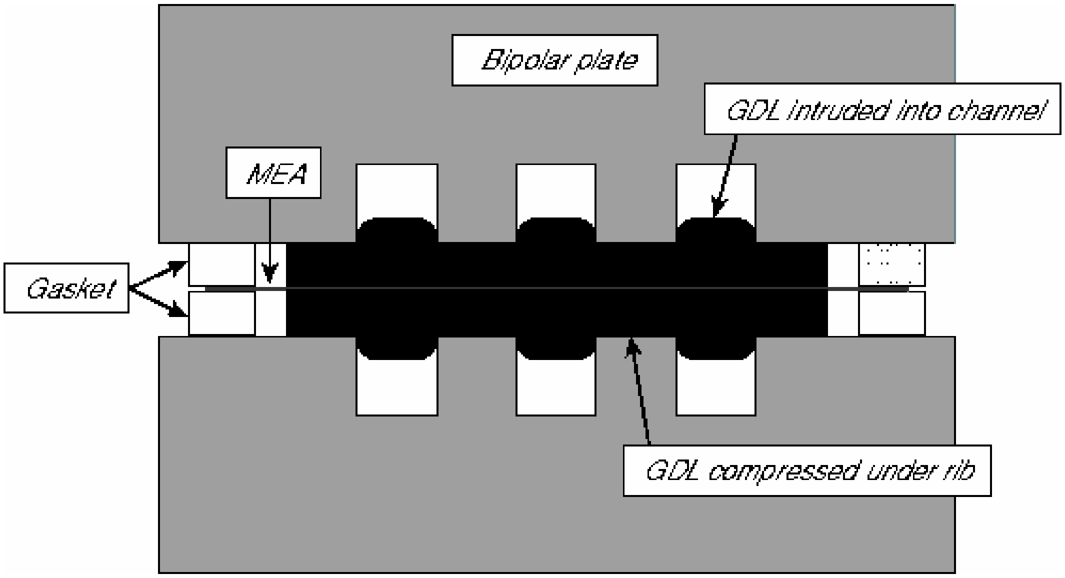

Figure 32: PTL deformation under compression. PTL under the ridges is compressed to gasket thickness, while the parts under the flow channels remain uncompressed and intrude into the channels.

Inhomogeneous compression of the porous transport layers has several effects on fuel cell operation. PTL intrusion into flow channels decreases the effective cross section, increasing pressure loss in the channels. Furthermore, PTL compression under the ridges reduces porosity, which decreases permeability and thus hinders oxygen access to the electrode under the ridge and water removal from under the ridges.

Contact resistance between the PTL and electrode under the channel is higher than under the ridge, due to the pliable nature of PTL materials and lack of compression. Lower contact pressure under the channels has been observed experimentally [e.g. 110]. As a result, there are lateral currents in the electrode as the current pursues a path of least resistance and crosses over to the PTL where contact resistance is lower, i.e. under the ridge. Uneven current density distribution may create unfavorable hot spots due to ohmic heating where local current density is high. Current density distribution is further distorted by the changes of PTL bulk conductivity induced by compression. Compression increases the number of contact points between the carbon fibers in the PTL, thus increasing conductivity. Similarly to electrical current, also heat flux is affected by changes in thermal contact resistance.

Despite their various functions and importance for fuel cell operation, porous transport layers have received little research attention until recent years. There are few previous studies on PTL properties under compression. There are a few studies on

PTL gas permeability under compression [87 94 112 113 114 115 116], and it has also been considered in some models [117 118]. Variations in bulk electrical conductivity of the PTL under compression have been modeled by Meng and Yang [117] and by Pharoah *et al.* [121], but experimental studies are scarce. Typically electrical conductivity has been roughly estimated from values based on uncompressed samples [99 109]. Thermal bulk conductivity of PTLs has been experimentally determined in publication IV and more recently, by Khandelwal and Mensch [119]. They also determined the thermal contact resistance between the PTL and metal plate. However, the effect of compression on thermal bulk conductivity was not considered in publication IV or by Khandelwal and Mench [119].

The importance of electrical contact resistance between the PTL and other components has been discussed by many authors [33 42 74 80 99 109 110 120 121], but few experimental results have been published [99 110 120]. Furthermore, all authors have ignored bulk conductivity of the PTL, which is affected by compression.

Fuel cell modelers have so far seldom taken these effects into account. Sun *et al.* [122] and Zhou *et al.* [123] considered the effect of inhomogeneous compression of the porous transport layers, but Sun *et al.* ignored contact resistance and Zhou *et al.* the effect of compression on bulk conductivity of PTLs. Typically, PTL thickness, permeability and contact resistance between the PTL and electrode, if considered at all, are assumed uniform all over the cell area.

Goal of this work was to experimentally evaluate porous transport layer properties and contact resistance between cell components as a function of compression. Obtaining accurate values for these properties would enable improving existing computer models and thereby optimizing fuel cell structure for higher performance. Measured properties were PTL intrusion into the flow channel, in-plane gas permeability, in- and through-plane electrical conductivities, and contact resistance between the current collector and PTL, as well as PTL and electrode. All properties were measured as a function of PTL compressed thickness instead of compression pressure, since unlike compression pressure, compressed thickness can be controlled without special equipment. Values were successfully obtained for all properties except for contact resistance between the electrode and PTL.

9.2. Experimental methods and setup

9.2.1. PTL material

Porous transport layer material used in all experiments was SGL ®SIGRACET GDL 10 BA (by SGL Carbon AG). The material is a carbon paper, wet proofed with 5%-wt PTFE solution. The material has no microporous layer and the porosity is 88% [124].

9.2.2. PTL intrusion into flow channel

For measuring the intrusion into flow channel, a PTL sample was placed between two rigid metal plates and compressed to desired thickness set by clearance gages. One of the plates had a groove in the middle, which functioned as the flow channel. Bottom of the groove had an opening in the middle, through which a probe attached to a dial gage came into contact with the PTL surface. Prior to assembly, dial gage was zeroed to plate surface. Thus, PTL intrusion into the groove could be measured. The experiment was repeated with several groove widths, ranging from 0.6 to 2 mm.

9.2.3. Gas permeability under compression

For gas permeability measurement, a circular PTL sample was centered between two rigid metal plates and compressed to desired thickness set by clearance gages. The top plate had a gas inlet in the middle. The flow of dry air, which entered the PTL sample in the center and then permeated radially through the sample until the edge, was controlled by a Brooks 5850S mass flow controller. Pressure difference between the inlet and outlet was measured with a tube manometer for several air flow rates and sample thicknesses. Gas permeability of the sample for each thickness was calculated by Darcy’s equation, using measured pressure differences and set flow rates.

9.2.4. PTL through-plane electrical conductivity

Through-plane conductivity of the PTL material was determined by measuring the resistance of a stack of PTL samples (up to 6) compressed between two graphite current collector plates, see Figure 33, by four point probe method. The thickness of the PTL sample stack was controlled by clearance gages.

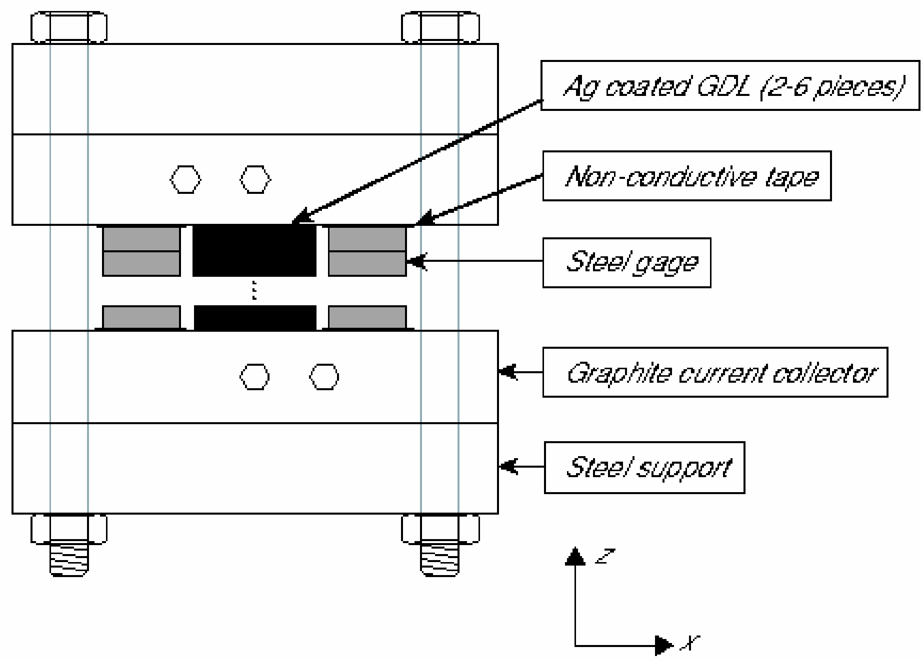

Figure 33: Resistance measurement setup.

To eliminate contact resistance between the PTL samples, all PTL surfaces at PTL-PTL interfaces were vacuum evaporation coated with a 150 nm layer of silver, which has been shown to reduce contact resistance significantly [125 126], but not affect the bulk conductivity [127]. If the PTL-PTL contact resistance is assumed negligible, the measured resistance can be expressed as

$$R_{meas} = 2 \cdot R_{gr} + n \cdot R_{PTL,bulk} + 2 \cdot R_c \tag{1}$$

where R_{meas}, R_{rg}, $R_{PTL,bulk}$, R_c, and n are the measured resistance, bulk resistance of the graphite, bulk resistance of the PTL, the contact resistance of the PTL-graphite interface, and number of PTL samples in the stack. When R_{meas} is plotted as a function of n, the slope of the graph gives the bulk resistance of PTL material, $R_{PTL,bulk}$. R_{gr} was measured with the four point probe method, and R_c was obtained with a method presented in chapter 9.2.6.

9.2.5. PTL in-plane electrical conductivity

The apparatus used for in-plane electrical conductivity measurement is presented in Figure 34. Both ends of a rectangular PTL sample were clamped under graphite current collectors. Thickness of the PTL under the current collectors was controlled by clearance gages, and the distance between the current collectors could be adjusted. The part of the PTL not under current collectors was compressed to desired thickness by a plastic plate. Resistance of the system was measured by four point probe method for each sample thickness at several distances between the current collectors. Since contact resistances between the PTL sample and current collectors remained constant, the difference of the two resistance values gave the contribution from the bulk PTL material. Bulk conductivity was calculated from the result using equation 2.

$$\sigma_{x,h} = \frac{1}{R_2 - R_1} \frac{x_2 - x_1}{h \cdot w} \tag{2}$$

where $\sigma_{x,h}$ is the bulk conductivity of the PTL sample at thickness h, x_2 and x_1 are the distances between current collectors, R_2 and R_1 are measured resistance values, and w is the sample width. In order to increase accuracy, all measurements were conducted at several current collector separations and the results averaged for each PTL thickness.

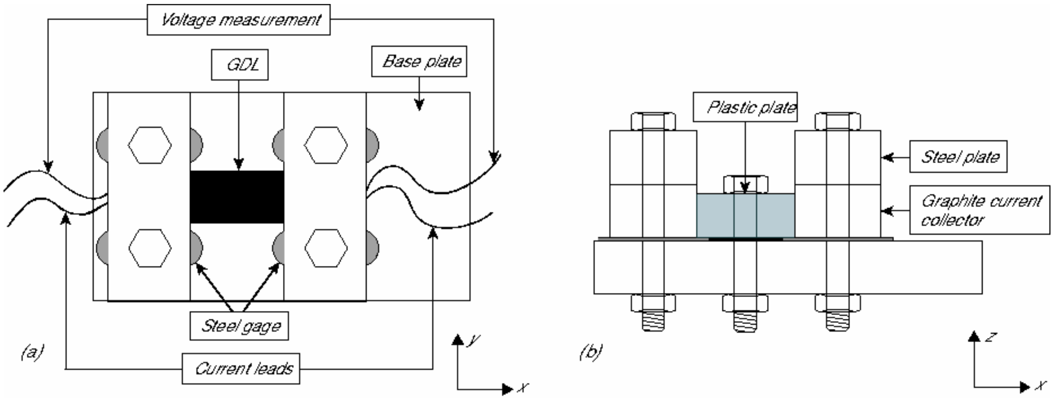

Figure 34: In-plane conductivity measurement set-up. a) top view b) cross section

9.2.6. Contact resistance between PTL and current collector, and PTL and electrode

Instead of using equation 1 and measured graphite conductivity to calculate contact resistance between the PTL and current collector, the apparatus in Figure 33 was implemented as a 3D model in COMSOL Multiphysics 3.2, a commercial PDE solver software, and contact resistance was determined by simulation. Conductivity of the graphite current collectors was only an order of magnitude higher than that of PTLs, and the thickness was an order of magnitude higher. Therefore, the bulk resistance of graphite current collectors was comparable to PTL resistance, and thus current profile through the current collector could not be assumed constant. Measured potential differences were used as boundary conditions at current lead connectors and determined bulk conductivity of PTL material and graphite were used, and the potential profile was solved in the model. The potential profile and measured current were used to calculate the contact resistance between the PTL and current collector. Beginning from an initial guess, the contact resistance was varied until the simulated current was equal to the measured one.

Since the ionomer membrane between the electrodes in an MEA is an electric insulator, the device in Figure 33 could not be applied for determining contact resistance between the PTL and the electrode. Instead, the apparatus for in-plane conductivity, see Figure 34, was used. The measurement procedure was similar to that of PTL in-plane conductivity, but the PTL sample was replaced with a MEA sample of similar dimensions. Pieces of PTL of exactly the same size as the current collectors were placed under the current collectors, between the current collector and the MEA. Resistance of the system was again measured at various current collector separations and the measurement system was implemented in COMSOL Multiphysics 3.2. Since contact resistance between the current collectors and PTL was known from the previous experiment, the only unknown quantity, contact resistance between the PTL and electrode could be solved by simulation.

9.3. Results and discussion

Figure 35 gives the thickness of PTL under the channel at various channel widths as a function of gasket thickness i.e. steel gage thickness in the figure. Intrusion depth is the difference of PTL thickness under the channel and gasket thickness. Even at maximum compression, the PTL under the channel was compressed only 8% of the original thickness. When the PTL under the ridges was compressed to 250 μm, PTL thickness under the channel changed only by ca. 3%. Intrusion depth into the channel depends on the type and properties of the PTL material, but all pliable materials exhibit this behavior to some extent.

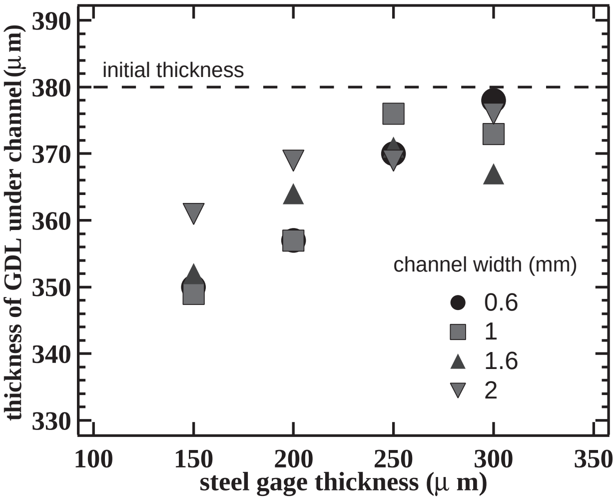

Figure 35: Thickness of PTL (SGL ®SIGRACET GDL 10 BA) under the flow channel as a function of the thickness of the compressed part of the PTL (gage thickness).

Large local differences in thickness lead into local variations in mass transport properties. Oxygen and water transport is hindered under the ridges due to loss of permeability caused by compression. Furthermore, low compression leads into low contact pressure between the PTL and the electrode under the channel, which increases electrical and thermal contact resistance. Additionally, PTL intrusion into the channel decreases channel cross section, affecting the velocity of the reactant flow and increasing pressure loss in the flow channels.

Measured in-plane gas permeability of ®SIGRACET GDL 10 BA PTL as a function of compression is presented in Figure 36. Permeability decreases by an order of magnitude when the PTL is compressed to 250 μm, 66% of the original thickness, but decreases slowly afterwards. These values agree well with results in the open literature, e.g. [33]. ®SIGRACET GDL 10 BA porosity given by the manufacturer is 88%, and at 66% thickness (250 µm), approximately 39% of the pore volume is lost, giving a porosity of ca. 82%.

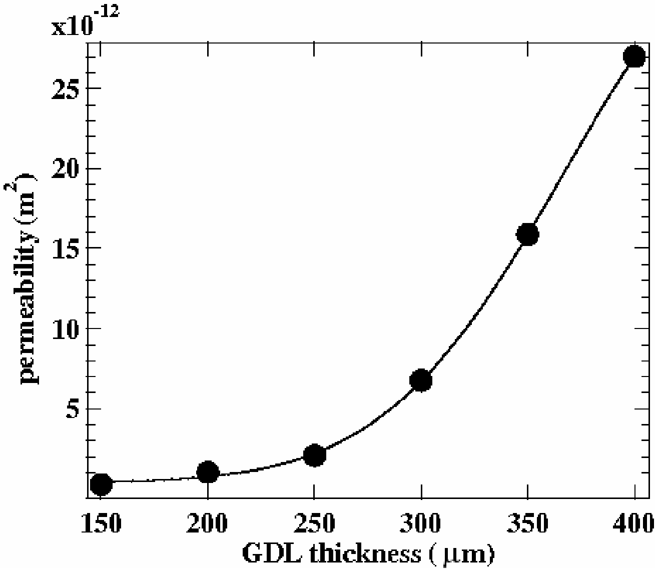

Figure 36: In-plane gas permeability of SGL ®SIGRACET GDL 10 BA as a function of thickness.

As shown above, PTL permeability under the channel can be an order of magnitude higher than that under the ridge, and reactant flow velocity and pressure loss increase due to PTL deformation. This has a notable effect on mass transport especially on the cathode side, and should be taken into account in computer models if more realistic description of operating conditions is desired.

Measured electrical conductivity of ®SIGRACET GDL 10 BA in in- and through-plane directions is given in Figure 37. In-plane conductivity was three to four times higher than through-plane conductivity, probably due to orientation of carbon fibers in the material. Most fibers are aligned in the in-plane direction and have relatively few contact points with fibers above and below at low compression. The number of contact points increases with compression, as well as the quality of existing contacts. Through-plane conductivity was very low at lowest compression for the same reason. The in-plane values were smaller than previously reported, from 5000 to 23000 S m^{-1} [33 73]. However, obtained through-plane conductivity in normal compression range (up to 66%) agreed with those previously reported, from 300 to 1400 S m^{-1} [33 80 124 128]. Some of the difference can probably be attributed to structural differences between PTL materials, but majority to overestimation of contact resistance, which leads into overestimation of bulk conductivity.

Area specific contact resistance values for the interface between the graphite current collector and the PTL are presented in Figure 38. The values were obtained by simulation using measured conductivity values and error limits were obtained by repeating the simulation and varying the values for measured quantities within their respective error limits. Contact resistance is strongly dependent on compression. As PTL is compressed from 92% to 66% of the original thickness, contact resistance decreases by an order of magnitude, due to increase in contact quality and actual contact area.

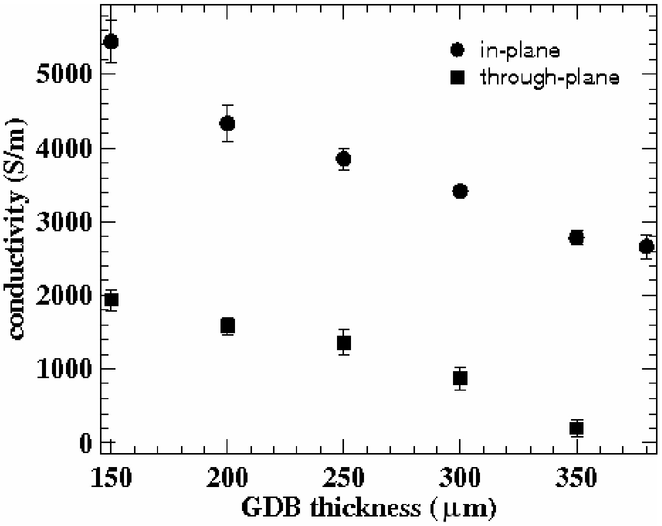

Figure 37: In- and through-plane electrical conductivity of SGL ®SIGRACET GDL 10 BA as a function of thickness.

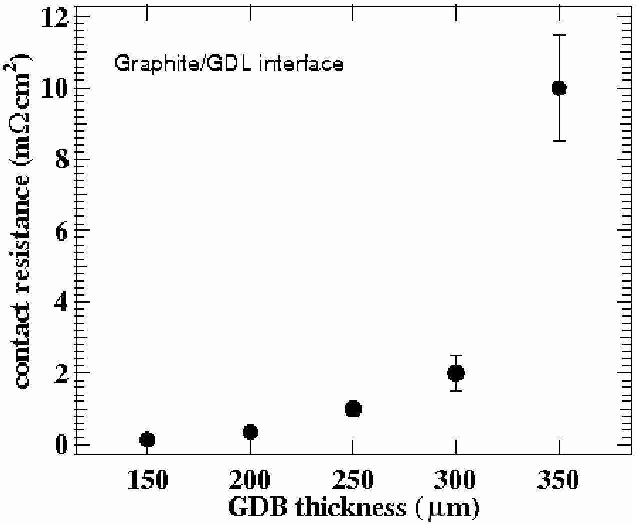

Figure 38: Area specific contact resistance between the current collector and SGL ®SIGRACET GDL 10 BA as a function of thickness.

Contact resistance between fuel cell components is discussed in many publications. Reported values for contact resistance between the current collector and PTL under moderate compression (0.5-2 MPa) fall in the range of 1 to 50 mΩ cm^2 [33 42 73 80 110 120 121]. Based on these results, the significance of contact resistance has been often overestimated. Large variation of results can probably be explained to some extent by differences in material properties, but more probably the cause is ignoring the contribution from the bulk of PTL and current collector.

Resistance contributions from bulk PTL material, PTL-current collector interface and bulk current collector are comparable. Using the values measured in publication V for through-plane conductivity of PTL at 250 μm, bulk resistance of the PTL is ca. 1.7 mΩ cm^2, and contact resistance between the PTL and current collector was ca. 1 mΩ cm^2. For the graphite used in the experiments, the bulk conductivity was ca. 70000 S m^{-1}. Therefore, the resistance of a 5 mm current collector is approximately 0.7 mΩ cm^2, which is close to both PTL bulk resistance and PTL-current collector contact resistance.

Measuring contact resistance between the electrode and the PTL was not successful, probably due to numerical problems in the simulation model. However, contact resistance at that interface is probably higher than that between the PTL and current collector due to the ionomer content in the electrode. Therefore, it can be expected that electrical and thermal contact between the electrode and PTL under the channel is poor compared to that under flow channel ridges. This produces lateral currents in the electrode, as current searches for the path of least resistance. Thus, realistic current density distribution is probably very different from those given by models that ignore the deformation of porous transport layer under compression and resulting variations in mass transport and electrical and thermal contact between cell components [129].

10. The effect of NaCl on PEMFC performance

10.1. Background

Laboratory PEM fuel cells typically use high purity reactants, which are not economically viable for real world applications. In the near future, affordable hydrogen will be manufactured from hydrocarbons or biomass by reforming, gasification or biological methods, while ambient air is used as the oxidant. In addition to a wide range of temperature and humidity conditions, fuel cells will be exposed to a number of impurities carried by the reactants. Before full commercialization of PEM fuel cells is possible, effects of different contaminants must be determined and ways to mitigate the harmful effects found.

Depending on the type and quantity of the contaminant species, time of exposure, and the side of the cell it is present in, i.e. anode or cathode, impurities may affect one or more components in the cell. Catalyst poisons, for example carbon monoxide, adsorb onto the catalyst surface and block reaction sites interfering with the electrode reactions, or alter reaction pathways by inhibiting or promoting certain reactions. Other impurities attack the ionomer, increasing resistance to the current carrying ion or induce ionomer degradation. In addition to affecting electrochemical operation, impurities may also cause corrosion or other surface changes in flow field plates, PTLs, pumps, fittings and other hardware.

On the anode side impurities are usually introduced into the cell with the fuel or originate from cell components. Hydrogen rich fuel streams made by reforming hydrocarbons such as natural gas, methanol, diesel or gasoline often contain at least small amounts of carbon monoxide and dioxide, sulfur compounds, hydrocarbon residues and other possibly harmful species. Fuel impurities often poison the catalyst, decreasing cell performance by altering reaction kinetics. For some impurities the effect is reversible and performance can be restored, but for other contaminants the degradation is permanent. The most studied fuel impurity is carbon monoxide, which is present in most reformed fuel streams [130 131 132 133 134 135 136 137 138 139]. Other investigated contaminants include carbon dioxide [139 140 141 142], hydrogen sulfide [143 144 145], ammonia [141 146 147 148], and hydrogen peroxide [149].

Contaminants in the atmosphere have both natural and anthropogenic sources, the most important being vehicle and industry exhausts from combustion of fossil fuels. In addition to exhaust gases, also fine particles and some naturally occurring species may have an adverse effect on fuel cell performance. Although air impurities are present in majority of fuel cell operating environments, their effect on fuel cell performance has received less attention than fuel impurities.

Previously, many groups have investigated the effect of some common contaminants found in vehicle exhausts: CO, CO_2, NO_2 and SO_2 [150 151 152 153]. Moore *et al.* included also some common chemical warfare agents in their study [154]. Mepsted carried out an extensive study on the effects of common exhaust gas components and other contaminants from internal combustion engines, and used several different MEA types in his experiments [155]. Okada has discussed theoretically the effect of cation presence in a PEM fuel cell [156 157].

There are several approaches for mitigating the harmful effects of fuel and oxidant impurities, scrubbing or using high purity hydrogen carriers and optimizing the reforming process being the most obvious. In mitigation of the effect of air impurities air filtering has been preferred over contaminant tolerant catalysts. Mechanical and chemical filtering can be used to lower the contaminant content of air down to tolerable levels [152 155 158 159].

To a great extent, studies on fuel impurity mitigation have concentrated on increasing tolerance to carbon monoxide. Operation at higher temperature, between 120 and 150°C, would decrease CO adsorption onto the catalyst surface [27 133 160 161]. On the other hand, it would require ionomers that maintain proton conductivity at higher temperature and low humidity, which are developed actively, see for example [162 163]. CO tolerance can also be improved by alloying the platinum catalyst with other materials, which promote oxidation of adsorbed CO. Currently, the most common catalyst alloys for CO-tolerant anodes are Pt/Ru and Pt/Ru-based ternary alloys [164 165 166 167 168 169]. CO oxidation can also be promoted by air bleed, i.e. mixing some oxygen into the fuel stream [23 168 170 171 172]. This involves some losses in fuel conversion to electricity due to direct chemical reaction between H_2 and O_2, but that is only of the order of a few percent [23] and performance benefits usually outweigh the losses. Similar addition of O_2 into the fuel stream can be achieved by injecting oxygen evolving compounds, e.g. hydrogen peroxide, into the fuel humidification system [173 174]. The beneficial effect of an air bleed can be enhanced by adding a CO selective catalyst layer between the flow channel and the electrode [24 25 175 176].

Publication VI concentrates on the effect of sodium chloride in the cathode side on PEMFC performance. NaCl from sea water is present in the atmosphere as aerosol on coastal areas, and is used as deicer on roads, which makes it a very relevant air impurity considering fuel cell powered vehicles. Harmful effects of metal anions on Nafion® conductivity are well documented [156 157 177 178 179 180 181 182 183] and chloride ions are a known catalyst poison, see e.g. [184 185], but studies of the effect of NaCl on PEMFC performance are scarce in the open literature.

10.2. Experimental methods and setup

The effect of NaCl on fuel cell operation was studied by injecting NaCl solution into cathode air stream of an operating PEM fuel cell and observing cell performance by several methods. These methods included polarization and high frequency resistance (HFR, 8 kHz) measurements at intervals to monitor performance change in time, and cyclic voltammetry in order to detect signs of catalyst poisoning. Furthermore, the effect of NaCl on Pt/C electrode was studied for reference in *ex situ* test. A single Pt/C electrode was prepared on glassy carbon and immersed in a H_2SO_4 solution, and cyclic voltammograms were recorded. Subsequently, NaCl was added into the solution and another set of voltammograms was recorded.

Fuel cell experiments were conducted using a 25 cm^2 cell with double sided E-TEK ELAT® porous transport layer on the anode side, E-TEK ELAT® v2.22 on the cathode and a Nafion® 112 membrane with thin film electrodes prepared following the Los Alamos National Laboratory standard procedure [186]. Platinum loading was ca. 0.2 mg cm^{-2} for both electrodes.

Cell temperature was 80°C and anode and cathode reactant humidification temperatures were 105°C and 85°C, respectively. Reactant flow rates were constant, 500 cm^3 min^{-1} (NTP) for dry hydrogen and 2100 cm^3 min^{-1} (NTP) for dry air at a total pressure of 2.9 bar(a). These flow rates correspond to stoichiometric factors of 2.9 and

5.1 for hydrogen and air, respectively, at a current density of 1 A cm^{-2}. The chosen operating conditions are similar to those used in automotive applications.

1 M NaCl solution was prepared using ACS reagent grade NaCl and deionized water. The solution was injected into cathode side air stream at 1 cm^3 min^{-1} from a pressurized reservoir and flow rate was controlled by a needle valve downstream from the reservoir. The flow rate was chosen so that it did not initially cause flooding in the cell.

The cell was operated at a constant voltage of 0.6 V during the NaCl injection test and average current density was recorded. After stopping NaCl injection, the cell was operated on neat air to study recovery from NaCl-induced performance loss. During the experiment, polarization and resistance curves were recorded at intervals. Cyclic voltammograms were recorded before the NaCl injection and after the recovery period.

10.3. Results and discussion

Current density vs. time curve recorded at constant voltage during the NaCl injection test is presented in Figure 39. NaCl injection was started at t = 0 h and continued until t = 99.2 h. Polarization and resistance curves, which are presented in Figure 40, were recorded at times indicated in Figure 39.

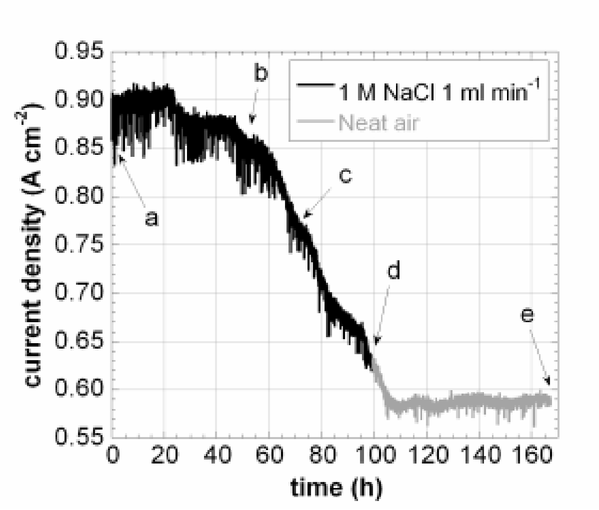

Figure 39: Current vs. time curve recorded at constant voltage (0.6 V) while injecting 1.0 M NaCl into the cathode air stream at 1 cm^3 min-1, and recovery on neat air. Polarization curves were recorded at a) 1.1h b) 53.4h c) 71.6h d) 99.2h e) 167.3h

Onset of performance degradation is delayed ca. 24 h despite the fact that the injected NaCl solution contains enough Na$^+$ to replace every proton in the membrane in every 15 seconds. The delay leads to the conclusion that sodium ions are transported to the MEA by diffusion in liquid, since diffusion in solid phase would be much slower and convective transport faster. Diffusion through graphite parts in the PTLs can not be ruled out as a secondary transport mechanism, since NaCl was seen to diffuse through graphite flow field plates, making them a long term NaCl source. After the initial onset of performance degradation, the rate of current density decay was ca. 4 mA cm^{-2} h^{-1} and was nearly linear after the first 30 hours. The plateau from 35 to 45 h was caused by NaCl pump malfunction.

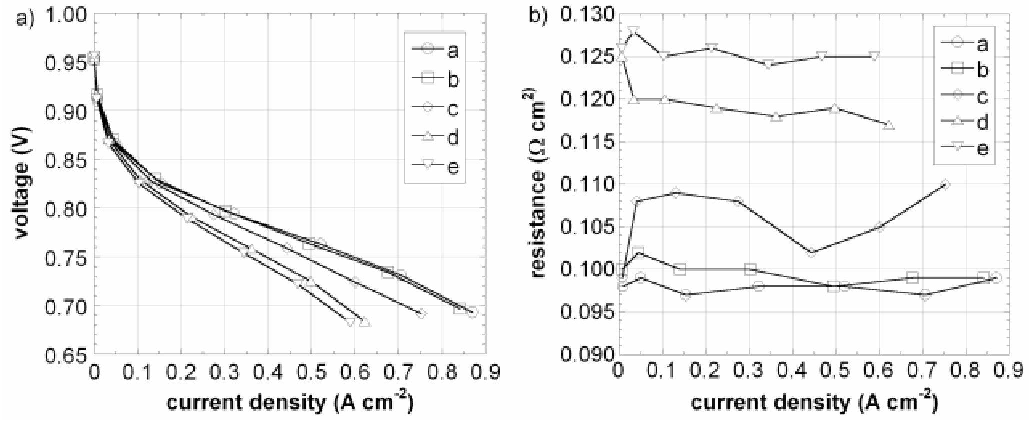

Figure 40: *IR*-compensated polarization and high frequency resistance curves recorded before, during and after the NaCl injection test. The polarization curves were recorded at a) 1.1 h b) 53.4 h c) 71.6 h d) 99.2 h e) 167.3 h.

An interesting feature can be seen in the polarization curves in Figure 40a, *IR*-compensated by the measured HFR values, see Figure 40b. Polarization curves here do show indications of other loss mechanisms than ohmic overpotential – The curves overlap at low current densities, thus the activation overpotential was not affected, and curves do not bend down at higher current densities, which would be an indication of mass transport overpotential. Still, *IR*-compensation by the measured HFR values does not suffice to restore the current density – voltage curves back to the initial level.

Probable explanation for this phenomenon is the inclusion of contributions from both H^+ and Na^+ conductivity in the membrane into measured HFR. Mobility of Na^+ in the membrane is lower than that of H^+; therefore the measured HFR increases as sodium ions replace protons. However, the increase in real resistance experienced by protons is steeper since the number of available acid sites is constant and the ratio of protons to sodium ions decreases. Fuel cell performance depends only on H^+ conductivity, since they are the only species that can carry current through the membrane. While sodium ions have the same electrical charge as protons, they are not reduced at the cathode, because the reduction potential of Na^+ is 2.71 V, which is outside the operating conditions of a PEM fuel cell.

If assumed that only the ohmic overpotential is increased by NaCl injection, the resistance experienced by protons can be calculated from the measured polarization curves. This is done by finding a resistance values that would make all *IR*-compensated polarization curves overlap with the first one. The least squares method was used obtain the resistance values (R_{calc}) presented in Figure 41a, which contains also the measured HFR values for reference. Polarization curves in Figure 41b are *IR* -compensated by R_{calc} values and match the original curve well. This indicates that ohmic loss is the primary loss mechanism affected by NaCl injection.

Measured HFR increased by ca. 29% during the experiment, while R_{calc} after the NaCl injection was 138% higher than the original HFR. However, fuel cell performance dropped only by 33%, despite the large decrease in proton conductivity.

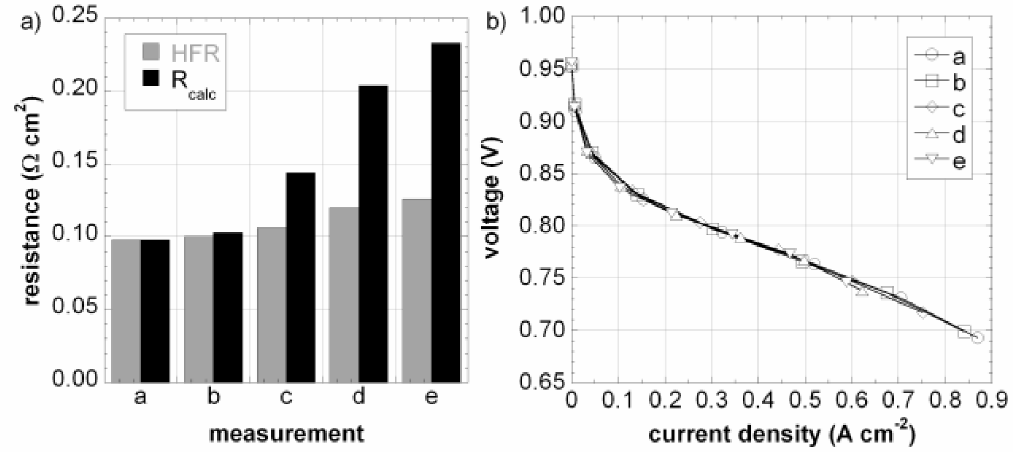

Figure 41: Calculated total resistance for polarization curves a) - e) in Figure 39, divided into measured HFR and contribution from other sources. b) Polarization curves from Figure 39, *IR*-compensated with the calculated resistance values (R_{calc}).

The assumption that ohmic loss is the only overpotential affected by the presence of NaCl, was supported by cyclic voltammetry after the NaCl injection test. Although the *ex situ* single electrode tests in H_2SO_4 solution containing NaCl indicated that Cl^- adsorbs onto the Pt catalyst and changes adsorption/desorption behavior of hydrogen, cyclic voltammograms from the fuel cell did not have any indication of chloride presence on the catalyst surface, see Figure 42.

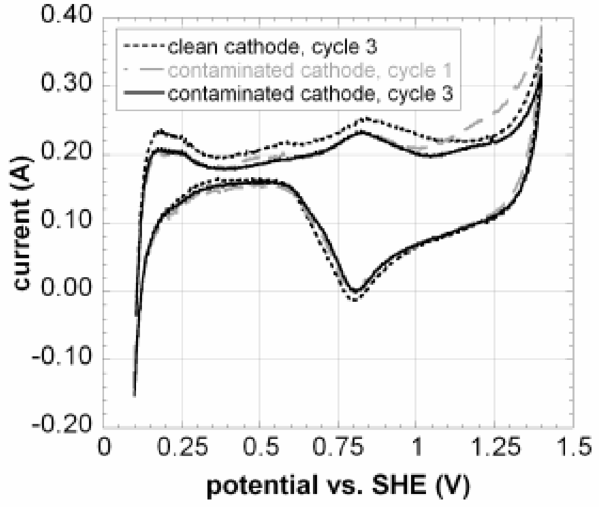

Figure 42: Cyclic voltammograms of cathode side electrode before and after NaCl injection test. Scan rate 10 mV s^{-1}, scan range 0.1 – 1.4 V vs. SHE.

Furthermore, recovery from NaCl was investigated by operating the cell continuously after stopping the NaCl injection for ca. 60 hours. Cell performance kept dropping for the first 10 hours after switching off the NaCl pump, indicating that the NaCl already in the cell did not flush out instantly. After that cell voltage stabilized and did not change significantly during the next 50 hours.

As a conclusion, the major effect of NaCl contamination in a PEM fuel cell is the replacement of protons by sodium ions in the ionomer. This increases the protonic resistance of the membrane, thus decreasing performance, and performance loss is irrecoverable under normal operating conditions. Presence of NaCl in the cathode side did not affect activation or mass transport overpotential. However, these results apply only to the hardware and operating conditions used in this work and results may be different under other conditions. Furthermore, the injection rate of NaCl was five to six orders of magnitude larger than those likely to occur naturally. Still, proton replacement by sodium ions can be expected to occur under all relevant operating conditions, and exposure of PEM fuel cell systems to NaCl should be minimized in order to avoid performance loss.

11. Summary and conclusions

The work in this thesis concentrates on investigating the limiting factors of PEMFC cathode performance. PEMFC cathode is a major contributor to cell losses, which are connected to oxygen reduction reaction, oxygen transport and water management. Furthermore, the cathode is exposed to impurities in the surrounding atmosphere. Oxygen transport and water management issues as well as the effect of air impurities are included in this study. The activation overpotential of oxygen reduction reaction is an electrochemical issue, involving catalyst and electrode development, and thus outside the scope of this thesis.

The main goal was to gain a better understanding of the effect of physical properties of cell components on mass transfer on the cathode and on cathode performance. The study on the effect of air impurities concentrated on one common impurity relevant for transportation applications of PEM fuel cells. Additionally, new measurement and analysis methods were developed.

Essential part for fuel cell operation and the focal point of this work was the porous transport layer. Properties of the cathode porous transport layer affect the transportation of oxygen and electric current as well as water management. Despite their evident importance, porous transport layers have received little research attention. In publication IV, an improved characterization method for porous transport layer performance under one and two phase conditions was presented, and correlation between the physical properties and cell performance was investigated. However, no clear correlation was found. During the work, the variations in contact pressure and contact resistance between cell components, which create current density and temperature variations, were observed and suggestive values for previously poorly known material properties, such as thermal conductivity and electrical contact resistance, were obtained. Furthermore, analysis of experimental results confirmed that the flooding of PEMFC cathode side begins in the porous transport layer, not in the electrode. Additionally, the performance of several porous transport layer materials was compared under different operating conditions.

Porous transport layer investigation continues in publication V. The focus was on the effect of inhomogeneous compression on porous transport layer caused by the channel-ridge structure of flow field plates, and the physical properties of porous transport layer materials under compression. New methods were developed for measuring the electrical bulk conductivity of the PTL and contact resistance at the PTL-flow field plate interface as a function of compression. Results include values for previously poorly known physical property parameters. Previous studies were found to overestimate the contribution from contact resistance at the interfaces because current collector resistance and the effects of compression on bulk conductivity of PTL are ignored.

Uneven contact pressure distribution between cell components stems from the pliability of porous transport layers. A rigid porous transport layer material would alleviate the problem and make possible the construction of free-breathing fuel cells with large open cathode area without additional support structures. In publication III, titanium sinter was studied as an option. Mechanical properties of titanium sinters are acceptable and material cost is affordable, but its water management properties are lacking and contact resistance between the sinter and other components is high. However, titanium sinters might have potential for some applications, especially if the problem with high contact resistance can be solved.

Publication VI presents a study on the effect of sodium chloride in the cathode air stream on PEM fuel cell performance. Sodium chloride was chosen due to its presence in the atmosphere offshore and in coastal regions, and its use as a road deicer. Thereby, the effect of sodium chloride was investigated under operating conditions that are relevant for automotive PEMFC applications. The presence of NaCl in the cathode was found to cause an irreversible performance loss due to proton replacement by sodium ions in the ionomer. Chloride ions were not observed to harm PEMFC performance.

New measurement methods were developed during this work. In publication I, the application of current interruption method for resistance measurement of a unit cell in a fuel cell stack is presented. Combined with unit cell voltage measurement, resistance measurements facilitate locating and identifying performance problems. In publication II, an apparatus for measuring current density distributions from a free-breathing PEMFC is introduced. Current density distribution measurements enable studying the effect of ambient conditions on fuel cell performance and efficient use of active cell area. Furthermore, the device can be used in developing passive control methods for free-breathing fuel cells.

As a result of this effort, new methods for PEM fuel cell and porous transport layer performance analysis and characterization were developed, and insight was gained on current density distribution in free-breathing fuel cells. This information is useful for developing more efficient passive control methods and free-breathing PEM fuel cells. The effect of porous transport layer properties on water management and mass and charge transport in the cathode is now understood better. Furthermore, values for previously poorly known material parameters were obtained, enabling modelers to develop more accurate models that take local phenomena into account. The effect of a common air impurity, sodium chloride, on PEM fuel cell performance was investigated and the action of the impurity on cell components was determined. This information can be used by automotive companies that have to consider the effect of air impurities on the performance of fuel cell power sources in vehicles.

Based on the work here, the following topics were found to warrant further research. The relation between the physical properties of porous transport layers and fuel cell performance is not established. Insight into gas and liquid transport process in the porous transport layer is needed. New testing and characterization methods are needed to better understand the critical processes and parameters of porous transport layers, especially in the presence of liquid water.

As a result, fuel cell models often include parameter values for porous transport layer and other properties that are based on estimations and best guesses. To improve accuracy, these parameters should be determined and applied into the models. Furthermore, models should take into account the local variations in material properties and contact pressure between components. These create local variations in reactant, water, heat and charge transport, which lead into emergence of current density distribution. Including local phenomena into computer models would provide new insight into fuel cell operation.

Before commercialization, the effect of various air impurities on PEM fuel cell performance and durability should be investigated. Many operating environments contain harmful compounds, and therefore development of impurity tolerant catalysts and other materials, as well as filtering methods should be pursued.

12. References

1 Key Word Energy Statistics 2005, IEA Publications 2005, available online at http://www.iea.org/dbtw-wpd/Textbase/nppdf/free/2005/key2005.pdf, quoted 2006-09-01

2 World Energy Outlook 2004, IEA Publications 2004, ISBN 92-64-1081-73-2004, available online at http://www.iea.org//textbase/nppdf/free/2004/weo2004.pdf, quoted 2006-07-26

3 World Energy Outlook 2005 Fact Sheet “Where Do Current Energy Trends Lead?”, IEA Publications 2005, available online at http://www.worldenergyoutlook.org/fact_sheets/Global_Energy_Trends.pdf, quoted 2006-07-26

4 DOE Hydrogen Program 2005 Annual Progress Report, U.S. Department of Energy, 2005, available online at http://www.hydrogen.energy.gov/annual_progress05.html, quoted 2006-07-26

5 Hydrogen, Fuel Cells and Infrastructure Technologies Program - Multi-Year Research, Development and Demonstration Plan. U.S. Department of Energy, Energy Efficiency and Renewable Energy, 2005, available online at http://www1.eere.energy.gov/hydrogenandfuelcells/mypp/index.html, quoted 2006-07-26

6 Fuel Cell Technology Challenges, U.S. DOE Energy Efficiency and Renewable Energy, available online at http://www.eere.energy.gov/hydrogenandfuelcells/fuelcells/fc_challenges.html , quoted 2006-09-01

7 W.R. Grove, Philosophical Magazine, Ser. 3, Vol. 14, 1839

8 W.R. Grove, Proc. R. Soc. London 5 1845, pp. 557-559

9 http://www.risoe.dk/Afd-abf/sofc/fuel/history_uk.htm, quoted 2006-08-02

10 U.S. Patent 28317 to M. Vergnes, May 17, 1860, quoted from S.G. Meiburh, Electrochim. Acta 11, pp. 1301-1318, 1966

11 J.A.A. Ketelaar, “History”, in L.J.M.J. Blomen and M.N. Mugerwa (eds.), “Fuel Cell Systems”, Plenum Press, New York 1993, ISBN 0-306-44158-6

12 http://chem.ch.huji.ac.il/~eugeniik/history/bacon.html, quoted 2006-08-02

13 A.J. Appleby and F.R. Foulkes, Fuel cell handbook, New York, USA, van Nostrand Reinhold, 1989, 762 p., ISBN 00-442-31926-6

14 http://en.wikipedia.org/wiki/Gemini_V, quoted 2006-08-02

15 C. Lamy, A. Lima, V. LeRhun, F. Delime, C. Coutanceau and J.-M. Léger, J. Power Sources 105(2) 2002, pp. 283-296

16 A. Verma and S. Basu, J. Power Sources 145(2) 2005, pp. 282-285

17 H.A. Gasteiger, W. Gu, R. Makharia, M.F. Mathias, B. Sompalli, “Beginning-of-life MEA performance–efficiency loss contributions”, in: W. Vielstich, A. Lamm, H.A. Gasteiger (Eds.), Handbook of Fuel Cells: Fundamentals, Technology, and Applications, vol. 3, Chapter 46, Wiley, 2003, p. 593

18 M. Rikukawa and K. Sanui, Prog. Polym. Sci. 25(10) 2000, pp. 1463-1502

19 J. Zhang, Z. Xie, J. Zhang *et al.*, J. Power Sources 160(2) 2006, pp. 872-891

20 J. Zhang and R. Datta, J. Electrochem. Soc. 149(11) 2002, pp. A1423-A1431

21 W.A. Adams, J. Blair, K.R. Bullock and C.L. Gardner, J. Power Sources 145(1) 2005, pp. 55-61

22 D.C. Papageorgopoulos, M.P. de Heer, M. Keijzer, J.A.Z. Pieterse and F.A. de Bruijn, J. Electrochem. Soc. 151(5) 2004, pp. A763-A768

23 S. Gottesfeld and J. Pafford, J. Electrochem. Soc. 135(10) 2988, pp. 2651-2652

24 F.A. Uribe, J.A. Valerio, F.H. Garzon and T.A. Zawodzinski, Electrochem. Solid State Lett. 7(10) 2004, pp. A376-A379
25 P.A. Adcock, S.V. Pacheco, K.M. Norman and F.A. Uribe, J. Electrochem. Soc. 152(2) 2005, pp. A459-466
26 Q. Li, R. He, J.O. Jensen and N.J.Bjerrum, Fuel Cells 4(3) 2004, pp. 147-159
27 Q. Li, R. He, J.-A. Gao, J.O. Jensen and N. J. Bjerrum, J. Electrochem. Soc. 150(12) 2003, pp. A1599-1605
28 M.S. Bursell, Electrochemical cell and a gas diffusion electrode for it. PCT Int. App. WO8100032, 1981-01-08
29 M.S. Wilson and S. Gottesfeld, J. Appl. Electrochem. 22(1) 1992, pp. 1-7
30 R. Lindstrom, R.J. Allen and W. Juda, Thin carbon-cloth-based electrocatalytic gas diffusion electrodes and electrochemical cells comprising them. Eur. Pat. App. EP26995, 1981-04-15
31 Z. Qi and A. Kaufman, J. Power Sources 109(1) 2002, pp. 38-46
32 V.A. Paganin, E.A. Ticianelli and E.R. Gonzalez, J. Appl. Electrochem. 26(3) 1996, pp. 297-304
33 M. Mathias, J. Roth, J. Fleming, W. Lehnert, Diffusion media materials and characterisation, in Handbook of Fuel Cells – Fundamentals, Technology and Applications, Vol. 3: Fuel Cell Technology and Applications, Chapter 46, pp. 517-537, W. Vielstich, H. Hasteiger and A. Lamm, Editors, John Wiley & Sons, Ltd., New York, USA 2003
34 V. Mehta and J.S. Cooper, J. Power Sources 114(1) (2003), pp. 32-53
35 D. Oei, J.A. Adams, A.A. Kinnelly, G.H. Purnell, R.I. Sims, M.S. Sulek, D.A. Wernette, B. James, F. Lomax, G. Baum, S. Thomas, I. Kuhn, Direct hydrogen fueled proton exchange membrane fuel cell system for transportation applications: Final Technical Report, DOE/CE/50389-505, 2000
36 Y.W. Rho, O.A. Velev, S. Srinivasan and Y.T. Kho, J. Electrochem. Soc. 141(8) 1994, pp. 2084-2089
37 M. Ciureanu and R. Roberge, J. Phys. Chem. B 105(17) 2001, pp. 3531-3539
38 D.M. Bernardi and M.W. Verbrugge, AIChE J. 37(8) 1991, pp. 1151-1163
39 J.C. Amphlett, R.M. Baumert, R.F. Mann, B.A. Peppley, P. R. Roberge and T.J. Harris, J. Electrochem. Soc. 142(1) 1995, pp. 1-8
40 E. Middelman, W. Kout, B. Vogelaar, J. Lenssen and E. De Waal, J. Power Sources 118(1-2) 2003, pp. 44-46
41 P.L. Hentall, J.B. Lakeman, G.O. Mepsted, P.L. Adcock and J.M. Moore, J. Power Sources 80(1-2) 1999, pp. 235-142
42 H. Wang, M.A. Sweikart and J.A. Turner, J. Power Sources 115(2) 2003, p. 243-251
43 N. Aukland, A. Boudina, D.S. Eddy, J.V. Mantese, M.P. Thompson and S.S. Wang, J. Mat. Res. 19(6) 2004, pp. 1723-1729
44 M.P. Brady, K. Weisbrod, C. Zawodzinski, I. Paulauskas, R.A. Buchanan and L.R. Walker, Electrochem. Solid-State Lett. 5(11) 2002, pp. A245-A247
45 N. Cunningham, D. Guay, J.P. Dodelet, Y. Meng, A.R. Hlil and A.S. Hayb, J. Electrochem. Soc. 149(7) 2002, pp. A905-A911
46 D.N. Busick and M.S. Wilson, in Proton Conducting Membrane Fuel Cells, S. Gottesfeld, T. F. Fuller, and G. Halpert, Editors, PV 98-27, pp. 435-445, The Electrochemical Society Proceedings Series, Pennington, NJ (1998)
47 T.M. Besmann, J.W. Klett, J.J. Henry Jr. and E. Lara-Curzio, J. Electrochem. Soc. 147(11) 2000, pp. 4083-4086
48 E.A. Cho, U.-S. Jeon, H.Y. Ha, S.-A. Hong and I.-H. Oh, J. Power Sources 125(2) 2004, pp. 178-182

49 J. Huang, D.G. Baird and J.E. McGrath, J. Power Sources 150(1) 2005, pp. 110-119
50 C. Zawodzinski, M.S. Wilson and S. Gottesfeld, in Proton Conducting Membrane Fuel Cells, S. Gottesfeld, T. F. Fuller, and G. Halpert, Editors, PV 98-27, pp. 446-456, The Electrochemical Society Proceedings Series, Pennington, NJ (1998)
51 S. Gamburzev and A.J. Appleby, J. Power Sources 107(1) 2002, pp. 5-12
52 E. Birgersson and M. Vynnycky, J. Power Sources 153(1) 2006, pp. 76-88
53 W.-M. Yan, C.-H. Yang, C.-Y. Soong, F. Chen and S.-C. Mei, J. Power Sources 160(1) 2006, pp. 284-292
54 D. Natarajan and T. Van Nguyen, AIChE J. 51(9), pp. 2587-2598
55 D. Natarajan and T. Van Nguyen, AIChE J. 51(9), pp. 2599-2608
56 W. Liu, K. Ruth and G. Rusch, J. New Mat. Electrochem. Sys. 4(4) 2001, pp. 227-231
57 J. Kaskimies, “Kaasuvirtaus polymeeripolttokennon katodilla (Gas flow on the cathode of a solid polymer fuel cell)”, Helsinki University of Technology, 2000, Master’s thesis (in Finnish)
58 M. Noponen, “Experimental studies and simulations on proton exchange membrane fuel cell based energy storage systems”, Helsinki University of Technology, 2000, Master’s thesis
59 T. Mennola, “Design and experimental characterization of polymer electrolyte membrane fuel cells”, Helsinki University of Technology, 2000, Licentiate’s thesis
60 M. Mikkola, “Experimental studies on polymer electrolyte membrane fuel cell stacks”, Helsinki University of Technology, 2001, Master’s thesis
61 W.J. Wruck, R.M. Machado, T.W. Chapman, J. Electrochem. Soc. 134(3) 1987, pp. 539-546
62 C. Lagergren, G. Lindbergh, D. Simonsson, J. Electrochem. Soc. 142(3) 1995, pp. 787-797
63 F. N. Büchi, A. Marek, G. Scherer, J. Electrochem. Soc. 142(6) 1995, pp. 1895-1901
64 F.N. Büchi, G.G. Scherer, J. Electroanal. Chem. 404(1) 1996, pp. 37-43
65 F. Richter, C.-A. Schiller and N. Wagner, in Electrochemical Applications 1/2002, ZAHNER-elektrik GmbH & Co KG, 2002
66 D. Webb, S. Møller-Holst, J. Power Sources 103(1) 2001, pp. 54-60
67 T. Mennola, M. Noponen, M. Aronniemi, T. Hottinen, M. Mikkola, O. Himanen and P. Lund, J.Appl.Electrochem. 33(11) 2003, pp. 979-987
68 P.C. Rieke and N.E. Vanderborgh, J. Electrochem. Soc. 134(5) 1987, pp. 1099-1104
69 A. B. Geiger, R. Eckl, A. Wokaun and G. G. Scherer, J. Electrochem. Soc. 151(3) 2004, pp. A394-A398
70 J. Stumper, S.A. Campbell, D.P. Wilkinson, M.C. Johnson, M. Davis, Electrochim. Acta 43(24) 1998, pp. 3773-3783
71 C. Wieser, A. Helmbold, W. Schnurnberger, in Proc. Electrochem. Soc. 98-27 (Proton Conducting Membrane Fuel Cells II), 1999, p. 457-461
72 C. Wieser, A. Helmbold, E. Gülzow, J. Appl. Electrochem. 30(7) 2000, pp. 803 – 807
73 M.M. Mench, C.Y. Wang, J. Electrochem. Soc. 150(1) 2003, pp. A79-A85
74 M.M. Mench, C.Y. Wang, M. Ishikawa, J. Electrochem. Soc. 150(8) 2003, pp. A1052-A1059

75 Y.-G. Yoon, W.-Y. Lee, T.-H. Yang, G.-G. Park, C.-S. Kim, J. Power Sources 118(1-2) 2003, pp. 193-199

76 N. Rajalakshmi, M. Raja, K. S. Dhathathreyan, J. Power Sources 112(1) 2002, pp. 331-336

77 S. J.C. Cleghorn, C.R. Derouin, M.S. Wilson, S. Gottesfeld, J. Appl. Electrochem. 28(7) 1998, pp. 663-672

78 T. Hottinen, M. Noponen, T. Mennola, O. Himanen, M. Mikkola and P. Lund, J. Appl. Electrochem. 33(3-4) 2003, pp. 265-271

79 M. Noponen, T. Hottinen, T. Mennola, M. Mikkola and P. Lund, J. Appl. Electrochem. 32(10) 2002, pp. 1081-1089

80 D. Natarajan and T. Van Nguyen, J. Power Sources 135(1-2) 2004, pp. 95-109

81 S. Voss, H. Kollmann and W. Kollmann, J. Power Sources 127(1-2) 2004, pp. 93-97

82 C. Zawodzinski, M.S. Wilson and S. Gottesfeld in Proceedings - Electrochemical Society 98-27, Proton Conducting Membrane Fuel Cells II, 1999, pp. 446-456

83 M.S. Wilson and C. Zawodzinski, PCT Int. Appl., 1998, 97-US17248

84 J.C. Amphlett, R.M. Baumert, R.F. Mann, B.A. Peppley, P.R. Roberge, T.J. Harris, J. Electrochem. Soc. 142(1) 1995, pp. 1–8

85 R. Varila, CEO, LabGas Instrument Co., 29 November 2002 (private communication between T. Hottinen and R. Varila)

86 D. L. Wood III, M. Maendle, P. M. Wilde and M. Murata, Abstracts of 2002 Fuel Cell Seminar, Palm Springs, California, November 18-21, 2002, pp. 41-44

87 H. Dohle, R. Jung, N. Kimiaie, J. Mergel and M. Müller, J. Power Sources 124(2) 2003, pp. 371-384

88 T. Hottinen, M. Mikkola, T. Mennola, P. Lund, J. Power Sources 118(1-2) 2003, pp. 183-188

89 B. Mueller, T. Zawodzinski, J. Bauman, F. Uribe, S. Gottesfeld, E.S. De Castro and M. De Marinis, Electrochemical Society Proceedings 98-27, The Electrochemical Society, Pennington, New Jersey, USA, 1999, pp. 1-9

90 T. Springer, M. Wilson and S. Gottesfeld, J. Electrochem. Soc. 140(12) 1993, pp. 3513-2536

91 T.E. Springer, T.A. Zawodzinski, M.S. Wilson, S. Gottesfeld, J. Electrochem. Soc., 143(2) 1996 , pp. 587-599

92 K. Tüber, D. Pócza, C. Hebling, J. Power Sources, 124(2) 2003, pp. 403-414

93 P.M. Wilde, M. Mändle, M. Murata, N. Berg, Fuel Cells 4(3) 2004, pp. 180-184

94 M.V. Williams, E. Begg, L. Bonville, H.R. Kunz, J.M. Fenton, J. Electrochem. Soc. 151(8) 2004, pp. A1173-A1180

95 C. Lim, C.Y. Wang, Electrochim. Acta 49(24) 2004, pp. 4149-4155

96 B. Thoben, A. Siebke, J. New Mat. Electrochem. Sys. 7(1) 2004, pp. 13-20

97 G.-G. Park, Y.-J. Sohn, T.-H. Yang, Y.-G. Yoon, W.-Y.Lee, C.-S. Kim, J. Power Sources 131(1-2) 2004, pp. 182-187

98 U. Pasaogullari, C.-Y. Wang, J. Electrochem. Soc. 151(3) 2004, pp. A399-A406

99 V. Mishra, F. Yang, R. Pitchumani, J. Fuel Cell Sci. Tech. 1(1) 2004, pp. 2-9

100 E. Antolini, E. E. Passos, E. A. Ticianelli, J. Power Sources 109(2) 2002, pp. 477-482

101 E. Antolini, E. E. Passos, E. A. Ticianelli, J. Appl. Electrochem. 32(4) 2002, pp. 383-383

102 E. Antolini, E. E. Passos, E. R. Gonzalez, E. A. Ticianelli, 2002 Fuel Cell Seminar Abstracts: Palm Springs, California, November 18-21, 2002, pp. 70-73
103 L.R. Jordan, A.K. Shukla, T. Behrsing, N.R. Avery, B.C. Muddle, M. Forsyth, J. Appl. Electrochem., 30(6) 2000, pp. 641-646
104 E. Gülzow, M. Schulze, N. Wagner, T. Kaz, R. Reissner, G. Steinhilber, A.J. Schneider, J. Power Sources 86(1-2) 2000, pp. 352-362
105 C. S. Kong, D-Y. Kim, H-K. Lee, Y-G. Shul, T-H. Lee, J. Power Sources 108(1-2) 2002, pp. 185-191
106 J. Moreira, A. L. Ocampo, P. J. Sebastian, M. A. Smit, M. D. Salazar, P. del Angel, J. A. Montoya, R. Pérez, L. Martínez, Int. J. Hydrogen Energy 28(6) 2003, pp. 625-627
107 J. Soler, E. Hontañón, L. Daza, J. Power Sources 118(1-2) 2003, pp. 172-178
108 Y.-G. Yoon, G.-G. Park, T.-H. Yang, J.-N. Han, W.-Y. Lee, C. S. Kim, Int. J. Hydrogen Energy 28(6) 2003, pp. 657-662
109 J. Ihonen, F. Jaouen, G. Lindbergh, G. Sundholm, Electrochim. Acta 46(19) 2001, pp. 2899-2911
110 Jari Ihonen, “Development of Characterisation Methods for the Components of the Polymer Electrolyte Fuel Cell”, Kungliga Tekniska Högskolan, 2003, Doctoral thesis
111 P. Vie and S. Kjelstrup, Electrochim. Acta 49(7) 2004, pp. 1069-1077
112 J. Ihonen, M. Mikkola, G. Lindbergh, J. Electrochem. Soc. 151(8) 2004, pp. A1152-A1161
113 G. Lin and T.V.Nguyen, J. Electrochem. Soc. 152(10) 2005, pp. A1942-A1948
114 T. Berning and N. Djilali, J. Power Sources 124(2) 2003, pp. 440-452
115 D. Natarajan and T.V. Nguyen, J. Electrochem. Soc. 148(12) 2001, pp. A1324-A1335
116 J.G. Pharoah, J. Power Sources 144(1) 2005, pp. 77-82
117 H. Meng and C.Y. Wang, J. Electrochem. Soc. 151(3) 2004, pp. A358-A367
118 J.G. Pharoah, K. Karan, W. Sun, J. Power Sources 161(1) 2006, pp. 214-224
119 M. Khandelwal and M.M. Mensch, J. Power Sources 161(2) 2006, pp. 1106-1115
120 H. Wang and J.A. Turner, J. Power Sources 128(2) 2004, pp. 193-200
121 S. Miachon and P. Aldebert, J. Power Sources 56(1) 1995, pp.31-36
122 W. Sun, B.A. Peppley and K. Karan, J. Power Sources 144(1) 2005, pp. 42-53
123 P. Zhou, C.W. Wu, G.J. Ma, J. Power Sources 155(2) 2006, pp. 1115-1122
124 Manufacturer’s data sheet for ®SIGRACET GDL 10 BA, SGL Carbon AG
125 M. Yamaguchi, H. Matsuo and S. Uozumi, Japanese patent JP06084529, 1994
126 K. Kodama, Japanese patent JP2004178893, 2004
127 A. Caillard, P. Brault, J. Mathias, C. Charles, R.W. Boswell and T. Sauvage, Surf. Coat. Tech. 200(1-4) 2005, pp. 391-394
128 T. Tomimura, S. Nakamura, H. Nonami and H. Saito, Proc. 7th IEEE International Conference on Solid Dielectrics, IEEE New York, USA, 2001, pp. 101-104
129 T. Hottinen, O. Himanen, S. Karvonen and I. Nitta, “Inhomogeneous Compression of PEMFC Gas Diffusion Layer, Part II: Modeling the effect” accepted for publication in J. Power Sources, Sep 2006
130 P. Stonehart, G. Kohlmayr, Electrochim. Acta 17(3) 1972, pp. 369-382
131 W. Vogel, L. Lundquist, P. Ross, P. Stonehart, Electrochim. Acta 20(1) 1975, pp. 79-93

132 M. Murthy, M. Esayian, A. Hobson, S. MacKenzie, W.-K. Lee, J.W. Van Zee, J. Electrochem. Soc. 148(10) 2001, pp. A1141-A1147
133 J.J. Baschuk and X. Li, Int. J. Energy Res. 25(8) 2001, pp. 695-713
134 Z. Qi, C. He, A. Kaufman, J. Power Sources 111(2) 2002, pp. 239-247
135 D.C. Papageorgopoulos, F.A. de Bruijn, J. Electrochem. Soc. 149(2) 2002, pp. A140-A145
136 K.K. Bhatia, C.-Y. Wang, Electrochim. Acta 49(14) 2004, pp. 2333-2341
137 J. Zhang, H. Wang, D.P. Wilkinson, D. Song, J. Shen, Z.-S. Liu, J. Power Sources 147(1-2) 2005, pp. 58-71
138 M. Murthy, M. Esayian, W.-K. Lee, J.W. Van Zee, J. Electrochem. Soc. 150(1) 2003, pp. A29-A34
139 S. Giddey, F.T. Ciacchi, S. Badwal, Ionics 11(1&2) 2005, pp. 1-10
140 T. Smolinka, M. Heinen, Y.X. Chen, Z. Jusys, W. Lehnert, R. Behm, Electrochim. Acta 50(25-26) 2005, pp. 5189-5199
141 N N. Rajalakshmi, T.T. Jayanth, K.S. Dhathathreyan, Fuel Cells 3(4) 2004, pp. 177-180
142 F.A. de Bruijn, D.C. Papageorgopoulos, E.F. Sitters. G.J.M. Janssen, J. Power Sources 110(1) 2002, pp. 117-124
143 P.J. de Wild, R.G. Nyqvist, F.A. de Brujin in Abstracts of the 2002 Fuel Cell Seminar, Palm Springs, CA, USA, 2002, pp. 227-230
144 Y. Takagi, F. Nakatani, M. Okamoto, T. Shimizu, S. Hikita in Fuel Cell Power for Transportation 2004, Society of Automotive Engineers 2004, ISBN: 0-7680-1363-1 pp. 173-179
145 R. Mohtadi, W.-K. Lee, S. Cowan, J. W. Van Zee, M. Murthy, Electrochem. Solid-State Lett. 6(12) 2003, pp. A272-A274
146 F.A. Uribe, S. Gottesfeld, T.A. Zawodzinski, Jr., J. Electrochem. Soc. 149(3) 2002, pp. A293-A296
147 R. Halseid, P.J.S. Vie, R. Tunold, J. Electrochem. Soc. 151(3) 2004, pp. A381-A388
148 H.J. Soto, W.-K. Lee, J.W. Van Zee and M. Murthy, Electrochem. Solid-State Lett. 6(7) 2003, pp. A133-A135
149 V.O. Mittal, H.R. Kunz, J.M. Fenton. Electrochem. Solid-State Lett. 9(6) 2006, pp. A299-A302
150 P.R. Hayter, P. Mitchell, R.A.J. Dams, C. Dudfield, N. Gladding in The effect of contaminants in the fuel and air streams on the performance of a solid polymer fuel cell, ETSU F/02/00126/REP Report to UK Department of Trade and Industry, 1997
151 L. Pino, V. Recupero, M. Laganà, M. Minutoli in Proceedings of the 1998 Fuel Cell Seminar, Palm Springs, CA, USA, 1998
152 F.A. Uribe, J. Valerio and T. Rockward in Abstracts of the 205th ECS Meeting, ECS, Pennington, New Jersey, USA, 2004, Abs. #332
153 R. Mohtadi, W.-K. Lee, J.W. Van Zee, J. Power Sources 138(1-2) 2004, pp. 216-225
154 J.M. Moore, P.L. Adcock, J.B. Lakeman, G.O. Mepsted, J. Power Sources 85(2) 2000, pp. 254-260
155 G. Mepsted in Investigation of the effects of air contaminants on SPFC performance, ETSU F/02/00172REP Report to UK Department of Trade and Industry, DTI/Pub URN 01/905, 2001
156 T. Okada, J. Electroanal. Chem. 465(1) 1999, pp. 1-17
157 T. Okada, J. Electroanal. Chem. 465(1) 1999, pp. 18-29

158 M.C. Bétournay, G. Bonnell, E. Edwardson, D. Paktunc, A. Kaufman, A.T. Lomma. J. Power Sources 134(1) 2004. pp. 80-87
159 Anon. A method for cleaning air from aggressive salts. Research Disclosure 474 (2003), pp. P1117
160 Y. Si, R. Jiang, J.-C. Lin, H.R. Kunz, J.M. Fenton, J. Electrochem. Soc. 151(11) 2004, A1820-A1824
161 H. Xu, Y. Song, H.R. Kunz, J.M. Fenton, J. Power Sources 159(2) 2006, pp. 979-986
162 O. Savadogo, J. Power Sources 127(1-2) 2004, pp. 135-161
163 J.A. Asensio, P. Gomez-Romero, Fuel Cells 5(3) 2005, pp. 336-343
164 H.-F. Oetjen, V. M. Schmidt, U. Stimming, F. Trila, J. Electrochem. Soc. 143(12) 1996, pp. 3838-3842
165 H.A. Gasteiger, N. Markovic, P. N. Ross, J. Phys. Chem. 99(20) 1995, pp. 8290-8301
166 A.S. Aricò, E. Modica, I. Ferrara, V. Antonucci, J. Appl. Electrochem. 28(9) 1998, pp. 881-887
167 C. He, H.R. Kunz, J.M. Fenton, J. Electrochem, Soc. 150(8) 2003, pp. A1017–A1024
168 R. J. Bellows, E. M. Soos, R. P. Reynolds, Electrochem. Solid-State Lett. 1(2) 1998, pp. 69-70
169 J.-H. Wee, K.-Y. Lee. J. Power Sources 157(1) 2006, pp. 128-135
170 L L. Gubler, G.G. Scherer, A .Wokaun. Phys. Chem. Chem. Phys. 3, 2001 pp. 325-329
171 T. Zawodzinski, T. Springer, J. Bauman, T. Rockward, F. Uribe, and S. Gottesfeld, in Proton Conducting Membrane Fuel Cells, S. Gottesfeld, T. F. Fuller, and G. Halpert, Editors, PV 98-27, pp. 127-135, The Electrochemical Society Proceedings Series, Pennington, NJ, USA, 1998
172 J.W. Bauman, T.A. Zawodzinski, Jr., S. Gottesfeld, in Proton Conducting Membrane Fuel Cells, S. Gottesfeld, T. F. Fuller, and G. Halpert, Editors, PV 98-27, pp. 136-149, The Electrochemical Society Proceedings Series, Pennington, NJ, USA, 1998
173 V.M. Schmidt, H.-F. Oetjen, J. Divisek, J. Electrochem. Soc. 144(9) 1997, pp. L237-L238
174 J. Divisek, H.-F. Oetjen, V. M. Schmidt, U. Stimming, Electrochim. Acta, 43(24) 1998, pp. 3811-3815
175 A.T. Haug, R.E. White, J.W. Weidner and W. Huang, J. Electrochem. Soc. 149(7) 2002, pp. A862-A867
176 H. Yu, Z. Hou, B. Yi, Z. Lin. J. Power Sources 105(1) 2002 pp. 52-57
177 T. Okada, N. Nakamura, J. Electrochem. Soc. 144(8) 1997, pp. 2744-2750
178 T. Okada, S. Møller-Holst, O. Gorseth, S. Kjelstrup. J. Electroanal. Chem. 442(1-2) 1998, pp. 137-145
179 T. Okada, Y. Ayato, M. Yuasa, I. Sekine. J. Phys. Chem. B, 103(17) 1999, pp. 3315 -3322
180 A. Pozio, R. F. Silva, M. De Francesco, L. Giorgi, Electrochim. Acta 48(11) 2003, pp. 1543-1549
181 M.J. Kelly, B. Eggera, G. Fafilek, J.O. Besenhard, H. Kronberger, G.E. Nauer. Solid State Ionics 176(25-28) 2005, pp. 2111-2114
182 M.J. Kelly, G. Fafilek, J.O. Besenhard, H. Kronberger, G.E. Nauer. J. Power Sources 145(2) 2005, pp. 249-252
183 S. Kundu, L.C. Simon, M. Fowler, S. Grot. Polymer 46(25) 2005, pp. 11707-11715

184 T.J. Schmidt, U.A. Paulus, H.A. Gasteiger, R.J. Behm. J. Electroanal. Chem. 508(1-2) 2001, pp. 41-47
185 V. Stamenkovic, N.M. Markovic, P.N. Ross, Jr., J. Electroanal. Chem. 500(1-2) 2001, pp. 44-51
186 M.S. Wilson, J.A. Valerio, S. Gottesfeld, Electrochim. Acta 40(3) 1995, pp. 355-363

Appendix A – List of other publications

Publications with contribution by the author but not included in this thesis are listed below by publication year in descending order.

- Olli Himanen, Tero Hottinen, Mikko Mikkola and Ville Saarinen, "*Characterization of membrane electrode assembly with hydrogen-hydrogen cell and ac-impedance spectroscopy, Part I: Experimental*", Electrochim. Acta 52(1) 2006, pp. 206-214
- Tero Hottinen, Olli Himanen, Mikko Mikkola, "*Convective Heat and Mass Transfer Coefficients of Cathode in a Planar Free-Breathing PEM Fuel Cell*", Paper No. TH1, In: Proceedings of the Fourth International Conference on Heat Transfer, Fluid Mechanics & Thermodynamics, Eds. J.P. Meyer & A.G. Malan, 19-22 September 2005, Cairo, Egypt
- T. Mennola, M. Noponen, T. Kallio, Mikko Mikkola and Tero Hottinen, "*Water balance in a free-breathing polymer electrolyte membrane fuel cell*". J. Appl. Electrochem. 34(01) 2004, pp. 31 - 36
- T. Hottinen, M. Mikkola and P. Lund, "*Evaluation of planar free-breathing polymer electrolyte membrane fuel cell design*". J. Power Sources 129(01) 2004, pp. 68-72
- T. Hottinen, M. Noponen, T. Mennola, O. Himanen, M. Mikkola and P. Lund, "*Effect of ambient conditions on performance and current distribution of a polymer electrolyte membrane fuel cell*". J. Appl. Electrochem. 33(03-04) 2003, pp. 265 - 271
- T. Mennola, M. Noponen, M. Aronniemi, T. Hottinen, M. Mikkola and P. Lund, "*Mass transport in the cathode of a free-breathing polymer electrolyte membrane fuel cell*". J. Appl. Electrochem. 33(11) 2003, pp. 979 - 987
- M. Noponen, T. Hottinen, T. Mennola, M. Mikkola and P. Lund, "*Determination of mass diffusion overpotential distribution with flow pulse method from current distribution measurements in a PEMFC*", J. Appl. Electrochem. 32(10) 2002, pp. 1081-1089